

Rochester Institute of Technology

RIT Digital Institutional Repository

Theses

7-28-2010

Stereoscopic particle image velocimetry analysis of healthy and emphysemic acinus models

Emily Jean Berg

Follow this and additional works at: <https://repository.rit.edu/theses>

Recommended Citation

Berg, Emily Jean, "Stereoscopic particle image velocimetry analysis of healthy and emphysemic acinus models" (2010). Thesis. Rochester Institute of Technology. Accessed from

This Thesis is brought to you for free and open access by the RIT Libraries. For more information, please contact repository@rit.edu.

*Stereoscopic Particle Image Velocimetry Analysis of
Healthy and Emphysemic Acinus Models*

Stereoscopic Particle Image Velocimetry Analysis of Healthy and Emphysemic Acinus Models

by

Emily Jean Berg

A Thesis Presented in Partial Fulfillment of the Requirements for
the Degree of *Master of Science in Mechanical Engineering*

Approved by:

Dr. Risa J. Robinson

Department of Mechanical Engineering

(Thesis Advisor)

Dr. Elizabeth A. DeBartolo

Department of Mechanical Engineering

Dr. Steven W. Day

Department of Mechanical Engineering

Dr. Wayne W. Walter

Department of Mechanical Engineering

(Department Representative)

**Rochester Institute of Technology
Kate Gleason College of Engineering
Department of Mechanical Engineering**

Rochester, NY

July 28th, 2010

Permission for Duplication

Permission Granted

Stereoscopic Particle Image Velocimetry Analysis of Healthy and Emphysemic Acinus Models

I, *Emily J. Berg*, hereby grant the Wallace Library at the Rochester Institute of Technology the right to reproduce this thesis in whole or in part.

Copyright 2010 © Emily J. Berg. All rights reserved.

Unlimited permission to copy or use this document, in whole or in part, for educational or otherwise non-profit purposes, is hereby granted subject to the inclusion of a citation as specified in a recognized style manual.

Date: _____

Signature of Author: _____

Emily J. Berg

565 Hall Road

Jamestown, NY 14701

Email: ejb3439@gmail.com

Phone: (716) 450 – 6947

Abstract

Inhaled particles reaching the alveolar walls have the potential to cross the blood gas barrier and enter the blood stream. Pulmonary dosimetry, however, is not well understood. Numerical and experimental studies shed some light on the mechanisms of particle transport, but realistic geometries have not been investigated. In order to accurately predict particle deposition, the characteristics that affect deposition need to be understood. This includes, but is not limited to, fluid flow, lung morphology, breathing conditions, and particle concentration. Various geometries have been used for research, but very few are close representations to *in vivo* geometry. Most studies have used simplified or idealized geometries based on published dimensions, but none replicate actual *in vivo* geometry; even fewer examine the differences that exist between healthy and diseased lung geometries.

The following work analyzes and compares the flow fields that exist in replica healthy and emphysemic lungs by using realistic geometries and breathing conditions. Actual human lung casts for *in vivo* healthy and emphysemic geometries were obtained, scanned, and used to reconstruct three dimensional replica models. From these geometries, hollow compliant models were created and used to simulate breathing under healthy and diseased conditions. It was shown that major geometric differences exist between the healthy and emphysemic models. Specifically, the emphysemic model alveoli appeared to merge into a single large alveolus with no potential regions of recirculation, as compared to the healthy model, which contained smaller, more distinct alveoli, and an overall model volume 11x smaller than the emphysemic model.

Each experimental geometry was examined using stereoscopic particle image velocimetry (stereoPIV) techniques. Realistic flow conditions were derived by the application of scaling theory to convert from the *in vivo* size to the large scale experimental set up. Experimental techniques were validated by comparing to computational fluid dynamic (CFD) results when using a simplified three-dimensional (3D) bulb geometry. Following validation, experimental flow fields were examined, on the large experimental scale, using velocity and streamline plots, for healthy and emphysemic geometries. It was shown that reversible flow was present in both models; even in locations representing a high probability for recirculating or irreversible flow.

Each of the experimental flow fields was then scaled to represent *in vivo* velocity predictions. The emphysemic model (run under normal emphysemic breathing conditions) had a flow rate 8x that of the healthy model with normal breathing. The inlet velocity for the healthy normal breathing model, however, was 1.6x larger than the emphysemic. These flow results are a function of both the model geometry and the applied realistic breathing conditions. The distribution of *in vivo* velocity magnitude over the flow field was also different between the healthy and emphysemic models. Specifically, the healthy model enters at higher velocities than the emphysemic, and then uniformly slows as the fluid moves towards the walls. The emphysemic model yields a large region of fast flow near the inlet and slows at random locations as it approaches the walls. It was reasoned that even though inhaled particles would likely travel further into the emphysemic model compared to the healthy, the distance to reach the wall would be much greater in emphysema as compared to healthy. This would result in higher deposition efficiencies for healthy models as compared to emphysema, which is consistent with results found in the literature.

Acknowledgements

I wouldn't have been able to finish this thesis without the encouragement and support of a few notable people. I would first like to thank my research advisor, Dr. Risa Robinson, for all of her guidance and support throughout my graduate career. The relationship that we developed truly defined my experience at RIT and for that I am grateful. Thank you to my committee, Dr. DeBartolo, Dr. Day, and Dr. Walter, for supporting me in all of my endeavors. Professor John D. Wellin's contributions and expertise allowed me to complete this work to its fullest potential. I would also like to thank Dave Hathaway, Rob Kraynik, Steven Kosciol, William Finch, Diane Selleck, and the rest of the Mechanical Engineering staff for their general knowledge and willingness to help. Your support has played a vital role in the success of this thesis. My graduate experience would not have been as enjoyable without the support of my friends and fellow graduate students, specifically Ted Harding, Ken Court, Nohl Schluntz, Rob Alpern, Chris Natoli, Tim Dovi, John Koepfel, and Eric Feigenheimer. The memories we made were as important to me as the completion of this degree. Lastly, I would like to thank my parents, Wayne and Jean Berg, and my brothers, Ben and Vinnie, for all of their love and support. Their encouragement and involvement throughout my life has meant more to me than I can ever describe and I owe my success to them.

This work was supported by the American Cancer Society (RSG-05-021-01-CNE).

Table of Contents

Abstract.....	i
Acknowledgements	iii
Chapter 1: Introduction and Background Information	1
1.1 – Anatomy of the Lung	1
1.2 – Alveolar Numerical and Experimental Models Found in Literature.....	2
1.3 – Summary of Alveolar Model Results from the Literature	5
1.4 – Gaps in the Research.....	5
1.5 – Scope of the Thesis Work	6
Aim 1 – Create Compliant Hollow Models	6
Aim 2 – Develop PIV Setup Capable of 3D Flow Field Analyses	6
Aim 3 – Complete StereoPIV Analysis on Healthy and Emphysematous Models.....	7
Chapter 2: Model Creation	8
2.1 – Cast Human Lungs.....	8
2.1.1 – Healthy Human	8
2.1.2 – Emphysema Human	10
2.2 – Obtain Micro-CT Scans of Cast.....	11
2.3 – Create 3D Digital Model from 2D Slices.....	12
2.3.1 – Reconstruct Whole Model	12
2.3.2 – Edit 2D Slices of Final Model Region	14
2.3.3 – Process Surface of Final Model	15
2.4 – Create Inlet Duct	16
2.5 – Scale Model	19
2.5.1 – <i>In Vivo</i> Size	19

2.5.2 – Experimental Size	20
2.6 – Create Compliant Models	20
Chapter 3: Flow in the Experimental Model.....	23
3.1. – Theory	23
3.2 – Convergence of Small Wo and Re	24
3.3 – Healthy Human Parameters	25
3.3 – Emphysemic Human Parameters	27
Chapter 4: Experimental Methods	29
4.1 – StereoPIV Theory	29
4.2 – Experimental StereoPIV Setup	32
4.2.1 – Cameras and Optics	32
4.2.2 – Testing Fixture and Components	33
4.2.3 – LabVIEW Code.....	34
4.3 – Image Capture.....	35
4.4 – Healthy Human Analysis Settings	35
4.4.1 – Creating Calibration Files	37
4.4.2 – Stereo AutoMapping	37
4.4.3 – StereoPIV Processing Parameters.....	39
4.5 – Emphysemic Human Analysis Settings	40
Chapter 5: Experimental Validation.....	41
5.1 – CFD Expanding Boiling Flask Model	41
5.1.1 – Model Creation	41
5.1.2 – Fluent Simulation.....	41
5.1.2.1 – Input Parameters	41
5.1.2.2 – Fluent UDF	42

5.1.3 – Mesh Independence.....	44
5.1.4 – CFD Results	45
5.1.4.1 – 1 st Location – Center Plane of Bulb.....	46
5.1.4.2 – 2 nd Location – 11 mm from Center Plane of Bulb	48
5.2 – Experimental Methods Used for Validation	49
5.2.1 – Compliant Model Creation.....	49
5.2.2 – Experimental Setup.....	49
5.2.4 – Insight 3G.....	50
5.2.4.1 – Image Capture.....	50
5.2.4.2 – Creating Calibration Files	51
5.2.4.3 – StereoPIV Processing Parameters.....	53
5.2.5 – StereoPIV Results Compared to CFD.....	53
5.2.5.1 – 1 st Location – Center Plane of Bulb.....	53
5.2.5.2 – 2 nd Location – 11mm from Center Plane of Bulb.....	59
5.3 – Conclusions About Boiling Flask Experiments.....	63
Chapter 6: StereoPIV Results in Alveolus Models.....	66
6.1 – Experimental Healthy Human Model	66
6.1.1 – Locations of Potential Recirculation.....	66
6.1.2 – 3-Dimensional Flow Fields.....	69
6.2 – In Vivo Healthy Human Predictions.....	72
6.2.1 – Scaling Experimental Healthy Results to <i>In Vivo</i>	72
6.3 – Experimental Emphysemic Human Model.....	78
6.4 – In Vivo Emphysemic Human Predictions.....	81
6.4.1 – Scaling Experimental Emphysemic Results to <i>In Vivo</i>	81
6.5 – Comparison between Healthy and Emphysemic Models.....	85
6.5.1 – Geometric Differences	85

6.5.2 – Comparison of Flow Conditions	86
6.5.3 – Normal Healthy Breathing vs. Normal Emphysemic Breathing	87
6.5.4 – Normal Healthy Breathing vs. Heavy Healthy Breathing	90
6.5.5 – Heavy Healthy Breathing vs. Normal Emphysemic Breathing	91
Chapter 7: Conclusions and Discussion	94
7.1 – Remarks	94
7.2 – Healthy versus Emphysemic Models	95
7.2.1 – Discussion of <i>In Vivo</i> Predictions	96
7.2.1.1 – Residence Time	96
7.2.1.2 – Particle Penetration Depth	97
7.2.1.3 – Particle Deposition	98
7.2.1.4 – Flow Rate	98
7.2.1.5 – Velocity Fields	99
7.3 – Limitations of Work	99
7.4 – Future Work	100
References	101

Table of Figures

Figure 1.1 - (A) Subdivisions of the pulmonary airways and (B) the acinus region of the human lung (Netter 1979).....	1
Figure 1.2 - Illustrations of (A) healthy and (B) emphysemic alveoli (Metro Health System 2008).	1
Figure 1.3 - Axisymmetric alveolus used by Tsuda et al. (1995) and Tippe and Tsuda (2000). QA = alveolar flow rate, QD = ductal flow rate, RA = alveolar radius, RD = ductal radius, γ = opening half angle.	2
Figure 1.4 - Symmetric channel geometry used by Darquenne (2001).	3
Figure 1.5 - Central channel geometry used by Karl et al. (2004).....	3
Figure 1.6 - (A) Alveolated duct geometry used by Sznitman et al. (2007a) and (B) Truncated octahedron geometry used by Sznitman et al. (2009).....	3
Figure 1.7 - Alveolated duct model used by van Ertbruggen et al. (2008). (A) Model dimensions, (B) experimental setup, and (C) numerical model.....	4
Figure 1.8 - Idealized geometry used by Oakes (2008). Healthy model (A) front and (B) top. Emphysemic model (C) front and (D) top.	4
Figure 1.9 - Honeycomb geometry used by Kumar et al. (2008). (A) Geometry representing generations 18 to 22 and (B) terminating alveolar sac representing the 23rd generation.....	4
Figure 2.1 - (A) Healthy human lung obtained from a fixed cadaver at RIT. (B) Piece 1 and (C) piece 2 from the lateral basal lobe of the left lung. (D) Schematic representing the casting locations in the healthy human left lung (Netter 1979).	9
Figure 2.2 - Microscope images of (A) piece 1 and (B) piece 2 from the healthy human lung cast (red lines represent 1 mm). Circled portion was scanned and reconstructed (see section 2.3.1).	9
Figure 2.3 - (A) Human emphysemic lung obtained from the cadaver lab at RIT. (B) Superior lobe cast and (C) Anterior lobe cast of the left lung. (D) Schematic representing the locations of casting in the human emphysemic left lung (Netter 1979).....	10

Figure 2.4 - (A), (B), (C) Sections chosen for further analysis from the human emphysema lung cast. (B) Section scanned and reconstructed (see section 2.3.1). (Red lines represent 1 mm). Circled portion represents the final experimental emphysemic human model section. 11

Figure 2.5 - 3D Doctor ROI selected to include the entire model. 12

Figure 2.6 - (A) Original whole healthy human reconstruction and (B) circled region selected for final model. (Both reconstructions are shown prior to 2D slice editing)..... 13

Figure 2.7 - (A) Portion of the original emphysemic human reconstruction and (B) circled region selected for final model. (Both reconstructions are shown prior to 2D slice editing) 14

Figure 2.8 - (A) 2D slice showing where edits need to occur and (B) the final edited image..... 14

Figure 2.9 - (A) Portion of a healthy human reconstruction with circles showing where holes and wart structures exist and (B) the same reconstruction using edited 2D images..... 15

Figure 2.10 - Progression of obtaining a final 3D digital model from the original healthy cast (shown from two different angles)..... 16

Figure 2.11 - Progression of obtaining a final 3D digital model from the original emphysemic cast. 16

Figure 2.12 - Process of creating an inlet duct on the healthy human model using SolidWorks. 17

Figure 2.13 - Progression of translating duct onto healthy human model 17

Figure 2.14 - (Top) Original emphysemic model with the (Bottom) additions made to fill in voids..... 18

Figure 2.15 - Healthy human final model (A) front, (B) top, and (C) right views (inlet duct measures 113.6 mm prior to scaling). Emphysemic human final model (D) front, (E) top, and (F) right views (inlet duct measures 290.32 mm prior to scaling). 18

Figure 2.16 - Images of (A) healthy and (B) emphysemic models representing dimensions used for in vivo scaling. The yellow bar in (B) represents 1 mm. 19

Figure 2.17 - Healthy human physical prototype model (A) top, (B) bottom, (C) left, and (D) right views..... 21

Figure 2.18 - Multiple views of the emphysemic human physical prototype model..... 21

Figure 2.19 - Compliant experimental model of the healthy human lung.	21
Figure 2.20 - Compliant experimental model of the emphysemic human lung.....	22
Figure 3.1 - Velocity profiles for varying Wo occurring (A) in the expanding bulb at $z = 0.375$ mm and (B) in the rigid duct at $z = 0.55$ mm. Velocity profiles for varying Re occurring (C) in the expanding bulb and (D) in the rigid duct.	24
Figure 3.2 - Convergence plots for (A) Womersley and (B) Reynolds numbers showing that velocity profiles converge prior to reaching the maximum experimental $Wo = 0.07$ and before the maximum experimental $Re = 0.24$. NL refers to the non-dimensional locations in Figure 3.1.	25
Figure 4.1 - Fundamentals of stereoPIV (Dynamics 2010). The x and z directions are depicted as right and up, respectively, while the y direction is out of the plane.	29
Figure 4.2 - Overlap area with interrogation region resulting from each cameras field of view (Dynamics 2010).....	30
Figure 4.3 - Processed 2D vector maps from each camera (Dynamics 2010).....	30
Figure 4.4 - Typical interrogation region used for image processing.	31
Figure 4.5 - (A) Identify particle mask, (B) determine position change, and (C) calculate vector based on known displacement / known ΔT (TSI 2009).....	31
Figure 4.6 - Image processing theory representing a single correlation peak (LaVision 2009)...	31
Figure 4.7 - Resulting 3D vector map (Dynamics 2010).....	32
Figure 4.8 - Experimental stereoPIV setup developed in our lab.	32
Figure 4.9 - LabVIEW block diagram used to expand and contract the experimental models. ...	34
Figure 4.10 - Capture settings for stereoPIV experiments.....	35
Figure 4.11 - LabVIEW output for a healthy human experiment displaying the input parameters required to match in vivo conditions (4 second period and 35% expansion resulting in an inhale flow rate of 1.94 mL/sec).	36
Figure 4.12 - (A) Left and (B) right perspective calibration files for the 2nd location in the healthy human model.....	37

Figure 4.13 - Pixel to length conversion for the 2nd location created from the information in Figure 4.13.	37
Figure 4.14 - Images prior to translating (grid represents 50 pixels).....	37
Figure 4.15 - Stereo AutoMapping results for the 2nd location in the healthy model.	38
Figure 4.16 - Perspective calibration for the 2 nd location after stereo AutoMapping.....	38
Figure 4.17 - Processing mask for the (A) 4th and (B) 6th locations in the healthy model.	38
Figure 4.18 - StereoPIV processor used for image processing.....	39
Figure 4.19 - (A) Local vector validation parameters and (B) vector conditions parameters for processing.	39
Figure 4.20 - LabVIEW output for an emphysemic human experiment displaying the input parameters required to match in vivo conditions (4 second period and 30.08% expansion resulting in an inhale flow rate of 1.94 mL/sec).	40
Figure 5.1 - (A) Glass boiling flask and (B) SolidWorks model used for CFD simulations.....	41
Figure 5.2 - Flowchart of UDF written to expand and contract boiling flask model.	43
Figure 5.3 - Various base meshes created in Harpoon.....	44
Figure 5.4 - Velocity profiles at time = 1.0 second for varying base level meshes occurring (A) in the stationary duct (y = 54.5 mm) and (B) in the center of the moving wall bulb (y = 26.8 mm).	45
Figure 5.5 - (A) Harpoon 0.90 base level mesh of the bulb. (B) Top mesh view of a cross section of the center of the model and (C) side view of the center cross section of the model.	45
Figure 5.6 - (A) View representing both laser sheet planes, (B) view displaying the two rake locations, and (C) front view of the model showing all four rake locations.....	46
Figure 5.7 - Fluent grid showing top and bottom rakes.....	46
Figure 5.8 - Velocity profile plots at the 1st location (center plane of the bulb) for the (A) top rake (y = 13.4 mm above the diameter) and (B) bottom rake (y = 3.4 mm above the diameter) for time = 1.0 second.	47

Figure 5.9 - Velocity profile plots at the 1st location (center plane of the bulb) for the (A) top rake ($y = 13.4$ mm above the diameter) and (B) bottom rake ($y = 3.4$ mm above the diameter) for time = 0.5 seconds.	47
Figure 5.10 - 2nd Location showing top and bottom rakes.	48
Figure 5.11 - Velocity profile plots at the 2nd location (11 mm from the center of the bulb) occurring at a flow time of 1.0 second for the (A) top rake ($y = 13.4$ mm above the diameter) and (B) bottom rake ($y = 3.4$ mm above the diameter).....	48
Figure 5.12 - Velocity profile plots at the 2nd location (11 mm from the center of the bulb) occurring at a flow time of 0.5 seconds for the (A) top rake ($y = 13.4$ mm above the diameter) and (B) bottom rake ($y = 3.4$ mm above the diameter).	49
Figure 5.13 - Compliant boiling flask model used for validation (model is sitting on flat surface).	49
Figure 5.14 - TSI capture settings used for experimental validation.	50
Figure 5.15 - Perspective calibration parameters used for 1st location.	51
Figure 5.16 - Perspective calibration parameters used for 2nd location.	51
Figure 5.17 - Stereo AutoMapping results for the (Top) 1st location and (Bottom) 2nd location.	52
Figure 5.18 - Final calibration files for (Left) 1st location and (Right) second location after stereo AutoMapping. The red boxes represent the final conversion factors.	52
Figure 5.19 - Processing masks for (A) 1 st location and (B) 2 nd location.	53
Figure 5.20 - LabVIEW outputs for the 1st locations (A) 1st set, (B) 2nd set, and (C) 3rd set. ..	53
Figure 5.21 - Top and bottom rake locations for the 1st laser sheet location (center of the bulb model).	54
Figure 5.22 - StereoPIV velocity profiles for time = 1.0 second with the predicted CFD results (shown as black solid lines) for the (A) top rake location ($y = 13.4$ mm above the diameter) and (B) the bottom rake location ($y = 3.4$ mm above the diameter) for the 1 st laser sheet	

location (Purple = velocity magnitude, Blue = x-velocity, Red = y-velocity, Green = z-velocity. Different sets are indicated by dashed lines, solid lines, and circles). 55

Figure 5.23 - StereoPIV velocity profiles for time = 0.5 seconds with the predicted CFD results (shown as black solid lines) for the (A) top rake location ($y = 13.4$ mm above the diameter) and (B) the bottom rake location ($y = 3.4$ mm above the diameter) for the 1st laser sheet location (Purple = velocity magnitude, Blue = x-velocity, Red = y-velocity, Green = z-velocity. Different sets are indicated by dashed lines, solid lines, and circles). 55

Figure 5.24 - (A) Scale inserted into compliant model and (B) scale removed from model. (Both occur in the center plane of the model)..... 56

Figure 5.25 - StereoPIV velocity profiles using the measured conversion factor (1 pix = 64.24 μm) for time = 1.0 second with the predicted CFD results (shown as black solid lines) for the (A) top rake location and (B) bottom rake location for the 1st laser sheet location (Purple = velocity magnitude, Blue = x-velocity, Red = y-velocity, Green = z-velocity. Different sets are indicated by dashed lines, solid lines, and circles). 58

Figure 5.26 - StereoPIV velocity profiles using the measured conversion factor (1 pix = 64.24 μm) for time = 0.5 seconds with the predicted CFD results (shown as black solid lines) for the (A) top rake location and (B) bottom rake location for the 1st laser sheet location (Purple = velocity magnitude, Blue = x-velocity, Red = y-velocity, Green = z-velocity. Different sets are indicated by dashed lines, solid lines, and circles). 58

Figure 5.27 - LabVIEW outputs for the 2nd locations (A) 1st set, (B) 2nd set, and (C) 3rd set. . 59

Figure 5.28 - Top and bottom rake locations for the 2nd laser sheet location..... 60

Figure 5.29 - StereoPIV velocity profiles for time = 1.0 second with the predicted CFD results (shown as black solid lines) for the (A) top rake location ($y = 13.4$ mm above the diameter) and (B) the bottom rake location ($y = 3.4$ mm above the diameter) for the 2nd laser sheet location (Purple = velocity magnitude, Blue = x-velocity, Red = y-velocity, Green = z-velocity. Different sets are indicated by dashed lines, solid lines, and circles). 60

Figure 5.30 - StereoPIV velocity profiles for time = 0.5 seconds with the predicted CFD results (shown as black solid lines) for the (A) top rake location ($y = 13.4$ mm above the diameter) and (B) the bottom rake location ($y = 3.4$ mm above the diameter) for the 2nd laser sheet

location (Purple = velocity magnitude, Blue = x-velocity, Red = y-velocity, Green = z-velocity. Different sets are indicated by dashed lines, solid lines, and circles).	61
Figure 5.31 - StereoPIV velocity profiles using the measured conversion factor (1 pix = 61.36 μm) for time = 1.0 second with the predicted CFD results (shown as black solid lines) for the (A) top rake location and (B) bottom rake location for the 2 nd laser sheet location (Purple = velocity magnitude, Blue = x-velocity, Red = y-velocity, Green = z-velocity. Different sets are indicated by dashed lines, solid lines, and circles).	62
Figure 5.32 - StereoPIV velocity profiles using the measured conversion factor (1 pix = 61.36 μm) for time = 0.5 seconds with the predicted CFD results (shown as black solid lines) for the (A) top rake location and (B) bottom rake location for the 2 nd laser sheet location (Purple = velocity magnitude, Blue = x-velocity, Red = y-velocity, Green = z-velocity. Different sets are indicated by dashed lines, solid lines, and circles).	62
Figure 5.33 - Difference in velocity profile caused by non-uniform expansion.....	65
Figure 6.1 - (A) Isometric and (B) top views of the chosen locations for data analysis for the healthy human model.....	66
Figure 6.2 - Regions where recirculation would be most likely to occur.	66
Figure 6.3 - Raw PIV images (showing the distribution of particles) of the 6th and 8th locations representing regions where recirculation would occur.	67
Figure 6.4 - Zoomed in views of the (A) vector and (B) streamline plots (contoured by velocity magnitude) for the 6th location in the healthy human model (refer to Figure 6.1 for the 6th location with respect to the whole model).	67
Figure 6.5 - Isometric view of the 6th location illustrating the z vectors.	68
Figure 6.6 - Zoomed in views of the (A) vector and (B) streamline plots (contoured by velocity magnitude) for the 8th location in the healthy human model (refer to Figure 6.1 for the 8th location with respect to the whole model).	68
Figure 6.7 - Isometric view of the 8th location illustrating the z vectors.	69

Figure 6.8 - 2D experimental velocity vector results for the six analyzed locations (A – F) corresponding to the 2nd through the 12th locations (see Figure 6.1A for locations). Each image is contoured by velocity magnitude and is independent of each location..... 70

Figure 6.9 - All six planar locations analyzed showing (A) contours and (B) vectors contoured by the global velocity magnitude..... 70

Figure 6.10 - Exploded view of all six planar locations analyzed showing (A) contours and (B) vectors contoured by the global velocity magnitude. (The maximum velocity that occurred in the planes analyzed was 9.5 mm/sec). 71

Figure 6.11 - Top view of the healthy human model representing the magnitude and direction of the z-component of velocity..... 71

Figure 6.12 - 2D *in vivo* velocity vector results for the six analyzed locations (A – F) corresponding to the 2nd through the 12th locations (see Figure 6.1A for locations) for $Re = 0.009$ 74

Figure 6.13 - In vivo results for all six planar locations analyzed showing (A) contours and (B) vectors contoured by the global velocity magnitude for $Re = 0.009$. (The maximum velocity that occurred in the planes analyzed was 0.22 mm/sec) 75

Figure 6.14 - Exploded view of all six planar locations analyzed showing (A) contours and (B) vectors contoured by the in vivo global velocity magnitude for a $Re = 0.009$. (The maximum velocity that occurred in the planes analyzed was 0.22 mm/sec) 75

Figure 6.15 - Top view of the healthy human model representing the in vivo magnitude and direction of the z-component of velocity (for $Re = 0.009$). 76

Figure 6.16 - 2D in vivo velocity vector results for the six analyzed locations (A – F) corresponding to the 2nd through the 12th locations (see Figure 6.1A for locations) for $Re = 0.035$ 76

Figure 6.17 - In vivo results for all six planar locations analyzed showing (A) contours and (B) vectors contoured by the global velocity magnitude for $Re = 0.035$. (The maximum velocity that occurred in the planes analyzed was 0.89 mm/sec) 77

Figure 6.18 - Exploded view of all six planar locations analyzed showing (A) contours and (B) vectors contoured by the in vivo global velocity magnitude for a $Re = 0.035$. (The maximum velocity that occurred in the planes analyzed was 0.89 mm/sec) 77

Figure 6.19 - Top view of the healthy human model representing the in vivo magnitude and direction of the z-component of velocity (for $Re = 0.035$). 78

Figure 6.20 - (A) Isometric and (B) top views of the chosen locations for data analysis for the emphysemic human model. 78

Figure 6.21 - 2D velocity vector results for the five analyzed locations (A – E) corresponding to the 2nd through the 10th locations (see Figure 6.20A for locations). Each image is contoured by velocity magnitude and is independent of each location. 79

Figure 6.22 - All five planar locations analyzed showing (A) contours and (B) vectors contoured by the global velocity magnitude. (The maximum velocity that occurred in the planes analyzed was 6.4 mm/sec) 80

Figure 6.23 - Exploded view of all five planar locations analyzed showing (A) contours and (B) vectors contoured by the global velocity magnitude. (The maximum velocity that occurred in the planes analyzed was 6.4 mm/sec) 80

Figure 6.24 - Top view of the emphysema human model representing the magnitude and direction of the z-component of velocity. 81

Figure 6.25 - 2D in vivo velocity vector results for the five analyzed locations (A – E) corresponding to the 2nd through the 10th locations (see Figure 6.20A for locations) for $Re = 0.035$ 83

Figure 6.26 - In vivo results for all five planar locations analyzed showing (A) contours and (B) vectors contoured by the global velocity magnitude for $Re = 0.035$. (The maximum velocity that occurred in the planes analyzed was 0.21 mm/sec) 83

Figure 6.27 - Exploded view of all five planar locations analyzed showing (A) contours and (B) vectors contoured by the in vivo global velocity magnitude for a $Re = 0.035$. (The maximum velocity that occurred in the planes analyzed was 0.21 mm/sec) 84

Figure 6.28 - Top view of the emphysemic human model representing the in vivo magnitude and direction of the z-component of velocity (for $Re = 0.035$).	84
Figure 6.29 - (A) Healthy and (B) emphysemic experimental prototypes. The circled portion represents the locations in the healthy model most likely to induce recirculation (6 th and 8 th locations).....	86
Figure 6.30 - (A) 10th location in the normal healthy human model ($Re = 0.009$) and the (B) 8th location of the normal emphysemic model ($Re = 0.035$)......	88
Figure 6.31 - 2nd location in the (A) normal healthy human model ($Re = 0.009$) and the (B) normal emphysemic model ($Re = 0.035$)......	89
Figure 6.32 – 10th location for the (A) normal healthy human model ($Re = 0.009$) and the (B) heavy healthy model ($Re = 0.035$)......	90
Figure 6.33 - 2nd location for the (A) normal healthy human model ($Re = 0.009$) and the (B) heavy healthy model ($Re = 0.035$)......	91
Figure 6.34 - (A) 10th location in the healthy heavy human model and the (B) 8th location of the normal emphysemic model (in vivo $Re = 0.035$).	92
Figure 6.35 – 2nd location in the (A) heavy healthy human model and the (B) normal emphysemic model (in vivo $Re = 0.035$)......	93

Chapter 1: Introduction and Background Information

1.1 – Anatomy of the Lung

The human respiratory tract is divided into three sections: the upper respiratory tract (consisting of the nasal passages and throat), the respiratory airways (made up of the larynx, trachea, bronchi, and bronchioles), and the lungs (consisting of respiratory bronchioles, alveolar ducts, alveolar sacs, and alveoli). While most of the respiratory tract exists mostly to direct air to the lungs, the alveoli are the only part of the lung where oxygen and carbon dioxide exchange occurs (referred to as the pulmonary region). Each human lung contains approximately 300 million

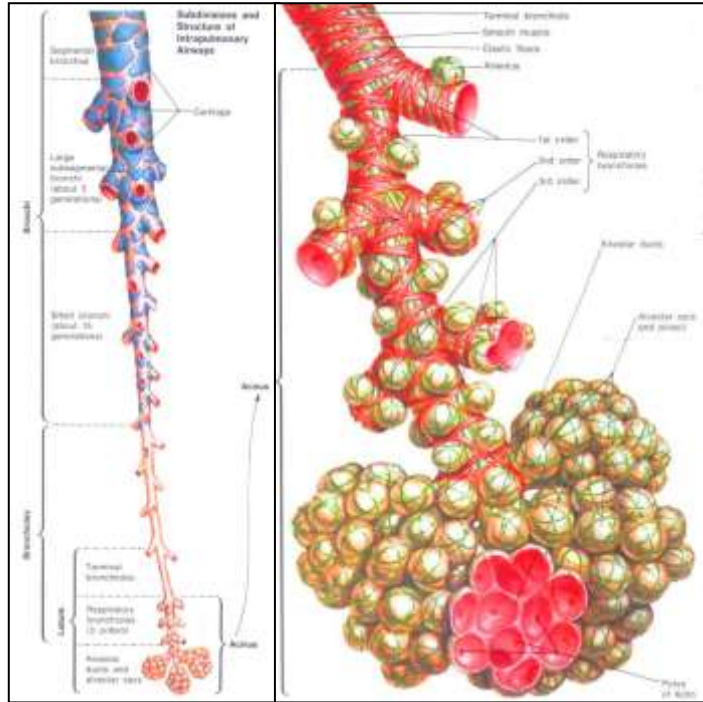


Figure 1.1 - (A) Subdivisions of the pulmonary airways and (B) the acinus region of the human lung (Netter 1979).

alveoli with an average effective airway diameter of 200 to 300 microns (Angus and Thurlbeck 1972). Figure 1.1 illustrates the anatomy of the most distal regions of the human lung; the bronchioles and acinus regions (occurring between generations 20 and 23). Understanding the fluid mechanics occurring in the acinus region is of high importance because it is the region where gas exchange occurs.

Emphysema is a chronic obstructive disease of the lung that occurs in the acinus region. It is classified as a chronic obstructive pulmonary disease (COPD). Over time, septa walls break down and air sacs lose their elasticity causing air to be trapped in the sacs. This increases the overall volume of the alveolar sacs and

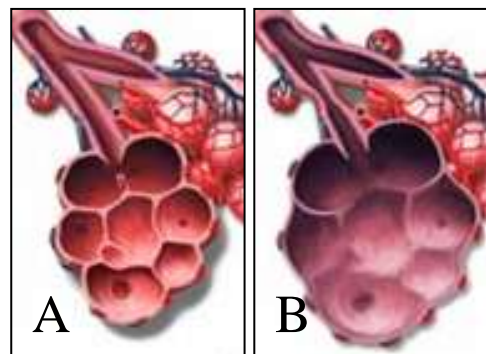


Figure 1.2 - Illustrations of (A) healthy and (B) emphysemic alveoli (Metro Health System 2008).

decreases the surface area through which gas exchange occurs. It becomes increasingly difficult to expel carbon dioxide from the lungs causing a starvation for oxygen. Figure 1.2 depicts the differences in geometry between healthy and emphysemic alveoli. It is seen that the septa walls of the emphysemic sac have deteriorated causing individual alveoli to join into a single large alveoli. Fifteen million Americans are currently affected by emphysema/COPD with 80-90% of the cases caused by smoking (Sciences 2009).

Particle deposition in the pulmonary regions of the lung is not well understood; mainly because the current models do not reflect *in vivo* geometry. In order to accurately predict deposition in various regions, the characteristics that affect deposition need to first be understood. This includes fluid flow, lung morphology, breathing conditions, and particle concentrations or dose.

1.2 – Alveolar Numerical and Experimental Models Found in Literature

Many studies have examined the complex flow patterns in the pulmonary regions with increasingly more sophisticated geometries. Tsuda et al. (1995) were some of the first researchers to study fluid mechanics in the alveolar region of the lung. They developed a moving boundary circular channel geometry surrounded by a torus, an axisymmetric representation of an alveolus (Figure 1.3), and performed numerical simulations to predict the fluid flow in various regions of the lung. The dimensions of the torus were varied to depict various lung generations. The ratio of the depth, D , distance from the mouth opening to the bottom of the torus, to the mouth diameter, MD , distance of the mouth opening perpendicular to the depth, (D/MD) , ranged from 0.50 to 0.87. A terminating sac, however, was not studied. This geometry was also used in the experimental research performed by Tippe and Tsuda (2000).

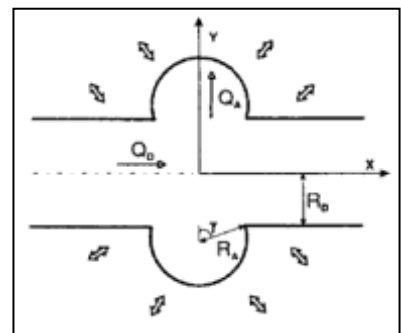


Figure 1.3 - Axisymmetric alveolus used by Tsuda et al. (1995) and Tippe and Tsuda (2000). Q_A = alveolar flow rate, Q_D = ductal flow rate, R_A = alveolar radius, R_D = ductal radius, γ = opening half angle.

Recently, more complex geometries have been created to better understand the complex *in vivo* flow patterns. A comparison was completed on published work that dealt primarily with the

lower generations, ideally terminating alveolar sacs and proximal generations. The following studies were chosen based on similar scopes to the completed work in this document.

Darquenne (2001) performed a computational fluid dynamic (CFD) simulation on a static wall

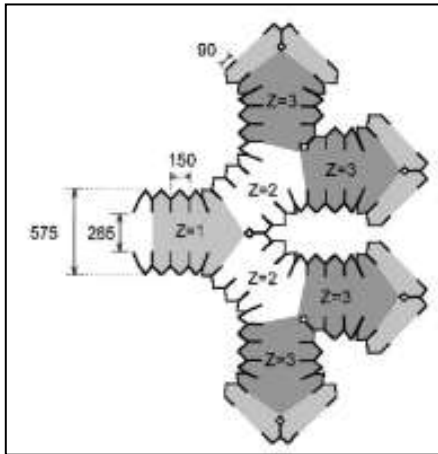


Figure 1.4 - Symmetric channel geometry used by Darquenne (2001).

geometry consisting of a symmetric channel surrounded by triangular shaped alveoli (Figure 1.4) with a D/MD ratio of 1.03; representing generations 18 through 20.

Karl et al. (2004) performed both numerical and experimental procedures on a stationary wall central channel geometry

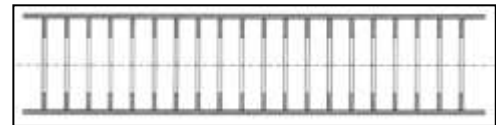


Figure 1.5 - Central channel geometry used by Karl et al. (2004).

surrounded by numerous alveoli with a D/MD ratio

ranging from 0.17 to 1.00 (Figure 1.5). These values are

representative of generations from the acinus region to an alveolated duct.

Sznitman et al. (2007a; 2009) completed moving boundary numerical simulations on an

alveolated duct with a single alveolus

(Figure 1.6A), and on a truncated

octahedron (14-hedron) geometry

(Figure 1.6B). The single alveolus

model's D/MD ratio ranged from 0.87

to 0.90, representing the 15th

generation to the 23rd generation, but

did not contain a terminal sac. In the

octahedron model, however, the D/MD

ranged from 1.02 to 2.00 and

represented generations labeled 3 through 8 (0 representing the transitional bronchioles); and

included a terminating sac.

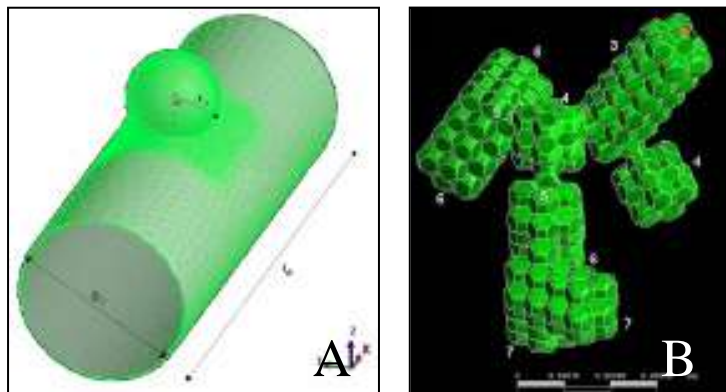


Figure 1.6 - (A) Alveolated duct geometry used by Sznitman et al. (2007a) and (B) Truncated octahedron geometry used by Sznitman et al. (2009).

Similar to Karl et al. (2004), van Ertbruggen et al. (2008) performed both numerical and experimental studies on an alveolated duct. Their model consisted of two alveolated ducts joined by a 145° bend and can be seen in Figure 1.7. The stationary wall geometry had a D/MD of 1.50 representing the 21st generation.

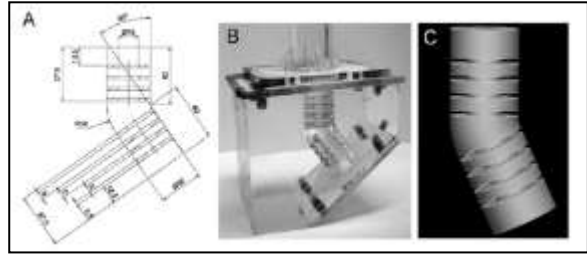


Figure 1.7 - Alveolated duct model used by van Ertbruggen et al. (2008). (A) Model dimensions, (B) experimental setup, and (C) numerical model.

Oakes (2010; 2008) presented thesis work pertaining to experimental PIV research on moving

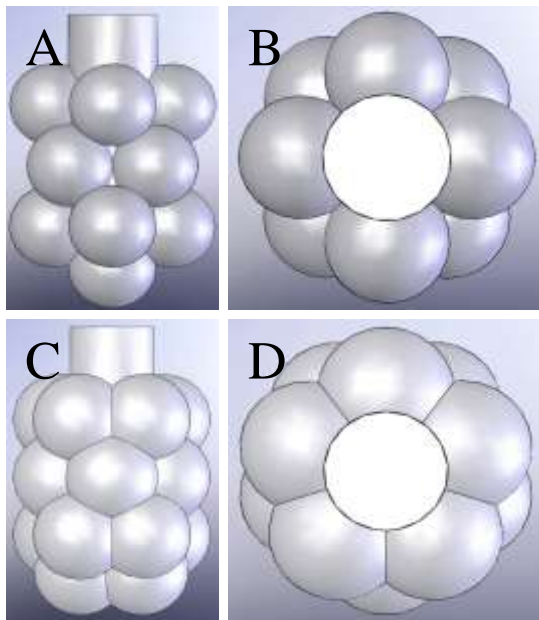


Figure 1.8 - Idealized geometry used by Oakes (2008). Healthy model (A) front and (B) top. Emphysemic model (C) front and (D) top.

boundary models of both healthy and diseased idealized geometry (Figure 1.8). For the healthy model, a D/MD ratio of 0.66 was used, while 0.43 was used for the emphysema model. Both of the models represented terminating sacs, occurring at the 23rd generation.

Similar in geometry to Oakes (2010; 2008), Kumar et al. (2009a) studied two honeycomb-like polygonal structures representing generations 18 to 22 and a terminating 23rd generation (Figure 1.9). Because of the complex geometry, the D/MD ratio was undetermined.

A wide variety of experimental and numerical parameters have also been studied, including constant input flow rates (van Ertbruggen et al. 2008; Darquenne 2001; Karl et al. 2004), non-constant breathing curves (Tsuda et al. 1995; Tippe and Tsuda 2000), and sinusoidal breathing curves (Sznitman et al. 2007a; Sznitman et

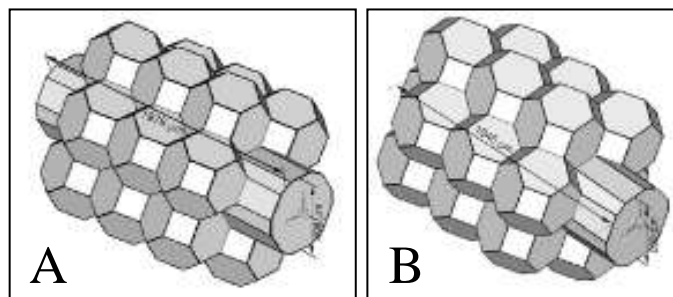


Figure 1.9 - Honeycomb geometry used by Kumar et al. (2008). (A) Geometry representing generations 18 to 22 and (B) terminating alveolar sac representing the 23rd generation.

al. 2009; Kumar et al. 2009a). Oakes (2010; 2008), however, used a spirometry derived breathing curve; indicative of a healthy human breathing under normal conditions.

1.3 – Summary of Alveolar Model Results from the Literature

It was determined that the flow rate ratio (ratio of the alveolar flow rate to the ductal flow rate) is of great importance when studying alveolar flow mechanics. Based on prior results, reversible flow is present when the flow rate ratio is greater than or equal to 0.05 (Tsuda et al. 1995; Tippe and Tsuda 2000; Kumar et al. 2009a). Reversible flows represent fields that are identical on the inhalation and exhalation portions of the breathing curve. If particles were introduced to a reversible flow, their path would be overlapping over a given breathing period (same path for inhalation and exhalation). Sznitman et al. (2007a; 2009), however, reported reversible flow when the ratio was greater than 0.02. Because the scope of the prior work varies from the current work, the flow rate ratio will be used to compare the results.

Zones of recirculating eddies exist where flow separation occurs, causing a swirling effect in the fluid field. Tsuda et al. (1995) and Tippe and Tsuda (2000) presented similar recirculation data with their joint geometry. Both found recirculation regions where the flow rate ratio was small (ranging from 0.01 to 0.02 and from 0.02 to 0.06 for Tsuda et al. (1995) and Tippe and Tsuda (2000), respectively). Both agree, however, that reversible flow is present above a flow rate ratio of 0.06. Darquenne (2001) and Karl et al. (2004), however, found recirculation in all of their studied cases. Sznitman et al. (Sznitman et al. 2007a; Sznitman et al. 2009) reported no recirculation in the terminal sac and the two proximal generations, but found recirculation in generations 19 and 20. Oakes (2008) found reversible flow in both experimental models for all of her trials. Similarly, Kumar et al. (2009a) found no recirculation in their terminating sac, but did, however, find recirculation in the generation immediately proximal.

1.4 – Gaps in the Research

Because *in vivo* geometry is complex and still not well understood, very few studies research the differences that exist between healthy and diseased lungs; including varying geometry or flow rates. Recently, research was compared on the flow fields existing in idealized healthy and emphysematous lungs (Oakes 2008), while the experimental models were created from idealized

geometry dimensions (Weibel 1965; Haefelibleuer and Weibel 1988; Klingele and Staub 1970; Mercer et al. 1987; Kohlhauf et al. 1997; Kohlhauf et al. 2000). Similar to previous studies, however, the geometry used in Oakes (2008) varies significantly from actual *in vivo* geometry.

The complexity of the experimental and numerical geometries has evolved and more models are better representing *in vivo* geometry. Actual *in vivo* geometry, however, has yet to be researched. While most research has used breathing curves similar to realistic breathing conditions, few replicate the *in vivo* breathing curve. It was shown that the input flow parameters have a significant impact on the fluid mechanics within the model. Large flow rate ratios yield radial flows while low ratios show significant recirculation. It is apparent that geometry representing a diseased alveolar sac has varying fluid mechanics, but radial flow is still present for a terminating sac.

1.5 – Scope of the Thesis Work

The goal of this research was to aid in the better understanding of the mechanisms that govern fluid motion and particle transport in the most distal regions of the lung and to compare the differences that exist between *in vivo* healthy and emphysematous models. Specifically, the existence of recirculation regions in each model will be examined experimentally using stereoscopic particle image velocimetry (stereoPIV) techniques and comparisons between healthy and emphysemic geometries made. The following aims were completed to achieve these research goals:

Aim 1 – Create Compliant Hollow Models

Develop two realistic experimental model prototypes (healthy and emphysemic) from *in vivo* human geometries and obtain compliant models of both geometries for use in stereoPIV experiments.

Aim 2 – Develop PIV Setup Capable of 3D Flow Field Analyses

In order to visualize 3D fluid flow in the experimental models, stereoscopic particle image velocimetry (StereoPIV) techniques were employed.

- Develop an experimental setup to accommodate stereoPIV techniques.

- Create a LabVIEW program to monitor and control the expansion and contraction of the compliant experimental models based on desired input parameters.
- Perform a fluid scaling analysis to ensure that the *in vivo* fluid fields are properly represented in the scaled experimental models.
- Validate the stereoPIV setup by comparing the results of a full experimental analysis of simple 3D bulb geometry to the results of a CFD analysis.

Aim 3 – Complete StereoPIV Analysis on Healthy and Emphysematous Models

Using the validated setup in Aim 2, healthy and diseased models were analyzed and compared.

- Compare geometry differences and how the flow fields are affected.
- Analyze experimental and *in vivo* velocity fields for both models. Compare the differences that exist between velocity magnitudes and distributions occurring in each model (for both experimental results and *in vivo* predictions).
- Compare differences that affect particle transport in the flow fields for each model.

Chapter 2: Model Creation

2.1 – Cast Human Lungs

2.1.1 – Healthy Human

Casting techniques of Phalen et al. (1973) were employed to cast human lungs from a fixed cadaver obtained through the Biological Sciences Department at RIT. Healthy lungs were filled with CO₂ to remove residual air then pumped with approximately 80 mL of saline to dissolve the CO₂. 10 mL of 310 RTV was then injected into the lung using a syringe pump which forced the saline to diffuse through the lung membrane. The casted lung was set overnight to cure and remained exposed to air for two weeks to dry out. Once dried, the lung was soaked in a 4M NaOH solution for approximately two weeks to dissolve the tissue and expose the *in vivo* cast. The left lung of a healthy human (Figure 2.1A) was cast in the posterior and lateral basal sections of the lower lobe. Sections of these casts were chosen for further analysis based on geometrical differences and the quality of the cast (Figure 2.1B and Figure 2.1C). Specifically, portions having air bubbles or truncated regions due to improper flow of casting material were eliminated.

Microscope pictures were taken of each of the pieces to determine which sections would be used for final reconstruction. Healthy humans typically have alveolar mouth diameters of approximately 230 to 330 μm (Kohlhauf et al. 2000) or 292 to 336 μm (Haefelibleuer and Weibel 1988) and represent defined bulb structures. Our healthy human casts were within this range, and were measured between 243 and 378 microns. Figure 2.2 represents microscope images of the two casts obtained from the healthy human. An ideal cast contains no air bubbles with defined bulb geometry. Based on the quality of the cast, the existence of uniform alveoli, and the presence of a terminating alveolar sac, the section in Figure 2.2B was chosen as the final healthy human cast model. The circled section was scanned and used to create the final experimental healthy model. Observation of the cast indicated that the terminal sac chosen for analysis was approximately 5 generations distal to the lower left lobar bronchi.

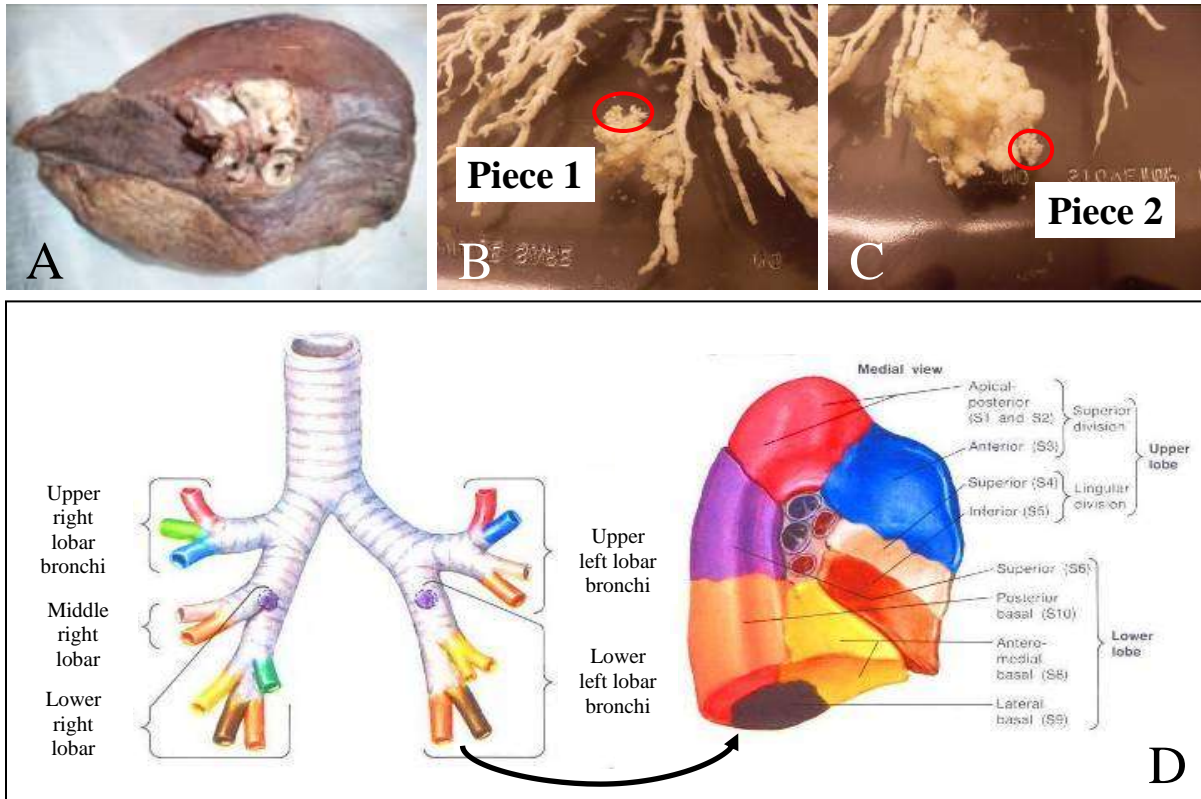


Figure 2.1 - (A) Healthy human lung obtained from a fixed cadaver at RIT. (B) Piece 1 and (C) piece 2 from the lateral basal lobe of the left lung. (D) Schematic representing the casting locations in the healthy human left lung (Netter 1979).

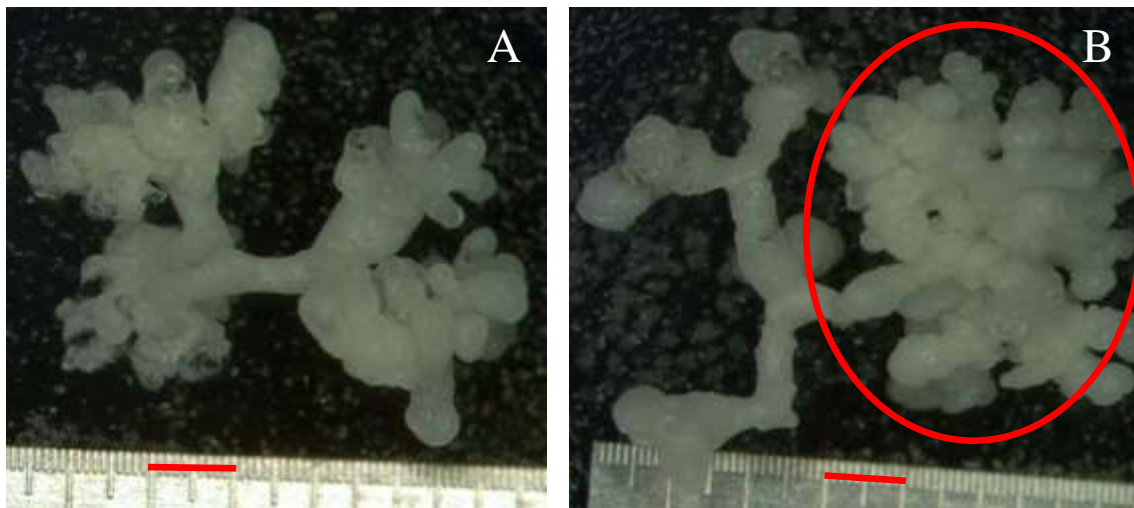


Figure 2.2 - Microscope images of (A) piece 1 and (B) piece 2 from the healthy human lung cast (red lines represent 1 mm). Circled portion was scanned and reconstructed (see section 2.3.1).

2.1.2 – Emphysema Human

A fixed human lung having characteristics of emphysema (Figure 2.3A) was obtained from the cadaver lab at RIT and cast using the same techniques used for the healthy human lung (Phalen et al. 1973). After filling the lung with CO₂, approximately 80 mL of saline was pumped in, followed by 60 mL of 310 RTV. Unlike the healthy lung, two emphysemic lobes were cast. Figure 2.3B represents the emphysemic cast of the superior lower left lobe, while Figure 2.3C represents the cast of the anterior portion of the superior division of the upper left lobe.

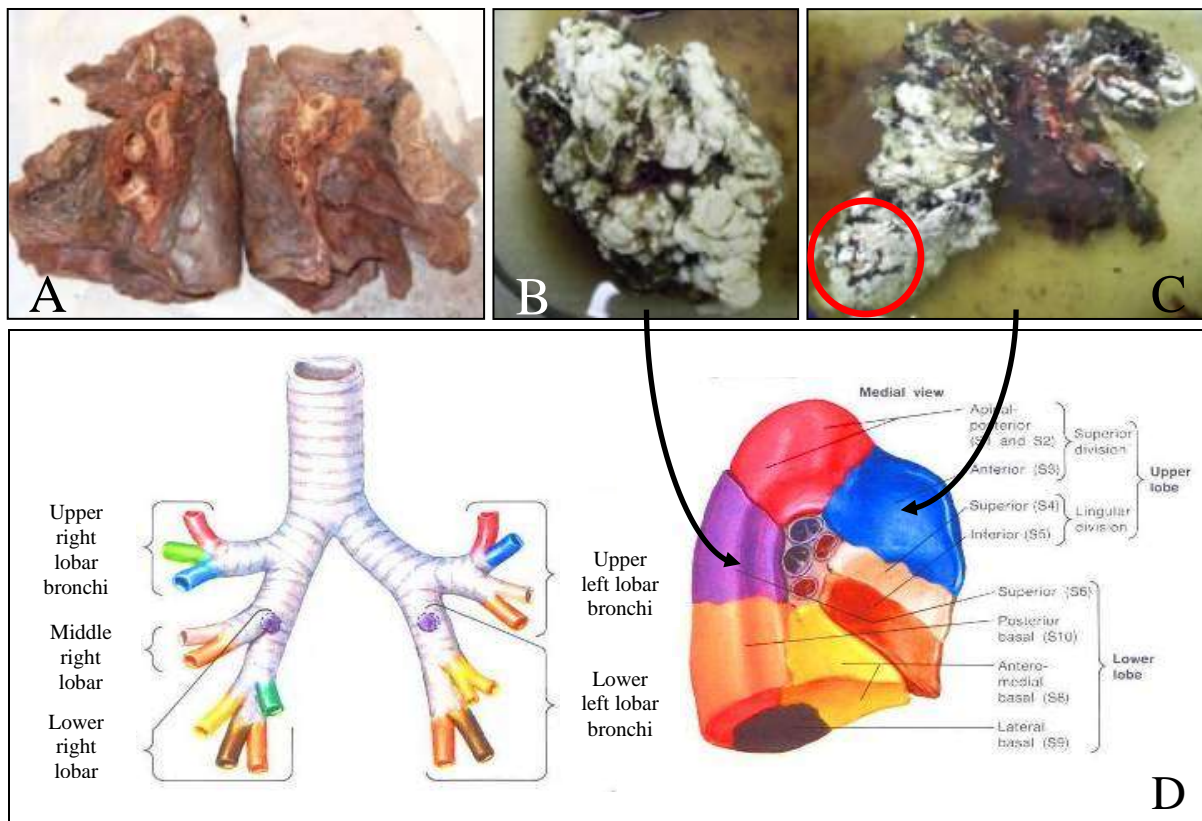


Figure 2.3 - (A) Human emphysemic lung obtained from the cadaver lab at RIT. (B) Superior lobe cast and (C) Anterior lobe cast of the left lung. (D) Schematic representing the locations of casting in the human emphysemic left lung (Netter 1979).

It was determined that pieces obtained from the cast in Figure 2.3C would be used for further analysis. This was based on the geometrical differences that exist in the section and the overall quality of the cast. Again, portions having air bubbles or truncated regions due to improper flow of casting material were eliminated. It was also seen that Figure 2.3B did not contain defined bulb structures that were desired. This portion represented more of a solid structure; which could

be an indication of over expanding and over casting, in addition to disease. The chosen piece (circled region in Figure 2.3C) was then divided into smaller sections for further analysis. Microscope images of three separate pieces can be seen in Figure 2.4.

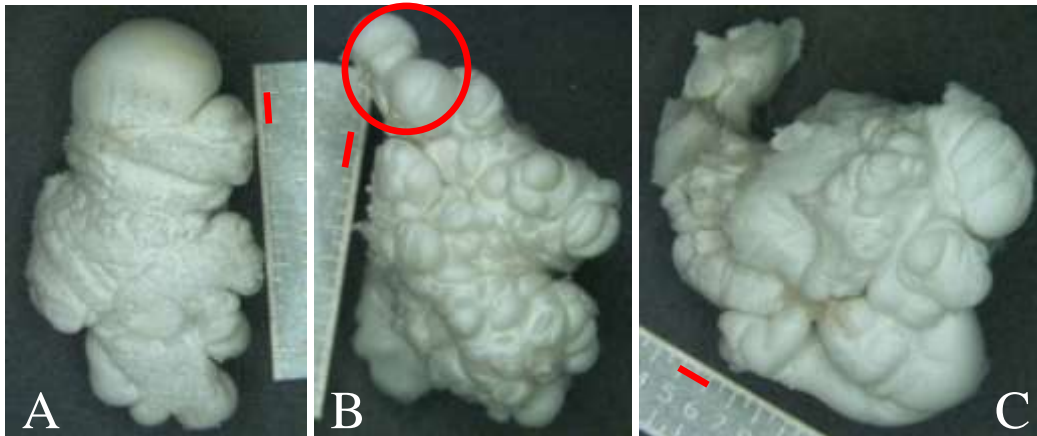


Figure 2.4 - (A), (B), (C) Sections chosen for further analysis from the human emphysema lung cast. (B) Section scanned and reconstructed (see section 2.3.1). (Red lines represent 1 mm). Circled portion represents the final experimental emphysemic human model section.

Based on the quality of the cast, the existence of large alveoli, and the presence of a terminating sac, the section in Figure 2.4B was chosen as the final emphysemic human cast model and was scanned to create the final experimental emphysemic model (circled portion in Figure 2.4B). Literature cites emphysematous diameters ranging from 430 to 830 μm (Kohlhauf et al. 2000) while our model's average effective airway diameter measures 1556 microns; indicating that our model was obtained from a severely diseased lung or was over inflated during the casting process.

2.2 – Obtain Micro-CT Scans of Cast

Micro-CT images were obtained for each of the chosen lung casts to create 3D digital models. A list of micro-CT vendors and their capabilities can be seen in Table 2.1. Micro Photonics was chosen for their high resolution scanner and large image size. Each of the models, healthy (Figure 2.2B) and emphysematous (Figure 2.4B), was sent to Micro Photonics for scanning and 2D images were received three weeks after shipment.

Table 2.1 - Chosen CT scan vendor (gray) compared to other considered vendors.

Vendor	SUNY Upstate	Micro Photonics	Micro Photonics	Scanco Medical
Micro/Nano	Micro	High Resolution Micro	High Resolution Nano	High Resolution Micro
Rates	\$258	\$400-1000	\$1,200	\$350
Resolution (microns)	37	5 to 8	0.4	6
Image Size	3072 x 2048	2k x 2k - 4k x 4k	1280 x 1024	512 x 512 - 4096 x 4096
Image Format	16 bit RAW	n/a	n/a	n/a
Scan Dimensions	8 cm (axial) x 5.4 cm (transaxial)	10mm - 78mm diameter (width)	1mm maximum diameter	36 mm max field of view
	5.4 cm (axial) x 8 cm (transaxial)	155mm diameter (height)	5 mm height	140 mm max length

2.3 – Create 3D Digital Model from 2D Slices

2.3.1 – Reconstruct Whole Model

The entire healthy human cast model (circled portion in Figure 2.2B) was reconstructed using the 2D images to determine a final model location. 3D Doctor (Able Software: Lexington, MA) was used to segment and reconstruct the models. Figure 2.5 shows a single 2D image of the healthy model with the entire model region selected. This is the region that was segmented and reconstructed.

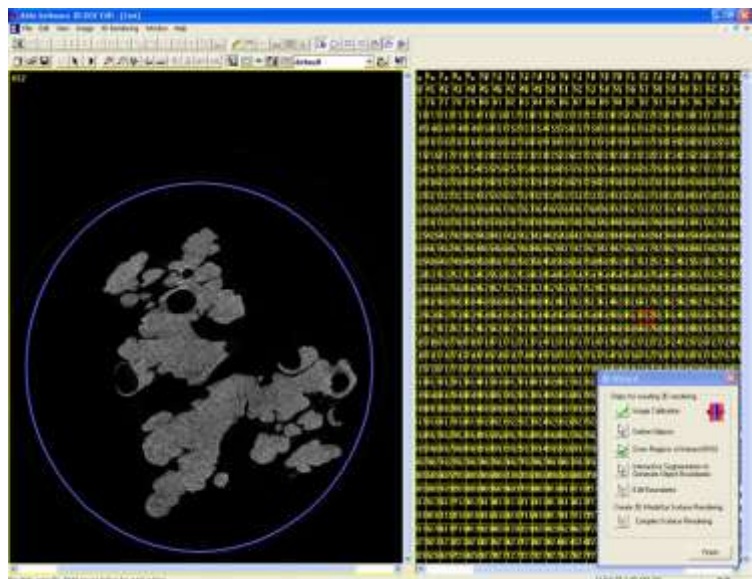


Figure 2.5 - 3D Doctor ROI selected to include the entire model.

After selecting the whole model region, the images were auto-segmented. This is a process that fills in the white areas of the image; indicating which boundaries to create. An image threshold of 45 to 255 was chosen and image smoothing was selected. After successfully segmenting all of the loaded images, a simple surface rendering was completed and exported as a *.obj file. VP-Sculpt (Visible Productions; Fort Collins, CO) was used to open and analyze the rendered 3D model. Figure 2.6A represents the original whole healthy human model that was reconstructed from the healthy cast. From this model, a smaller section was chosen as the final model (Figure 2.6B).

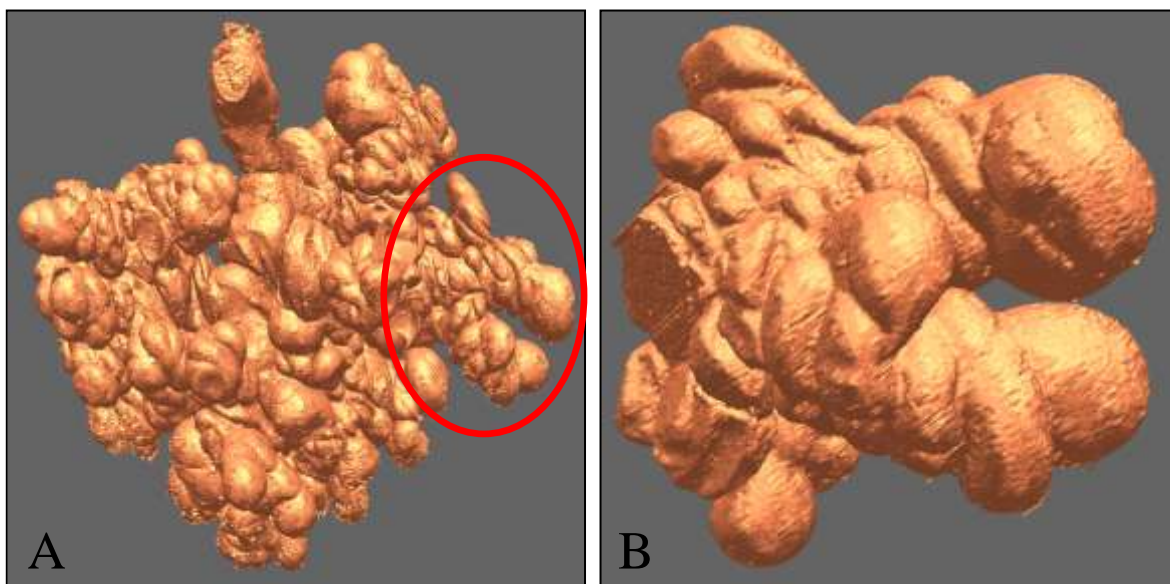


Figure 2.6 - (A) Original whole healthy human reconstruction and (B) circled region selected for final model. (Both reconstructions are shown prior to 2D slice editing)

The same process was used for the emphysemic human model, but the entire model was unable to be reconstructed at once because of its size; too many facets and vertices. Therefore, prior to reconstruction, a region of interest was determined by looking at the physical cast. This smaller selected region was then able to be reconstructed because it contained fewer facets. Figure 2.7A represents a partial reconstruction of the emphysemic human cast and the section chosen for the final emphysemic model (Figure 2.7B).

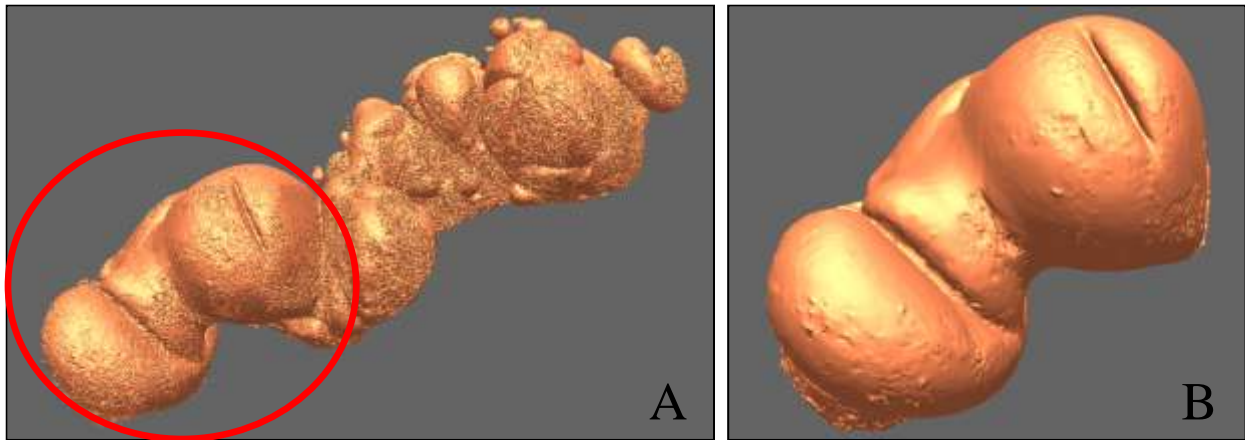


Figure 2.7 - (A) Portion of the original emphysemic human reconstruction and (B) circled region selected for final model. (Both reconstructions are shown prior to 2D slice editing)

2.3.2 – Edit 2D Slices of Final Model Region

Once the final region was chosen, the 2D images were edited for final processing. As seen in Figure 2.8, holes and major voids were present in the 2D slices. Images were edited in ImageJ (National Institutes of Health, USA) to remove the presence of holes in the final model. Also, the edges of the images were cleaned up as to not interfere with the segmentation process. Editing is a very delicate and tedious process that is extremely time consuming, but is also necessary to obtain a usable final model. Figure 2.8A represents a single 2D image that required edits. The holes were filled and the wart like structures removed. Figure 2.8B represents the same 2D slice after editing.

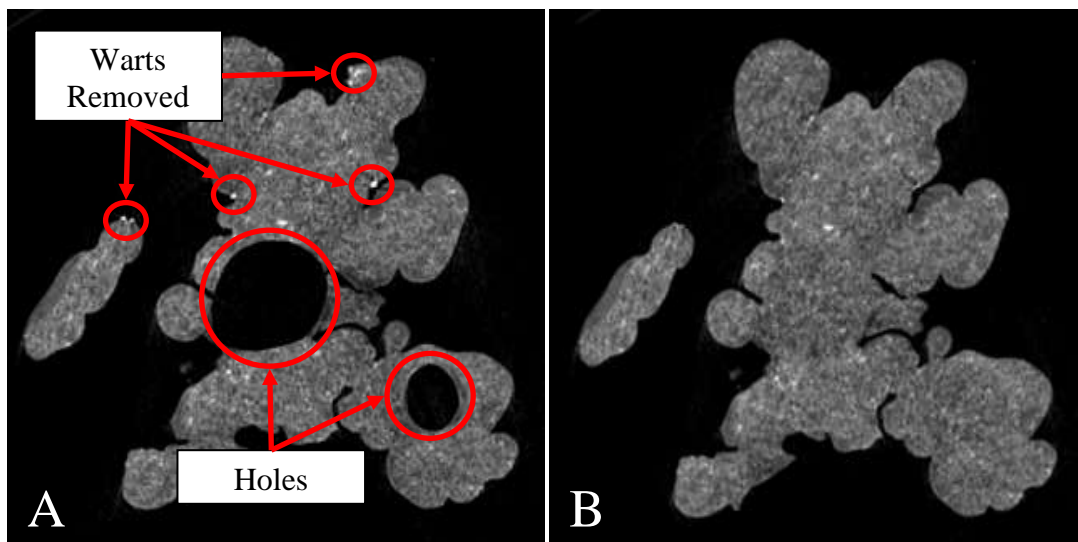


Figure 2.8 - (A) 2D slice showing where edits need to occur and (B) the final edited image.

Figure 2.9 illustrates the significance of editing the images prior to reconstructing. Figure 2.9A displays a portion of a reconstruction using original images with no edits. Large holes are visible and wart like structures can be seen on the surface. Figure 2.9B shows the same reconstruction region using edited images. It can be seen that the holes are filled and a majority of the warts removed. The overall quality of the edited reconstruction has drastically increased and is necessary for obtaining a useable final model.

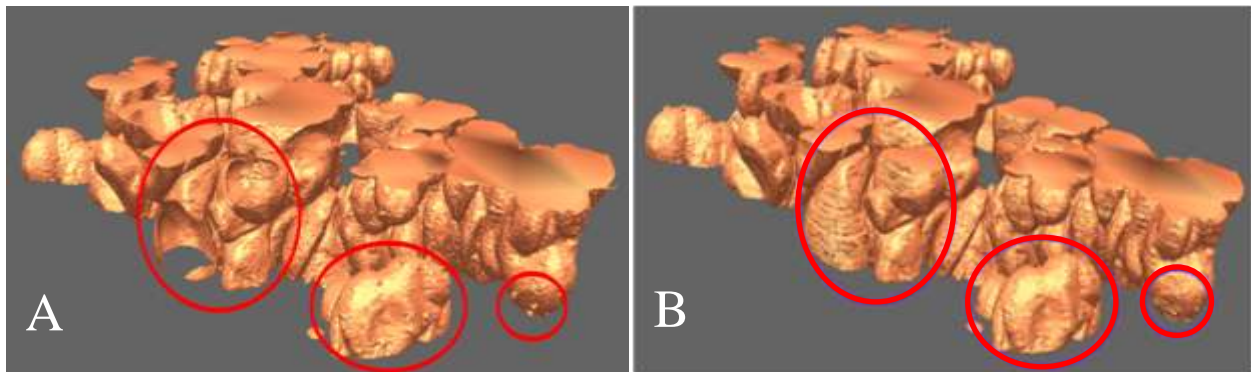


Figure 2.9 - (A) Portion of a healthy human reconstruction with circles showing where holes and wart structures exist and (B) the same reconstruction using edited 2D images.

The 2D editing process described above was applied to all of the images that make up the final model sections (Figure 2.6B and Figure 2.7B) to create a final reconstruction.

2.3.3 – Process Surface of Final Model

After the final models were reconstructed, VP-Sculpt was used to make final edits (fill holes and outer boundaries left by 3D doctor, remove improper facets/vertices, etc.) to the surface of the model and to decrease the number of model facets. This allows the model to be opened in SolidWorks (Dassault Systèmes SolidWorks Corp.; Concord, MA) where a duct was added.

After all of the holes and boundaries were filled, improper faces and vertices were deleted. The process of deleting then filling in holes was repeated until holes/boundaries or improper faces/vertices no longer existed. The model was then smoothed about 50 times using the default parameters to increase the quality of the surface.

Figure 2.10 displays the progression of obtaining a final edited 3D digital model from the original healthy human cast (shown from two different angles) while Figure 2.11 represents the emphysemic human final model progression. The circled regions represent the portions of the models chosen for the final experimental models.

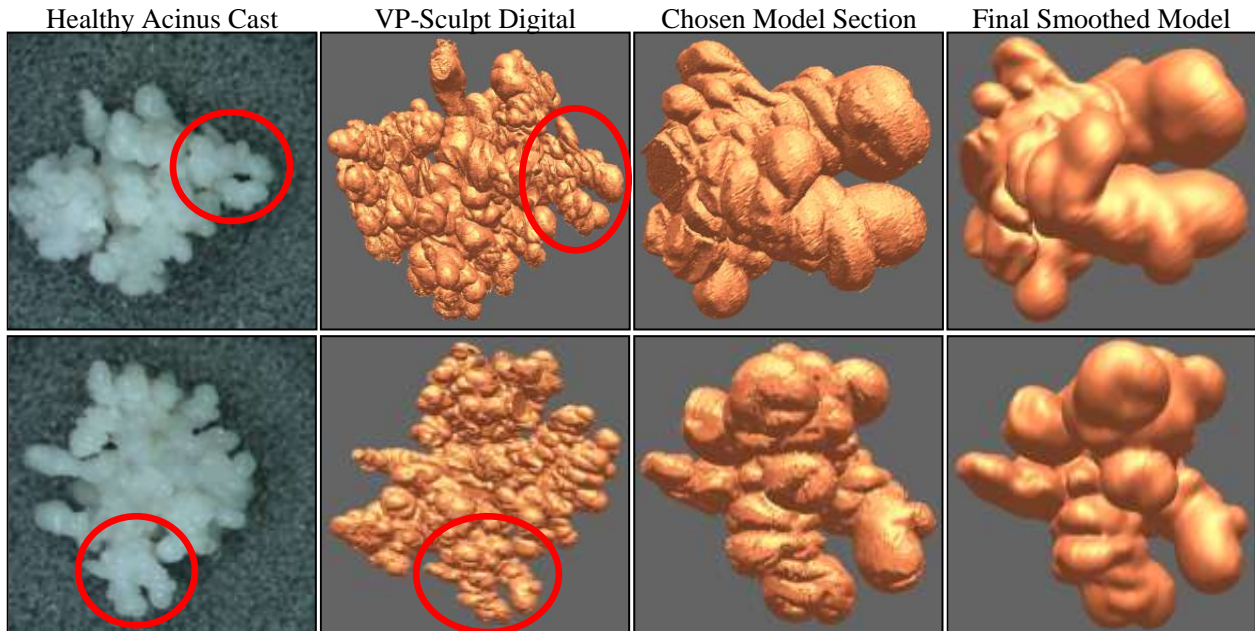


Figure 2.10 - Progression of obtaining a final 3D digital model from the original healthy cast (shown from two different angles).

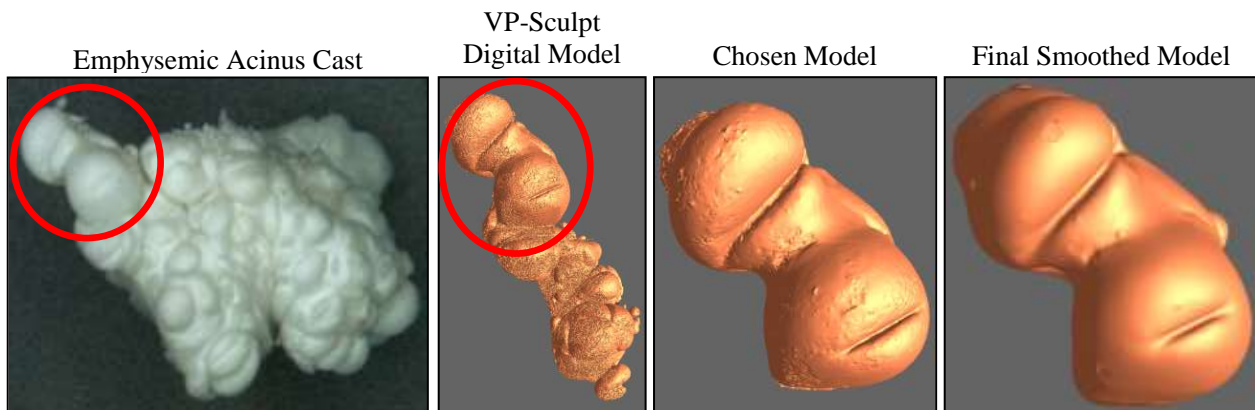


Figure 2.11 - Progression of obtaining a final 3D digital model from the original emphysemic cast.

2.4 – Create Inlet Duct

An inlet duct was added to both of the final models using SolidWorks. In order to open the model in SolidWorks, it was first decimated multiple times to decrease the number of facets

(small pieces that make up the surface of the model). A total of four decimations were completed on the healthy model leaving 27,012 vertices and 54,032 facets (originally 368,238 vertices and 736,416 facets). The emphysemic model was decreased to 23,497 vertices and 46,982 facets (originally 1,589,498 vertices and 3,174,083 facets). The healthy model was imported into SolidWorks as a surface body and an extrusion added based on the surrounding geometry of the model. Figure 2.12 displays the progression of creating an inlet duct using SolidWorks for the healthy human model. The circled sections represent the features that were added at each step.

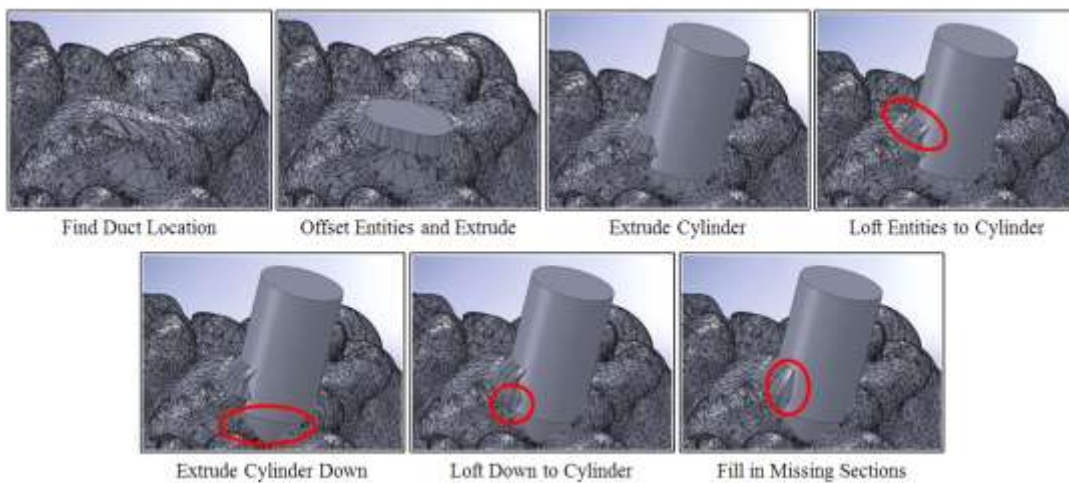
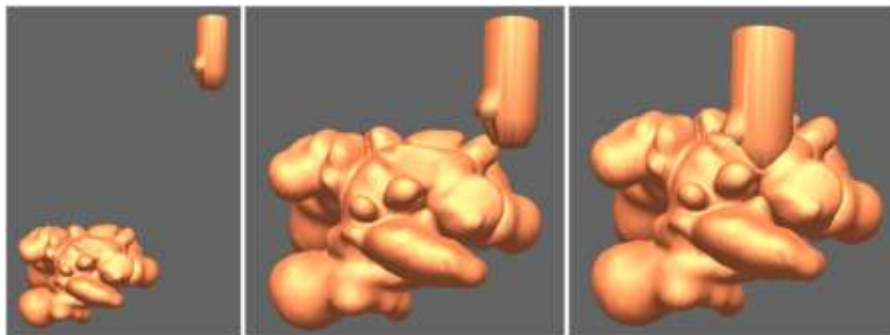


Figure 2.12 - Process of creating an inlet duct on the healthy human model using SolidWorks.

The newly created duct and features were joined to the existing model and was completed using VP-Sculpt. A tedious process of moving the duct into place on the healthy model was completed and is depicted in Figure 2.13.



A duct was also created for the emphysemic model, but further additions were first required. Because of the location of the final model section, portions of the model were cut from the rest of the geometry leaving flat surfaces where material exists in the whole model. Therefore, the missing bulb structures were recreated manually (Figure

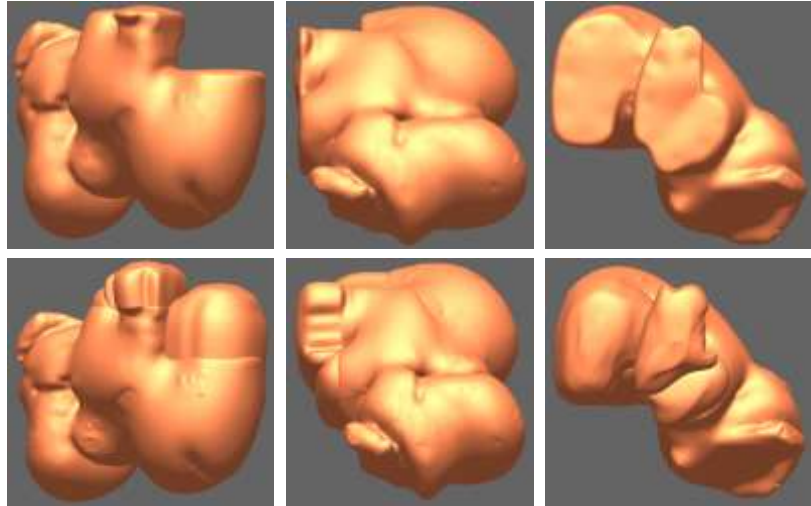


Figure 2.14 - (Top) Original emphysemic model with the (Bottom) additions made to fill in voids.

2.14). Figure 2.15 represents the final healthy and emphysemic models from three different views. These models were scaled to *in vivo* dimensions then scaled to the proper experimental size as described in the following section.

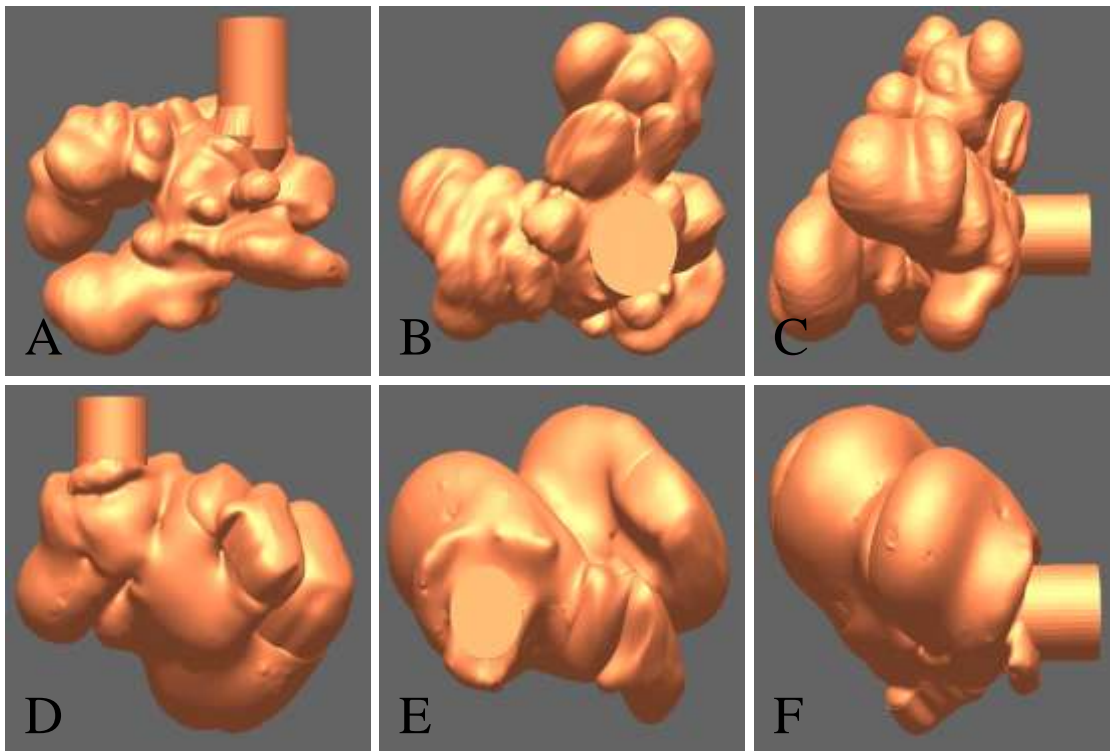


Figure 2.15 - Healthy human final model (A) front, (B) top, and (C) right views (inlet duct measures 113.6 mm prior to scaling). Emphysemic human final model (D) front, (E) top, and (F) right views (inlet duct measures 290.32 mm prior to scaling).

2.5 – Scale Model

2.5.1 – In Vivo Size

The final models were first scaled to *in vivo* dimensions and then scaled to the desired experimental size (see Chapter 3). Figure 2.16 represents the images of the *in vivo* models used for scaling. The yellow lengths represent the known dimensions and the colored lines were then measured and used for the *in vivo* scaling. When the final smoothed model sections were first brought into VP-Sculpt, the dimensions of the model were larger than the desired *in vivo* or experimental size (Figure 2.15). Therefore, each colored length in Figure 2.16 was measured on the over-sized model and compared to the corresponding *in vivo* dimensions.

Table 2.2 and Table 2.3 represent the measured *in vivo* and VP-Sculpt dimensions for the colored lines in Figure 2.16 for the healthy and emphysemic models, respectively.

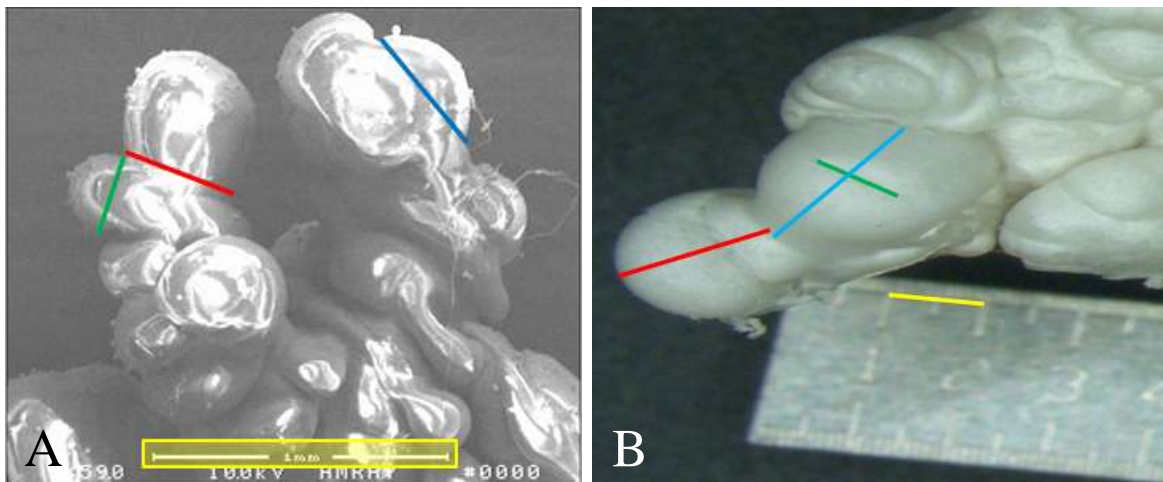


Figure 2.16 - Images of (A) healthy and (B) emphysemic models representing dimensions used for *in vivo* scaling. The yellow bar in (B) represents 1 mm.

Comparing the VP-Sculpt dimensions to the desired *in vivo* size, an *in vivo* scaling factor of $3.61\text{E-}3$ was used for the healthy human model which yielded an *in vivo* volume of 1.3 mm^3 (0.013 mL) and an *in vivo* duct diameter of 0.41 mm. The *in vivo* emphysemic model measured 13.6 mm^3 (0.136 mL) with a duct diameter of 0.90 mm (using a scaling factor of $3.06\text{E-}3$).

Table 2.2 - Measured *in vivo* and VP-Sculpt dimensions for the healthy human model shown in Figure 2.16A.

(An average scale factor of 3.61E-3 was used to scale from VP-Sculpt to *in vivo* size)

	<i>In Vivo</i> Dimension	VP-Sculpt Dimension	Scale Factor
Yellow Scale	1 .0 mm	N/A	N/A
Blue Line	0.43 mm	119.6	3.55E-03
Red Line	0.40 mm	113.7	3.51E-03
Green Line	0.25 mm	65.7	3.76E-03
Duct Diameter	0.41 mm	113.6	3.60E-03

Table 2.3 -Measured *in vivo* and VP-Sculpt dimensions for the emphysema human model shown in Figure 2.16B.

(An average scale factor of 3.06E-3 was used to scale from VP-Sculpt to *in vivo* size)

	<i>In Vivo</i> Dimension	VP-Sculpt Dimension	Scale Factor
Yellow Scale	1 .0 mm	N/A	N/A
Blue Line	2.29 mm	759.67	3.01E-03
Red Line	1.69 mm	552.04	3.06E-03
Green Line	0.98 mm	317.85	3.08E-03
Duct Diameter	0.90 mm	290.32	3.10E-03

2.5.2 – Experimental Size

Experimental parameters for both the healthy and emphysemic models were determined and can be seen in Chapter 3 (refer to Table 3.2 and Table 3.4, respectively). Both experimental models have a duct diameter of 8 mm. Therefore, the healthy model was scaled from *in vivo* size by a factor of 19.4 to yield an experimental model volume of 9013.5 mm³ (scaled from 0.41 mm to 8.0 mm) The emphysemic model, however, required a scaling factor of 8.9 to obtain a duct diameter of 8 mm from *in vivo* size; *in vivo* diameter of 0.9 mm corresponding to and emphysemic experimental model volume of 10488.6 mm³.

2.6 – Create Compliant Models

Physical prototypes of both of the experimental healthy (19.4x *in vivo* size) and emphysemic (8.9x *in vivo* size) models were obtained from Laser Reproductions (Gahanna, OH).

Specifically, each of the models was rapid prototyped using stereolithography techniques at a layer resolution of 0.006” and coated with a semi-bright nickel finish. The finish is necessary to create a surface on the prototype that does not degas into the compliant dipping material. This reduces the creation of bubbles in the compliant model and minimizes the amount of laser light refraction. The healthy human prototype (Figure 2.17) measures 33 mm in length and 41 mm in width while the emphysemic prototype measures 31 mm long and 35 mm wide (Figure 2.18).



Figure 2.17 - Healthy human physical prototype model (A) top, (B) bottom, (C) left, and (D) right views.



Figure 2.18 - Multiple views of the emphysemic human physical prototype model.

Each of the physical prototype models were then dipped into a bath of melted Ultraflex (Douglas and Sturgess Inc.; Richmond, CA) and quickly removed. To ensure uniform thickness throughout the compliant model, the models were



Figure 2.19 - Compliant experimental model of the healthy human lung.

rotated once removed from the bath. After completely cooled (waiting approximately ten minutes), the Ultraflex model was removed from the solid prototype. Figure 2.19 and Figure 2.20 represent images of the healthy human and emphysemic human compliant experimental models, respectively.

When creating future prototypes, it is important to have a thick coating of nickel applied as to reduce the possibility of cracking. Because the SLA material is not rated for the high melting temperatures it is exposed to, allowing the prototype to completely cool in between each dip is essential to maintaining a useable prototype model.



Figure 2.20 - Compliant experimental model of the emphysemic human lung.

Chapter 3: Flow in the Experimental Model

3.1. – Theory

The incompressible, constant viscosity Navier-Stokes equations (White 2006) can be written in non-dimensional form as

$$\left[\frac{\rho f d^2}{\mu} \right] \frac{\partial u^*}{\partial t^*} + \left[\frac{\rho U d}{\mu} \right] u^* \nabla^* u^* = - \left[\frac{P_s d}{\mu U} \right] \nabla^* P^* + \nabla^{*2} u^* \quad (3.1)$$

where $u^* = u / U$, $\nabla^* = \nabla d$, $P^* = P / P_s$, $t^* = t f$, P_s is an arbitrary value chosen to balance the viscous term, ρ is density, u is velocity vector, t is time, P is pressure, μ is dynamic viscosity, f represents the breathing frequency (breaths/sec), d is duct diameter, and U is the time and spatially averaged inlet velocity. The first dimensionless term in Equation 3.1 is related to the Womersley number, the ratio of oscillatory inertial to viscous forces (Loudon and Tordesillas 1998; Womersley 1955), by

$$Wo = \frac{d}{2} \sqrt{\frac{f}{\nu}} \quad (3.2)$$

where ν is the kinematic viscosity of the fluid. The second dimensionless term represents the time averaged Reynolds number ($Re = \frac{\rho U d}{\mu}$), the ratio of inertial forces to viscous forces, and can be written in terms of the experimental conditions as

$$Re = \frac{4 f E V_i}{\pi d \nu} \quad (3.3)$$

where E is percent expansion and V_i is initial model volume. Because the experimental models were scaled up from the *in vivo* size, the experimental parameters were derived as to match both the *in vivo* Re and Wo to the experimental Re and Wo , respectively, for both the healthy and

emphysemic models. Based on fabrication techniques, however, an 8 mm model diameter was desired for both of the models. Therefore, the other parameters affecting the Re and Wo were varied to properly match the *in vivo* conditions

3.2 – Convergence of Small Wo and Re

It is well understood that for small Re and Wo , non-dimensional velocity profiles are independent of Re and Wo , respectively. To test the limits of this assumption, a computational fluid dynamic analysis was run on the expanding three dimensional bulb used for experimental validation seen in Figure 3.1A (Berg et al. 2010). After verifying a grid independent solution, the non-dimensional profiles were obtained numerically for successively small Wo and Re using Fluent (Fluent, Inc.) at two locations in the model; in the center of the rigid duct at $z = 0.55$ mm and in the expanding bulb at $z = 0.375$ mm (Figure 3.1).

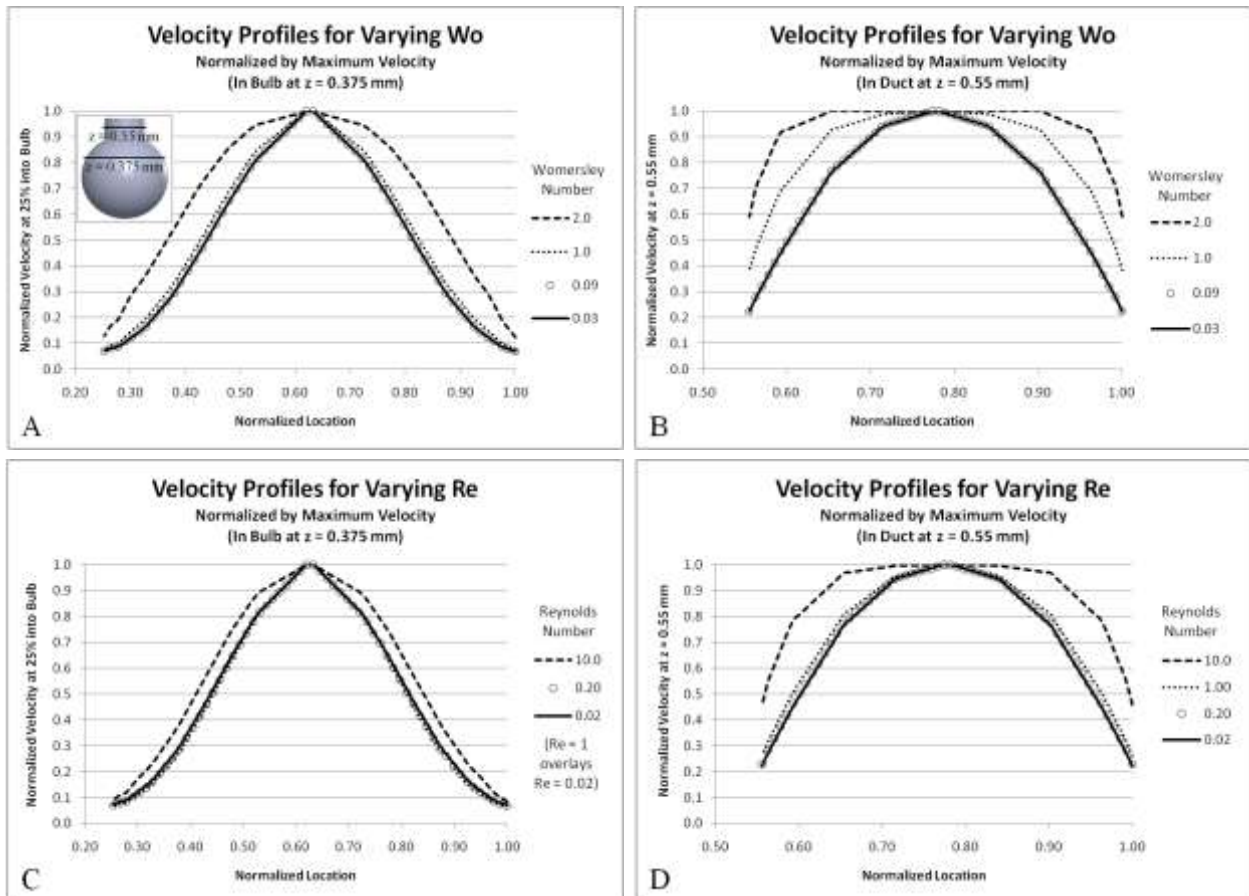


Figure 3.1 - Velocity profiles for varying Wo occurring (A) in the expanding bulb at $z = 0.375$ mm and (B) in the rigid duct at $z = 0.55$ mm. Velocity profiles for varying Re occurring (C) in the expanding bulb and (D) in the rigid duct.

Figure 3.2 shows that non-dimensional velocity profiles converge at about $Wo = 0.2$ and $Re = 0.7$, which are both larger than the *in vivo* and experimental conditions in the present study. These results were used to insure that *in vivo* conditions were well represented experimentally, as explained in the following sections.

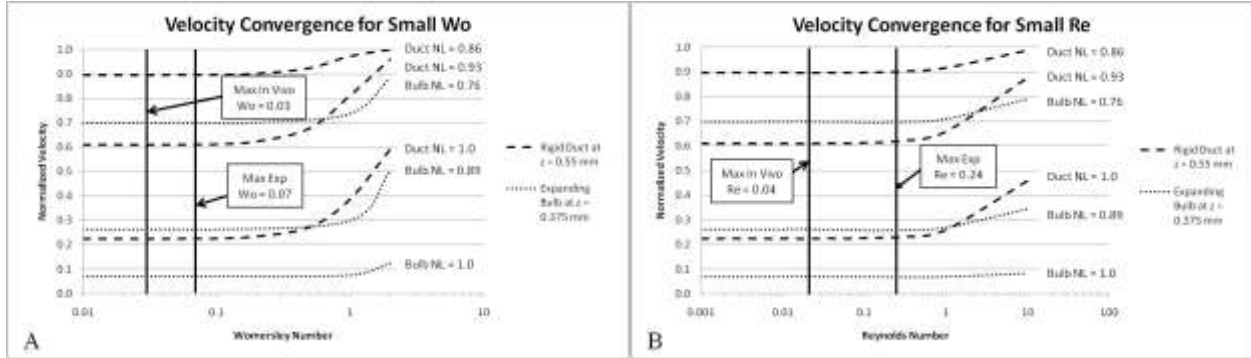


Figure 3.2 - Convergence plots for (A) Womersley and (B) Reynolds numbers showing that velocity profiles converge prior to reaching the maximum experimental $Wo = 0.07$ and before the maximum experimental $Re = 0.24$. NL refers to the non-dimensional locations in Figure 3.1.

3.3 – Healthy Human Parameters

Table 3.1 represents the model and material properties for the healthy human model used for experimental analysis. These values were concluded from the scaling analysis described in Chapter 2. The experimental healthy model was scaled from the *in vivo* size by a factor of 19.4 to obtain a duct diameter of 8 mm.

Table 3.1 - Model and material properties for the healthy human model.

Symbol	Property	<i>In Vivo</i> (Air at 20°C)	Experimental (Glycerin at 20°C)
d	Acinus Inner Duct Diameter (mm)	0.41	8.00
V_i	Mean Acinus Volume (mm ³)	1.25	9013.46
ν	Kinematic Viscosity (mm ² /sec)	17.10	909.80

In vivo breathing conditions for a healthy human breathing under normal conditions were determined based on information cited by Robinson et al. (2007). Using an average functional residual capacity (FRC) of 3050 L and an average tidal volume (TV) of 483 mL, the calculated *in vivo* expansion (TV / FRC) is 16% with an average breathing frequency of 15.71 breaths/min. Using the properties in Table 3.1, the *in vivo* Re is 0.009 with a Wo of 0.03. To simulate heavy breathing for a healthy human, however, Re and Wo were calculated using 60% expansion and found to be 0.04 and 0.03, respectively (Table 3.2). Because both Re and Wo are small and less than the converged values of 0.7 and 0.2, respectively (section 3.2), this indicates that the flow fields in the alveoli region are unchanged for normal versus heaving breathing conditions in a healthy human.

In order to match the experimental parameters with the *in vivo* conditions used in this work, the Wo was first matched because it is only a function of the breathing frequency; assuming the diameter is fixed at 8 mm (Equation 3.2). For an *in vivo* Wo of 0.03, an experimental breathing frequency of 2.23 breaths/min was required (a period of 26.9 seconds). Using this required frequency, an experimental expansion of 16% would then match the *in vivo* Re (Equation 3.3). The calculated *in vivo* and experimental flow parameters are shown in Table 3.2.

Table 3.2 - Healthy human *in vivo* and experimental fluid parameters required to match Re and Wo.

The grey values represent the chosen parameters used in this work.

		Breathing Frequency (breaths/min)	Period (sec)	Womersley	Expansion (%)	Reynolds
<i>In Vivo</i> Air at 20° C	Normal Breathing	15.7	3.8	0.03	16	0.009
	Heavy Breathing	15.7	3.8	0.03	60	0.035
Experimental Glycerin at 20° C	Matched Normal	2.2	26.9	0.03	16	0.009
	Matched Heavy	2.2	26.9	0.03	60	0.035
	Used in This Work	15.0	4.0	0.07	35	0.138

It is seen that the experimental period required to precisely match *in vivo* conditions is extremely large (26.9 seconds for a single breath to be completed). This is not an ideal condition because the particle displacements between sequential images would be difficult to detect. Also, because the motion of the pump would have to be extremely slow to produce a 26.9 second breathing period, we did not want to introduce residual particle motion into the system between sequential frames. Therefore, a more realistic breathing period for experiments is 4 seconds.

If a 4 second period was used rather than 26.9 seconds, the corresponding Wo is calculated to be 0.07 with a Re of 0.14 (using an expansion of 35%), which is still small and less than the converged values of 0.2 and 0.7, respectively. It is clear from the velocity profile plots (Figure 3.1) that the *in vivo* conditions for both Re and Wo would be met for all proposed experimental healthy cases because the non-dimensional velocity profiles are identical for Womersley numbers of 0.03 and 0.07, and for Reynolds numbers of 0.02 and 0.20 (within the range of proposed experimental conditions). Therefore, the presence of heavy breathing conditions has little effect on the flow field.

The grey values in Table 3.2 represent the final experimental Re and Wo using a breathing period of 4 seconds as compared to the *in vivo* Re and Wo . A 35% expansion was desired for the healthy model because the corresponding average input flow rate of 1.9 mL/sec coupled with the chosen pulse frequency of the laser (12.5 Hz) yields the appropriate particle displacement for collected image pairs.

3.3 – Emphysemic Human Parameters

Using the desired experimental duct diameter of 8 mm for the emphysemic model, a scaling factor of 8.9 was applied to the *in vivo* model (see Chapter 2). The model and material properties for the *in vivo* and experimental emphysemic models are shown in Table 3.3

In order to apply the same flow conditions to both the emphysemic and healthy models, the Re and Wo between each model were matched ($Re = 0.14$ and $Wo = 0.07$). In order to achieve these values, an experimental expansion of 30% was required for the emphysemic model with a

breathing period of 4 seconds (the difference in experimental percent expansion is due to the 11x difference in initial volumes between the healthy and emphysemic models).

Table 3.3 - Model and material properties for the emphysemic human model.

Symbol	Property	<i>In Vivo</i> (Air at 20°C)	Experimental (Glycerin at 20°C)
d	Acinus Inner Duct Diameter (mm)	0.90	8.00
V_i	Mean Acinus Volume (mm ³)	14.39	10488.60
ν	Kinematic Viscosity (mm ² /sec)	17.10	909.80

Table 3.4 - Emphysemic human *in vivo* and experimental fluid parameters required to match Re and Wo.

The grey values represent the chosen parameters used in this work.

		Breathing Frequency (breaths/min)	Period (sec)	Womersley	Expansion (%)	Reynolds
<i>In Vivo</i> Air at 20° C	Normal Breathing	16.0	3.7	0.03	11	0.04
Experimental Glycerin at 20° C	Matched Normal	2.3	26.4	0.03	50	0.04
	Used in This Work	15.0	4.0	0.07	30	0.14

The chosen experimental parameters for the emphysemic model are shown in grey in Table 3.4. Similar to the healthy model, an inlet flow rate of 1.94 mL/sec was applied to the emphysemic model. It is seen that the chosen experimental parameters ($Re = 0.14$ and $Wo = 0.07$) are below the converged values of $Re = 0.7$ and $Wo = 0.2$ (see section 3.2). Therefore, the presence of emphysemic conditions plays little to no role in alveolar flow. This allowed us to focus solely on the differences in flow fields that exist between the healthy and emphysemic models due to geometry effects rather than input Re or Wo (for all values of $Re \leq 0.7$ and $Wo \leq 0.2$).

Chapter 4: Experimental Methods

4.1 – StereoPIV Theory

PIV is an optical measurement technique used to non-invasively obtain instantaneous velocity fields in fluid flows. The fluid is seeded with small reflective tracer particles whose motion is tracked between images. Stereoscopic PIV is based on the same fundamental principles as human eye-sight. As with 2D measurements, stereoPIV measures displacements rather than actual velocities (with the cameras playing the roles of the eyes). The most accurate determination of the out-of-plane displacement is accomplished when there is 90° between the two cameras. The first camera would be able to capture the x and y components of velocity, while the second camera would capture the y and z components. In the cases of restricted optical access, however, smaller angles can be used at the cost of a somewhat reduced accuracy. For each vector, three true displacements (dX , dY , and dZ) are extracted from a pair of 2-dimensional displacements (dx , dy) as seen from the left and right cameras, respectively. Figure 4.1 illustrates the fundamentals of the stereoPIV process. The blue arrow, for example, would represent a single particle displacement through the light sheet. The 2D particle displacement seen from left camera is shown as the red arrow, while the 2D particle displacement seen from the right camera is represented as the black arrow.

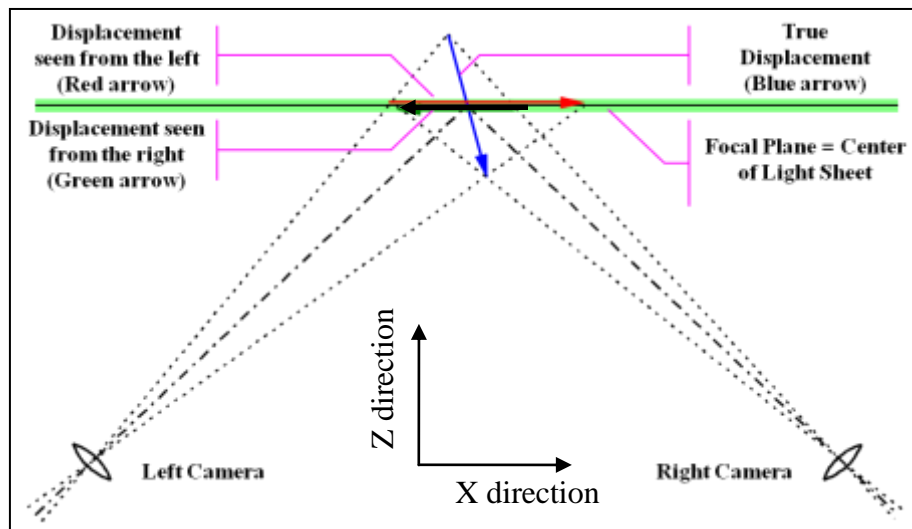


Figure 4.1 - Fundamentals of stereoPIV (Dynamics 2010). The x and z directions are depicted as right and up, respectively, while the y direction is out of the plane.

Due to perspective distortion occurring from the angle of the cameras with respect to the light sheet, each camera covers a trapezoidal region of the light sheet. Even with careful alignment of the two cameras, their respective fields of view only partly overlap each other. Within the region of overlap, interrogation points are chosen in a rectangular grid to match the spatial resolution of the cameras (Figure 4.2).

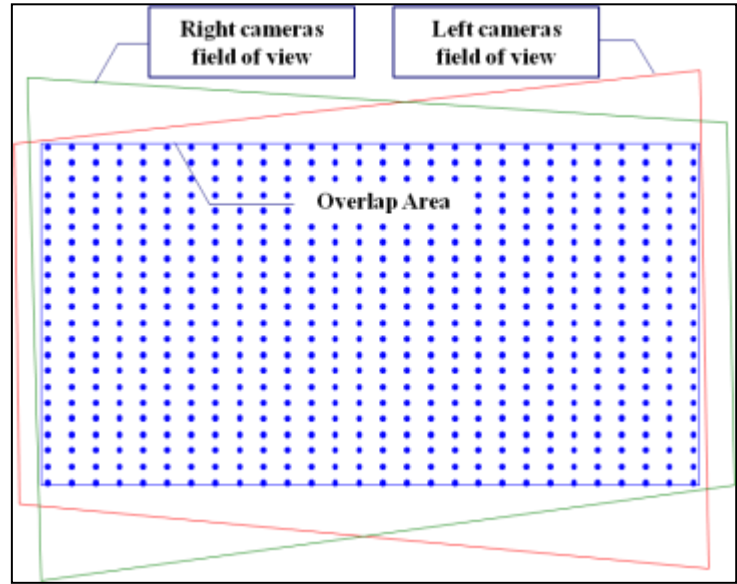


Figure 4.2 - Overlap area with interrogation region resulting from each camera's field of view (Dynamics 2010).

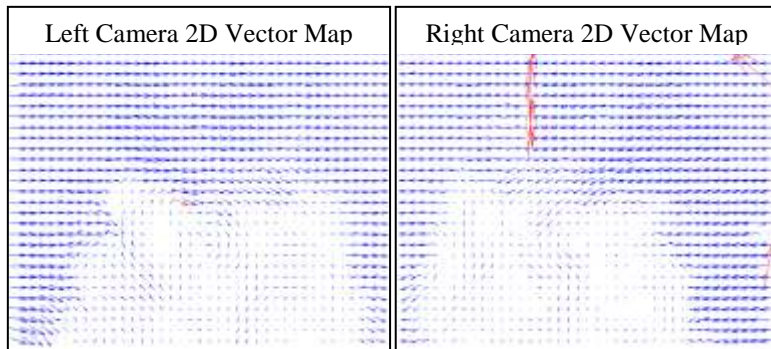


Figure 4.3 - Processed 2D vector maps from each camera (Dynamics 2010).

from the left and right cameras, respectively (Figure 4.3).

The actual stereoscopic measurements begin with conventional 2D PIV processing of simultaneous recordings from left and right cameras, respectively. This produces two 2-dimensional vector maps representing the instantaneous flow field as seen

The acquired images are grey scale images with variations of light intensities representing the presence of fluorescent particles. Each image set (two sequential image pairs) is separated by a known ΔT , the separation between laser pulses, and broken into small interrogation regions for cross correlation. Figure 4.4 represents a typical interrogation region used for image processing (representing 32x32 pixel squares). The group of particles that exists in each interrogation region represents a fairly unique 'fingerprint' that is tracked between both frames in the image set. Once a unique pattern is found for a particular region, the mask is scanned through the defined search area in the second frame and a correlation value is calculated at each

position. The value of the correlation function will be maximized when the ‘fingerprint’ is identified in the mask in the second frame. Ideally, a single, distinct, round peak will exist in the correlation map. Once identified, the x and y displacements of the particles are determined by the offset of the interrogation regions. Finally, since the ΔT between laser pulses is known, the group velocity for a particular region is measured as the displacement divided by the ΔT , and a single vector is assigned for each interrogation region (Figure 4.5). The process is completed for every interrogation region until all vectors are calculated (either real or interpolated). Figure 4.6 illustrates a different perspective on the calculation of a velocity vector for a particular interrogation region.

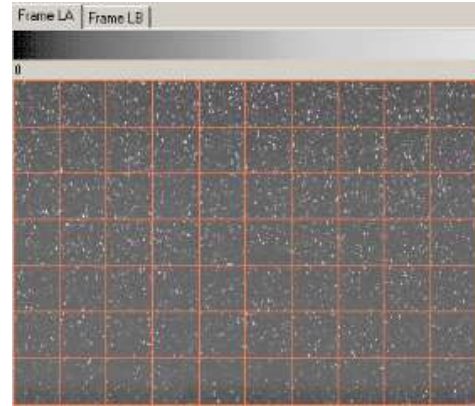


Figure 4.4 - Typical interrogation region used for image processing.

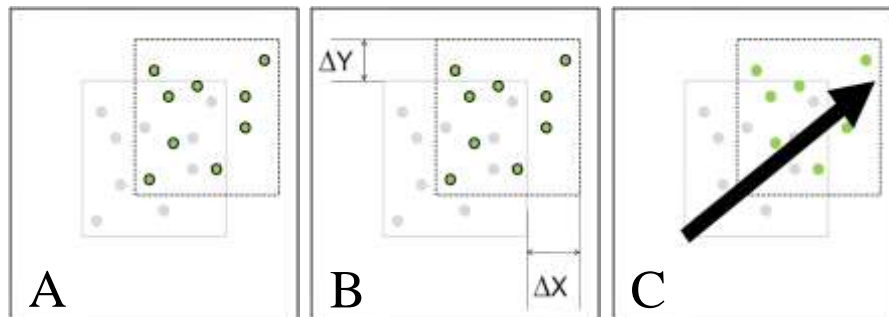


Figure 4.5 - (A) Identify particle mask, (B) determine position change, and (C) calculate vector based on known displacement / known ΔT (TSI 2009).

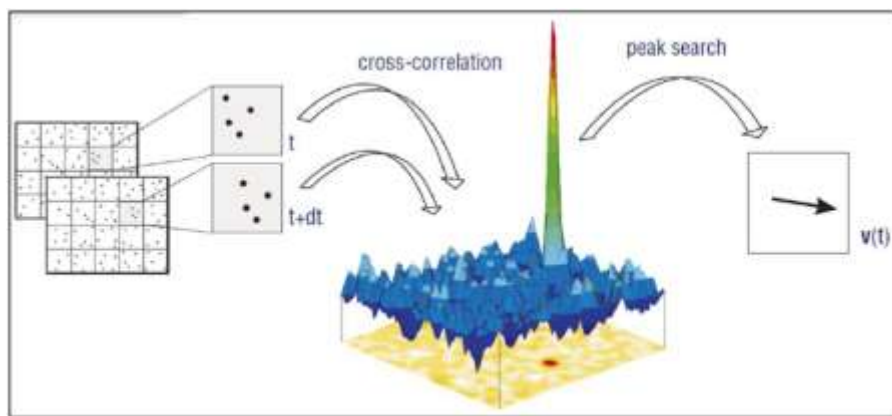


Figure 4.6 - Image processing theory representing a single correlation peak (LaVision 2009).

Using the known parameters from the perspective calibration (distance from the object to the image, lens focal length, and camera angle), the points in the interrogation grid (overlap area occurring in Figure 4.2) are mapped from the light sheet plane onto the left and right image planes (camera sensor) respectively. The 2D vector maps are re-sampled in the new interrogation regions to estimate 2D vectors at each point based on the nearest neighbours. The resulting 3D vector map is then calculated and depicted in Figure 4.7.

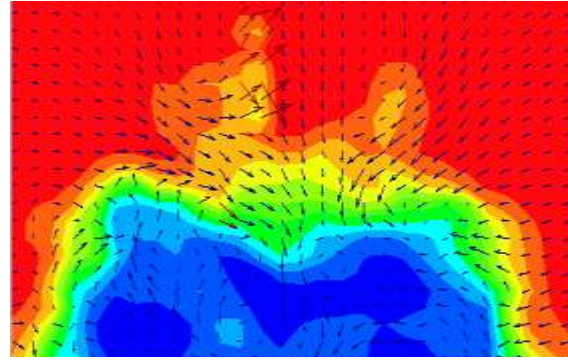


Figure 4.7 - Resulting 3D vector map (Dynamics 2010).

4.2 – Experimental StereoPIV Setup

4.2.1 – Cameras and Optics

The experimental setup developed in our lab for stereoPIV analysis is shown in Figure 4.8.

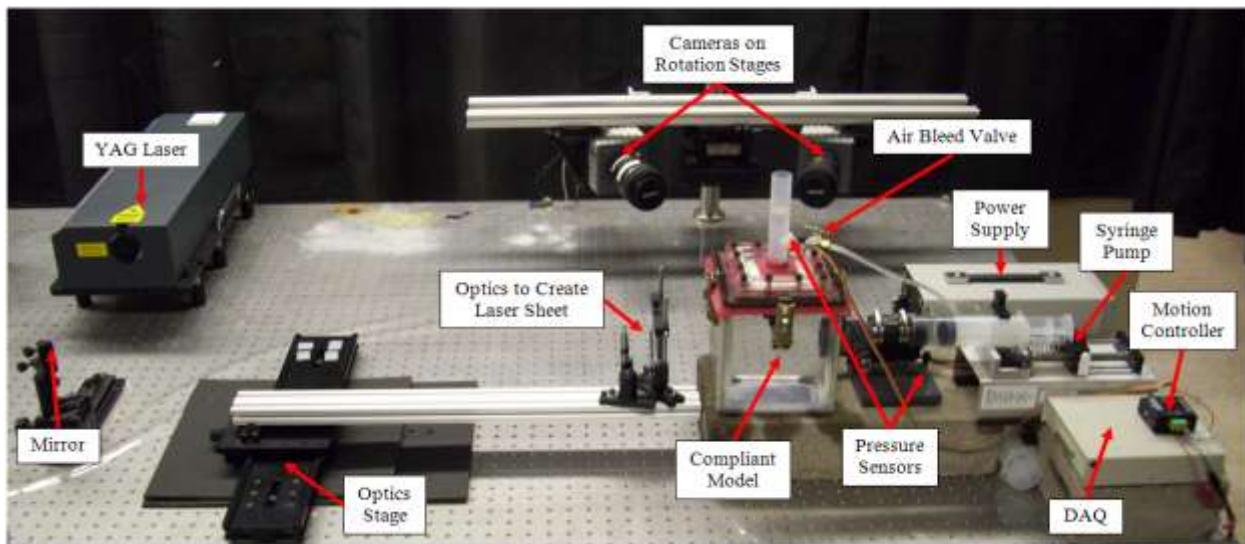


Figure 4.8 - Experimental stereoPIV setup developed in our lab.

Images were captured using two IDT Motion Pro X-3 Plus high-speed digital cameras, each equipped with a Tamron macro lens with a focal length of 90 mm, f-number of 2.8, and an image macro magnification ratio of 1:1. Ideally, Scheimpflug mounts are used to focus on planar fields

at oblique viewing angles. Because they were not used in this experiment, the camera angles were minimized to allow the entire image to be in focus across the laser sheet. Therefore, each camera was angled 15° from the perpendicular to the light sheet and was 7" from the center stand (30° between cameras as opposed to the ideal angle of 90° as described above). The distance from the camera lens to the experimental model was chosen as to allow the entire experimental model to fit into the field of view of each camera, resulting in a spatial resolution of $64.23 \mu\text{m}$ per pixel occurring at the center of the experimental setup and varying as the light sheet location changes. The fluid was illuminated with a New Wave Research Solo II pulsed 532 nm laser and $8 \mu\text{m}$ red fluorescent polymer microspheres (Duke Scientific Corp.; Palo Alto, CA) were used as tracer particles in 99% glycerin carrier fluid (emitting at 612 nm). A mirror, positioned on a rotation stage, was used to direct the beam from the laser to the optics. A planar laser sheet was created by passing the collimated laser beam through a cylindrical lens, focal length of 25.4mm, and a spherical lens of focal length 150 mm. The cameras were focused on regions of the experimental models in which the laser sheets waist (focal point of the beam) occurred, measuring approximately 1 mm thick and occurring in the center of the model. The cameras and laser were synchronized using a TSI Laser Pulse Synchronizer and triggered with the start of each experiment.

4.2.2 – Testing Fixture and Components

The experimental testing rig (shown in Figure 4.8) was developed to contain the experimental models and to simulate the input breathing parameters to achieve the proper *in vivo* flow conditions. Each compliant model was housed in a glycerin (refractive index of $1.47 \pm 2.0\text{E-}3$) chamber and filled with a glycerin / particle mix of approximately 0.007 grams of particles per 150 mL of glycerin to achieve the appropriate mixture required to minimize PIV processing error (Soria 2000). A computer controlled syringe pump drew a negative pressure on the chamber fluid, expanding the model and drawing glycerin from the inlet tube into the compliant model. Total model volume changes were verified with pressure sensors placed at the model inlet (MPXV5010GP, Freescale Semiconductor, Inc.) and at the base of the chamber (PX2300-10DI, Omega Engineering, Inc.). The syringe pump (NE-500, New Era Pump Systems, Inc.) was fitted with a stepper motor and controlled by a motion controller (MBC25081TB, Anaheim

Automation), programmed using LabVIEW and a DAQ device (PCI-6025E DAQ, National Instruments Corp.).

4.2.3 – LabVIEW Code

A LabVIEW code was generated to accurately control the motion of the experimental models based on the *in vivo* flow conditions. Once the experimental parameters were chosen (Chapter 3), the Re and Wo were matched by varying the input controls (initial model volume, percent expansion, and breathing period). Figure 4.9 represents the LabVIEW block diagram used to expand and contract the experimental models.

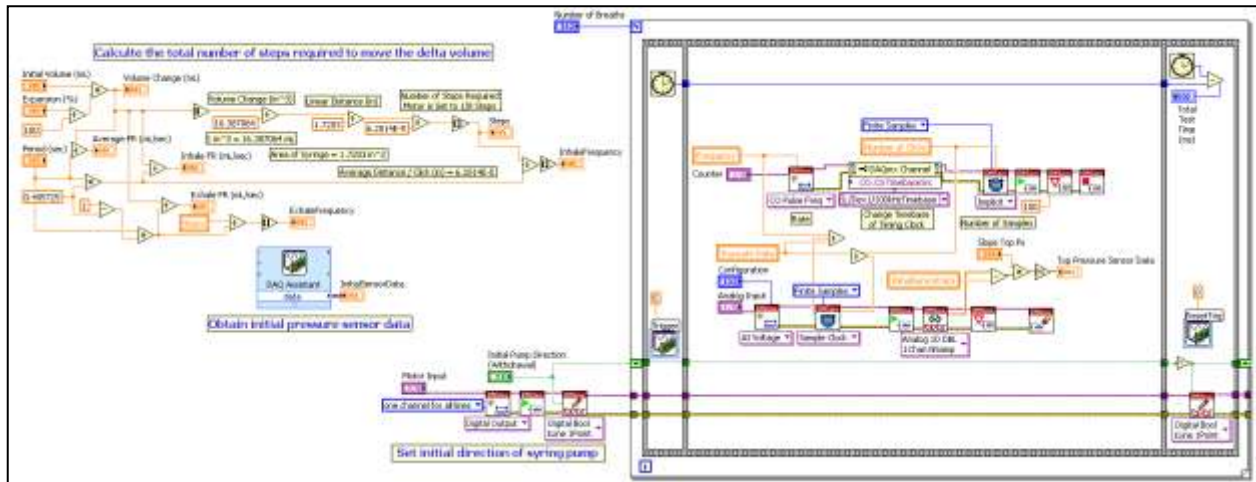


Figure 4.9 - LabVIEW block diagram used to expand and contract the experimental models.

Based on the initial volume and percent expansion of each model, the total volume change was calculated and converted to a linear distance based on the area of the syringe used (140 mL syringe with a cross sectional area of 1.7203 in^2). The average linear distance moved per step of the motor was $6.2\text{E-}5 \text{ in}$. Therefore, the total number of steps and step frequency (number of steps / inhalation time) was calculated and applied to the stepper motor. Each model required a flow rate of 1.94 mL/sec for a 4 second period (see Chapter 3) corresponding to a 3.15 mL volume change over the inhalation time (1.62 seconds). Therefore, for each model, a total of 1,802 clicks were required at a frequency of 1,112 clicks / second. At the start of the motion of the pump, a 5V trigger was sent to the pulse synchronizer to begin image capture. Finally, data

from the pressure sensor located at the inlet to the model was sampled and displayed to verify the correct volume change during each experiment.

4.3 – Image Capture

TSI’s Insight 3G (TSI Inc., Shoreview, MN, USA) was used to capture images for each experiment. Figure 4.10

represents the capture settings used for each of the experimental models. A single pulse / frame for each camera was used with a frequency of 12.5 Hz (deltaT of 0.08 seconds between sequential laser pulses and

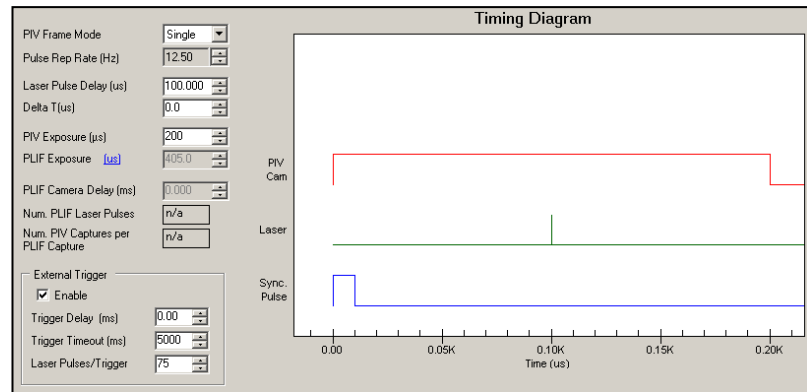


Figure 4.10 - Capture settings for stereoPIV experiments.

images). Because a period of 4 seconds was chosen for each model, a total of 50 images were required for each data set, but a total of 75 images were actually collected to account for any residual fluid motion. Because two cameras were used, 75 images were collected for the left camera and 75 collected for the right (a total of 150). For each laser sheet location, a total of three data sets were collected to illustrate the repeatability of the experimental results (refer to section 5.2.5 for variability analysis).

4.4 – Healthy Human Analysis Settings

A total of fourteen laser locations were selected for the healthy human model. The laser sheet was initially positioned just inside the model then moved in 3.2 mm (1/8”) intervals, collecting data at every new sheet location. At every position, the distance from the object to the image was measured (distance from the light sheet to the CCD array in the camera). This information was necessary to create an accurate perspective calibration file needed for image processing. In order to achieve the correct *in vivo* flow conditions (refer to Chapter 3), the input parameters shown in Figure 4.11 were applied at each laser plane location (breathing period of 4 seconds and model expansion of 35%).

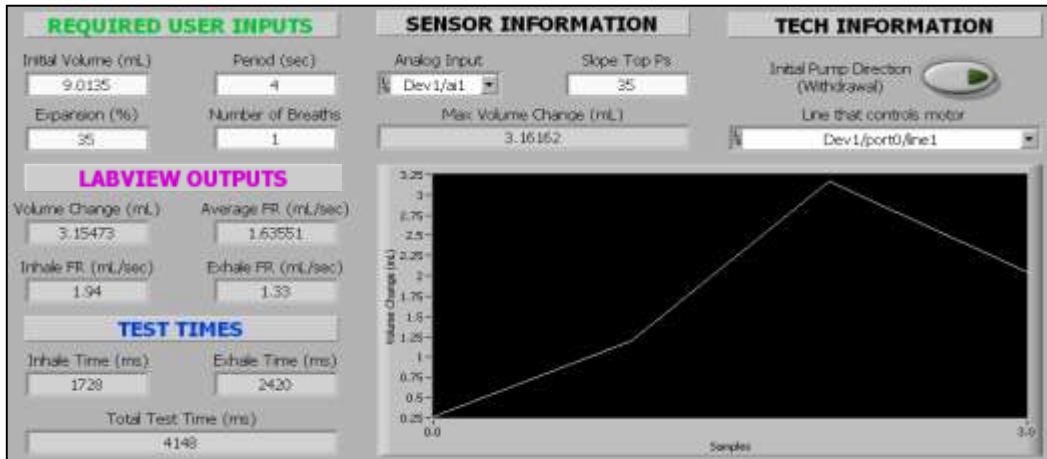


Figure 4.11 - LabVIEW output for a healthy human experiment displaying the input parameters required to match in vivo conditions (4 second period and 35% expansion resulting in an inhale flow rate of 1.94 mL/sec).

Table 4.1 represents the measurements collected for each laser sheet location where data was analyzed, including the two regions where recirculation would be most likely to occur.

Table 4.1 - Measurements obtained for each laser sheet location analyzed (RR = recirculation region).

	Mirror Location (mm)	Distance Object to Image (mm)
2ndLocation	43.7	669.9
4thLocation	50.0	663.6
6thLocation (1st RR)	56.4	657.2
8thLocation (2nd RR)	62.7	650.9
10thLocation	69.1	644.5
12thLocation	75.4	638.2

4.4.1 – Creating Calibration Files

Insight 3G was used to process the raw images collected from each laser sheet location. First, a perspective calibration file was created for each location. This allows the program to account for the magnification changes that occur across the field of view of the camera with respect to the center of the light sheet. Figure 4.12 represents the left and right calibration files for the second location in the healthy human model.

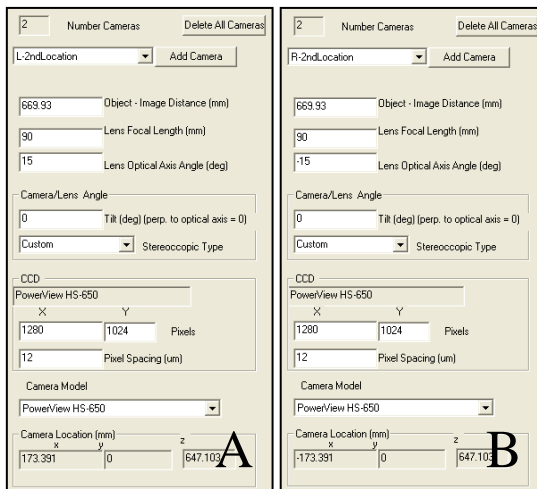


Figure 4.12 - (A) Left and (B) right perspective calibration files for the 2nd location in the healthy human model.

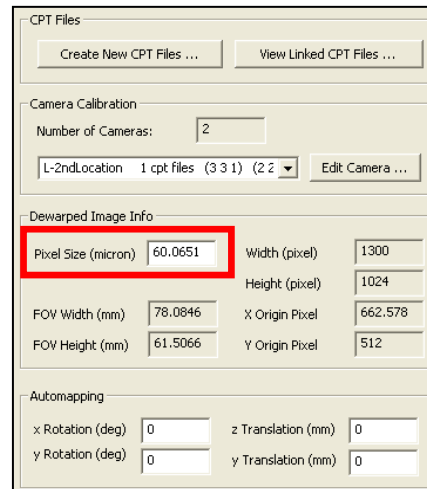


Figure 4.13 - Pixel to length conversion for the 2nd location created from the information in Figure 4.12.

4.4.2 – Stereo AutoMapping

Prior to processing the raw images, it was important to translate the images to make sure they were on top of each other.

Figure 4.14 represents an image pair prior to translating with a blue grid overlaid representing 50 pixels per square. It can be seen that Figure 4.14B needs to be translated approximately 100 pixels to the left and 10 pixels down to align with Figure 4.14A. This translation was

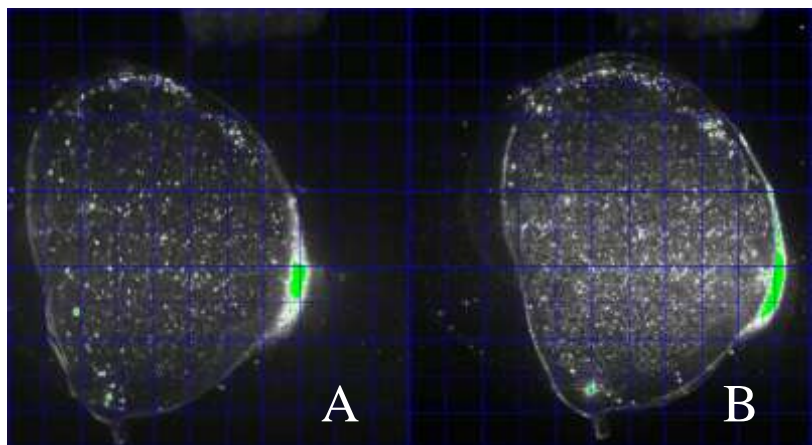


Figure 4.14 - Images prior to translating (grid represents 50 pixels).

completed using ImageJ and was necessary for all image sets analyzed. A stereo AutoMapping procedure was then completed on all selected laser sheet locations to optimize the perspective calibration by correcting the misalignment errors existing in the measurements between the light sheet location and the CCD array in the camera. This procedure was completed for each location to update the manual calibration files. A series of AutoMapping iterations was performed (as defined in the Insight 3G manual) until the parameters were considered converged and the final pixel to length conversion factor calculated. Figure 4.15 represents the results of the stereo AutoMapping procedure for the 2nd laser sheet location in the healthy model. It is seen that after the 4th iteration, the parameters have converged with the number of valid vectors maximized.

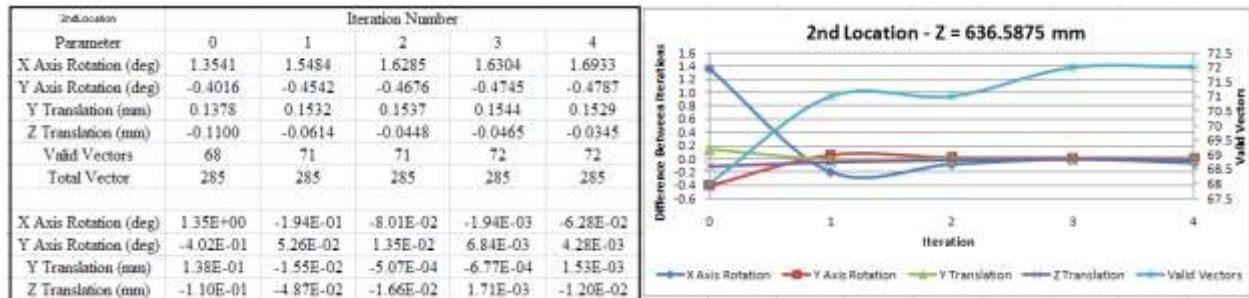


Figure 4.15 - Stereo AutoMapping results for the 2nd location in the healthy model.

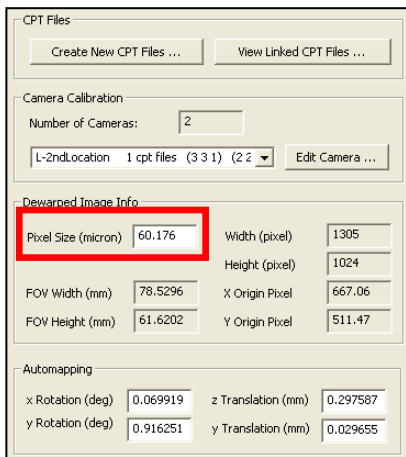


Figure 4.16 - Perspective calibration for the 2nd location after stereo AutoMapping.

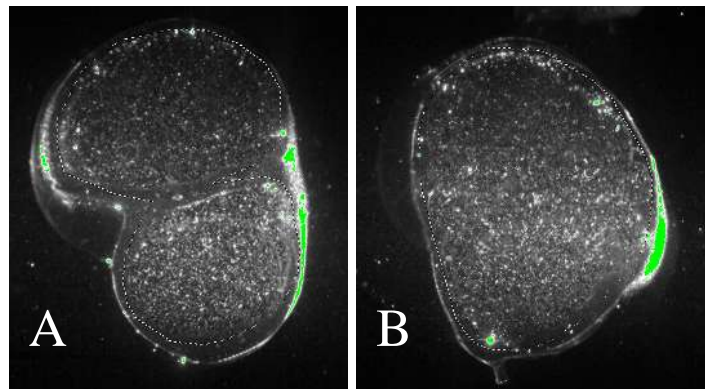


Figure 4.17 - Processing mask for the (A) 4th and (B) 6th locations in the healthy model.

Based on the stereo AutoMapping results, the perspective calibration files were updated. Figure 4.16 represents the updated calibration file that was used for processing the 2nd location images. It can be seen (when compared to Figure 4.13) that the linear conversion factor increased from

60.07 μm / pixel to 60.18 μm / pixel in (shown in the red boxes from Figure 4.13 to Figure 4.16) and is used when converting the particle displacements from pixels to physical length. This small change in conversion factors is an indication that the measurements obtained from the setup used to create the initial perspective calibration were correct. Each location also requires a unique processing mask. This determines which regions of the raw images to analyze. Vectors outside of the physical model are of no interest, and, to reduce processing time, are not included in the processing. Therefore, at each location, an outer boundary is drawn on the raw images to represent which regions to process. As an example, Figure 4.17 illustrates the processing mask applied at two different locations (shown as the dotted lines).

4.4.3 – StereoPIV Processing Parameters

With the AutoMapping completed with the final conversion factor calculated (Figure 4.16) and processing mask applied, each of the laser locations were then processed to extract particle displacements and velocity vectors. A correlation based PIV processor algorithm (Insight 3G default) was used to analyze the image pairs. A recursive Nyquist grid engine was chosen to increase the accuracy and spatial resolution of the results by processing the images in two passes with 50% grid overlapping. The correlations were calculated using Fast Fourier Transforms (FFT)

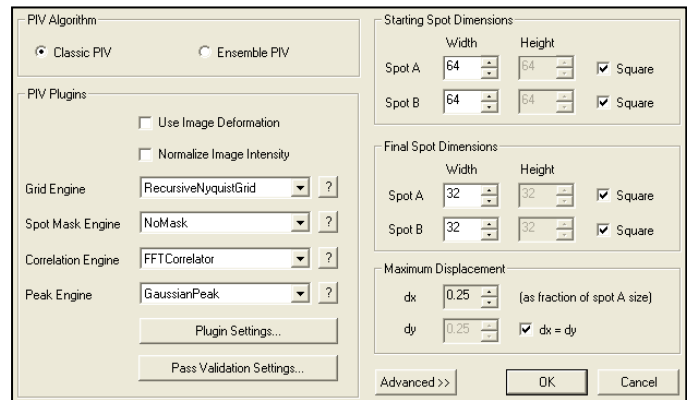


Figure 4.18 - StereoPIV processor used for image processing.



Figure 4.19 - (A) Local vector validation parameters and (B) vector conditions parameters for processing.

while the correlation peaks were located by fitting a Gaussian curve to the highest pixel and its four nearest neighbors. Figure 4.18 shows the stereoPIV processor setup used for the healthy human model, while Figure 4.19 represents the post processing parameters used for analysis. With all of the necessary parameters defined, each image set was analyzed using a known deltaT of 0.08

seconds (pulse frequency of 12.5 Hz). Results for the healthy model are found in Chapter 6.

4.5 – Emphysemic Human Analysis Settings

A total of twelve data laser sheet locations were selected for the emphysemic human model. The laser sheet was initially positioned just inside the model then moved in 3.2 mm (1/8”) intervals, collecting data at every new sheet location. Similar to the healthy model, the distance from the object to the image was measured at every laser location and used to create a unique perspective calibration file for every distance (distance from the light sheet to the CCD array in the camera).

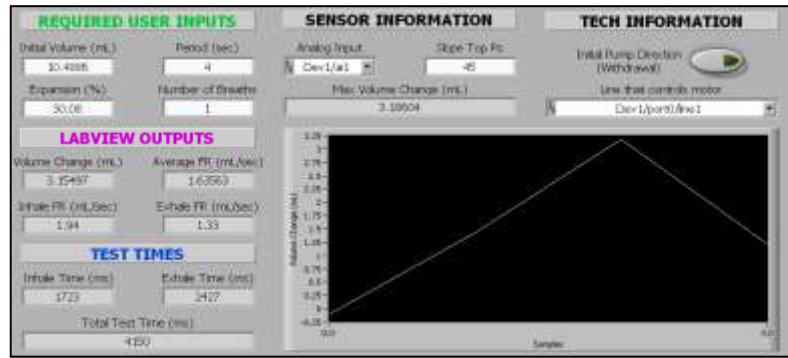


Figure 4.20 - LabVIEW output for an emphysemic human experiment displaying the input parameters required to match *in vivo* conditions (4 second period and 30.08% expansion resulting in an inhale flow rate of 1.94 mL/sec).

Figure 4.20 illustrates the flow conditions applied to the emphysemic model at every sheet location to match the *in vivo* flow conditions (4 second breathing period and expansion of 30%).

Table 4.2 shows the measurements obtained for each of the laser sheet locations analyzed. The process described in section 4.4.3 for processing of the healthy images was applied to the emphysemic model while the emphysemic model results are found in Chapter 6.

Table 4.2 - Measurements obtained for each laser sheet location analyzed for the emphysemic model.

	Mirror Location (mm)	Distance Object to Image (mm)
2ndLocation	73.8	639.8
4thLocation	67.5	646.1
6thLocation	61.1	652.5
8thLocation	54.8	658.8
10thLocation	48.4	665.2

Chapter 5: Experimental Validation

5.1 – CFD Expanding Boiling Flask Model

In order to validate the experimental stereoPIV setup, a simplified geometry was first tested experimentally and compared with computational results.

5.1.1 – Model Creation

A boiling flask model was created in SolidWorks using the outer dimensions of a 50 mL glass boiling flask (Figure 5.1). The two vertical blue lines in the model represent the different planes that were analyzed. The first plane (plane that the laser sheet goes through in the model) was located in the center of the model, while the second plane was 11 mm from the center.

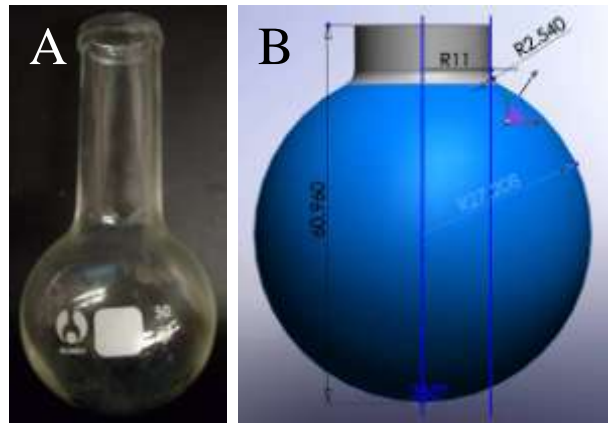


Figure 5.1 - (A) Glass boiling flask and (B) SolidWorks model used for CFD simulations.

5.1.2 – Fluent Simulation

5.1.2.1 – Input Parameters

A constant flow rate of 3.20 mL/sec was applied to the model for 2.5 seconds. This represents an 8 mL increase in volume corresponding to 9.5% expansion of the model. These conditions were chosen to allow for proper expansion of the bulb model mesh. Because portions of the mesh were stationary throughout the simulation while other regions were continually expanding and changing positions, the risk of overlapping of the mesh existed, which would cause failure of the simulation. For this boiling flask mesh, a percent expansion of $\leq 16.5\%$ was desired to prevent overlapping or negative volume detection in the model. Therefore, an arbitrary expansion of 9.5% was chosen.

A 3D, unsteady, pressure based solver was used in Fluent to simulate the boiling flask model. Glycerin was defined as the fluid material with a density, ρ , of 1264.02 kg/m³ and a dynamic

viscosity, μ , of 1.15 kg/m-s. Three dynamic zones were defined for the bulb: the inlet (stationary top surface of the duct where the inlet flow rate was applied), a moving zone (all nodes making up the circular geometry of the bulb where expansion of the nodes occurs (shown as the blue portion of the model in Figure 5.1B)), and a deforming zone (portion of the model that connects the stationary inlet to the moving boundary (shown in grey in Figure 5.1B)). The motion of the moving boundary zone was defined in the user-defined function (UDF). The model was re-meshed in-between each iteration to minimize skewness of the elements and to allow the mesh to update to the moving contours of the model. A second order upwind scheme was used to interpolate the momentum term while a second order scheme was selected for the pressure terms. A PISO algorithm was used for the pressure correction. Under-relaxation factors of 0.2, 0.8, 0.8, and 0.5 were chosen for pressure, density, body forces, and momentum, respectively, to aid in the convergence of the solution. In order to check convergence of the fluids equations, residuals (continuity, x-velocity, y-velocity, and z-velocity) were monitored with a convergence criterion of 1E-4. Finally, a time step of 0.01 seconds was applied for 250 steps with a maximum of 1000 iterations per time step and the solution was saved at each flow time occurring throughout the simulation (every 0.01 seconds).

5.1.2.2 – Fluent UDF

In order to expand and contract the boiling flask model in Fluent, similar to the motion existing in the experimental setup, a UDF (user-defined function) was modified from a previous version presented by our group (Harding and Robinson 2010). The solution was initialized which reads the input flow rate array file (constant flow rate of 3.20 mL/sec) and calculates the initial volume of the model. The grid motion routine starts, which updates the volume of the mesh by iterating until the correct expanded volume (also known as the target volume) is met. This procedure calculates the target volume of the model based on the input flow rate and the current time step. The model is then uniformly deformed in small increments until the percent difference between the current volume and the target volume is less than 1E-5. This is done by moving all of the nodes in the moving boundary zone adjacent to the surface the same calculated amount. Specifically, the nodes are displaced by $((\text{target volume} - \text{current volume}) * 1\text{E}-6)$ m every iteration within each time step until the model has expanded to the calculated target volume for

the given time step. Once the grid has been updated to the calculated target volume for a particular time step, the Navier-Stokes and continuity equations are solved using an iterative process. A maximum of 1000 iterations occur until the solution is converged for a given time step; occurring when the residuals reach $1E-4$ (continuity, x-velocity, y-velocity, and z-velocity). For the physical times analyzed, all velocity profiles were converged in less than the 1000 allowable iterations. An end routine is then completed to append all important data to text files. This includes the target and current volumes, residuals, and the volume and mass flow rate data for the given time step. The flow time is then increased by the time step (0.01 was used for this analysis) and the grid motion routine is restarted followed by the fluid solutions. The above iterative process of grid motion and fluid solutions is then continued until all of the specified time steps have been completed. Figure 5.2 represents a flowchart of the UDF that was written to expand and contract the boiling flask model.

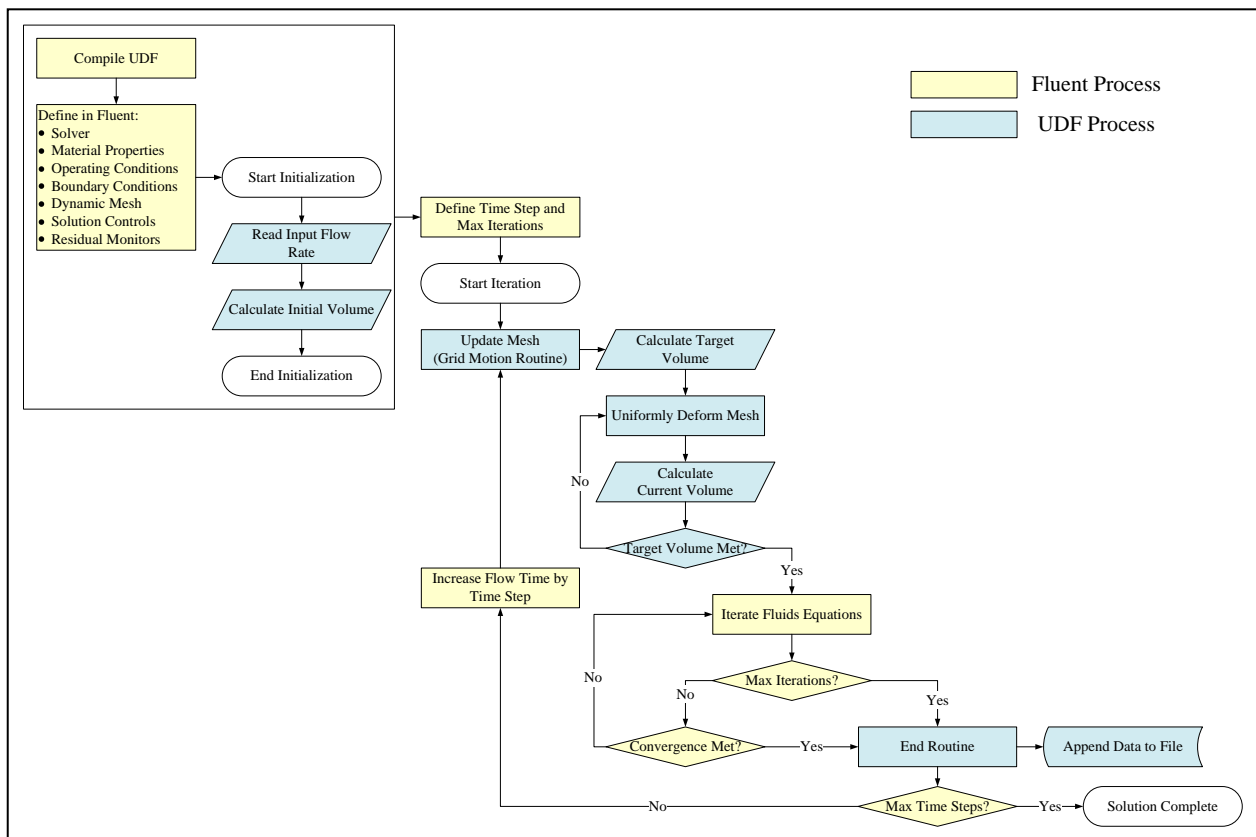


Figure 5.2 - Flowchart of UDF written to expand and contract boiling flask model.

5.1.3 – Mesh Independence

In order to determine the proper mesh size for CFD simulations, a mesh independence study was completed on various grid sizes. The six different base mesh parameters that were created in Harpoon (Sharc Ltd., Manchester, UK) are shown in Figure 5.3. The number of cells in the mesh models ranged from 32,253 (for a base of 1.4) to 95,762 cells (for a base of 0.85). Each mesh was created with hex dominant element types.

Base = 1.4						Base = 1.3						Base = 1.2					
Domain Extents:						Domain Extents:						Domain Extents:					
x-coordinate: min (m) = 1.591682e-005, max (m) = 5.440104e-002						x-coordinate: min (m) = 1.769447e-005, max (m) = 5.439926e-002						x-coordinate: min (m) = 1.959801e-005, max (m) = 5.439736e-002					
y-coordinate: min (m) = 1.907349e-009, max (m) = 6.096000e-002						y-coordinate: min (m) = 1.907349e-009, max (m) = 6.096000e-002						y-coordinate: min (m) = 1.907349e-009, max (m) = 6.096000e-002					
z-coordinate: min (m) = 3.783798e-005, max (m) = 5.437912e-002						z-coordinate: min (m) = 3.974343e-005, max (m) = 5.437722e-002						z-coordinate: min (m) = 4.165459e-005, max (m) = 5.437531e-002					
Volume statistics:						Volume statistics:						Volume statistics:					
minimum volume (m3): 7.097077e-011						minimum volume (m3): 5.471192e-011						minimum volume (m3): 4.128864e-011					
maximum volume (m3): 1.756161e-007						maximum volume (m3): 1.406081e-007						maximum volume (m3): 1.105921e-007					
total volume (m3): 8.697023e-005						total volume (m3): 8.698377e-005						total volume (m3): 8.700546e-005					
Face area statistics:						Face area statistics:						Face area statistics:					
minimum face area (m2): 2.269104e-007						minimum face area (m2): 1.967550e-007						minimum face area (m2): 1.601694e-007					
maximum face area (m2): 3.136001e-005						maximum face area (m2): 2.704001e-005						maximum face area (m2): 2.304001e-005					
Level Cells Faces Nodes Partitions						Level Cells Faces Nodes Partitions						Level Cells Faces Nodes Partitions					
0 32253 91074 25264 1						0 38027 107326 29801 1						0 45323 128181 35691 1					
Base = 1.0						Base = 0.9						Base = 0.85					
Domain Extents:						Domain Extents:						Domain Extents:					
x-coordinate: min (m) = 1.705551e-005, max (m) = 5.439990e-002						x-coordinate: min (m) = 1.959801e-005, max (m) = 5.439736e-002						x-coordinate: min (m) = 1.965714e-005, max (m) = 5.439730e-002					
y-coordinate: min (m) = 1.907349e-009, max (m) = 6.096000e-002						y-coordinate: min (m) = 1.907349e-009, max (m) = 6.096000e-002						y-coordinate: min (m) = 1.907349e-009, max (m) = 6.096000e-002					
z-coordinate: min (m) = 3.910446e-005, max (m) = 5.437786e-002						z-coordinate: min (m) = 4.165459e-005, max (m) = 5.437531e-002						z-coordinate: min (m) = 4.169846e-005, max (m) = 5.437526e-002					
Volume statistics:						Volume statistics:						Volume statistics:					
minimum volume (m3): 2.317378e-011						minimum volume (m3): 1.815876e-011						minimum volume (m3): 1.547921e-011					
maximum volume (m3): 6.400012e-008						maximum volume (m3): 4.665612e-008						maximum volume (m3): 3.930406e-008					
total volume (m3): 8.702509e-005						total volume (m3): 8.704079e-005						total volume (m3): 8.704825e-005					
Face area statistics:						Face area statistics:						Face area statistics:					
minimum face area (m2): 1.063792e-007						minimum face area (m2): 8.624303e-008						minimum face area (m2): 8.534106e-008					
maximum face area (m2): 1.600002e-005						maximum face area (m2): 1.296002e-005						maximum face area (m2): 1.156001e-005					
Level Cells Faces Nodes Partitions						Level Cells Faces Nodes Partitions						Level Cells Faces Nodes Partitions					
0 66901 190058 53723 1						0 84275 240200 68629 1						0 95762 272748 77673 1					

Figure 5.3 - Various base meshes created in Harpoon.

Each of the six meshes was simulated in Fluent using the same flow conditions described in 5.1.2.1. The code used to simulate the expanding bulb is described in Section 5.1.2.2.

To check grid independence of the velocity profiles occurring throughout the model, velocities were extracted along two locations in the bulb for each mesh size. The top rake (line at which velocities are extracted at uniform intervals) was taken in the stationary duct (at $y = 54.5$ mm from the bottom of the bulb), while the second rake was extracted in the expanding bulb at the location of the diameter (at $y = 26.8$ mm from the bottom of the bulb). The normalized velocity profiles at both rake locations for all six meshes can be seen in Figure 5.4.

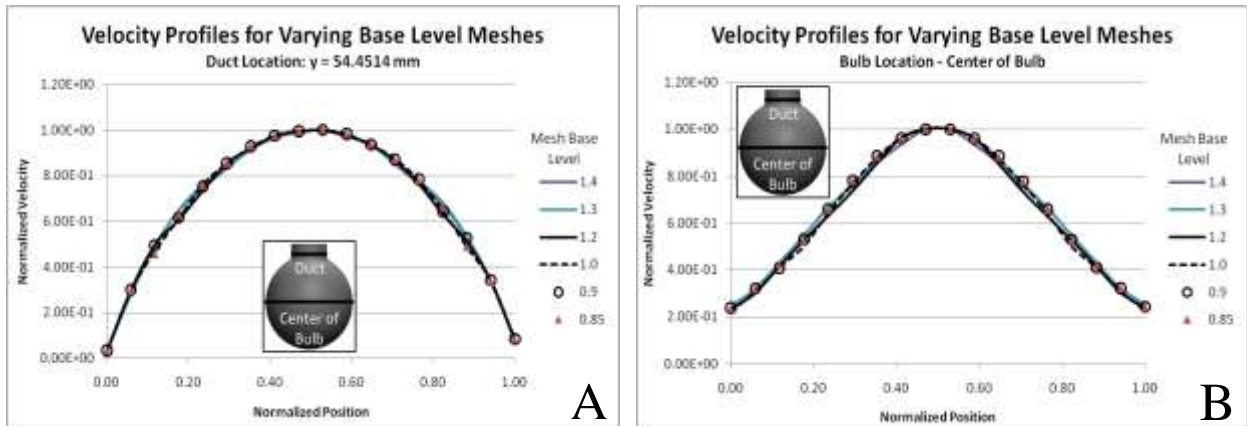


Figure 5.4 - Velocity profiles at time = 1.0 second for varying base level meshes occurring (A) in the stationary duct ($y = 54.5$ mm) and (B) in the center of the moving wall bulb ($y = 26.8$ mm).

It can be seen in Figure 5.4 that the velocity profiles are grid independent for mesh base levels less than or equal to 1.0. The red triangles (mesh = 0.85), black circles (mesh = 0.90), and black dotted line (mesh = 1.0) are overlapping; representing a grid independent solution. Therefore, a mesh size of 0.90 was chosen for final analysis and is shown in Figure 5.5 (see Figure 5.3 for the chosen mesh properties).

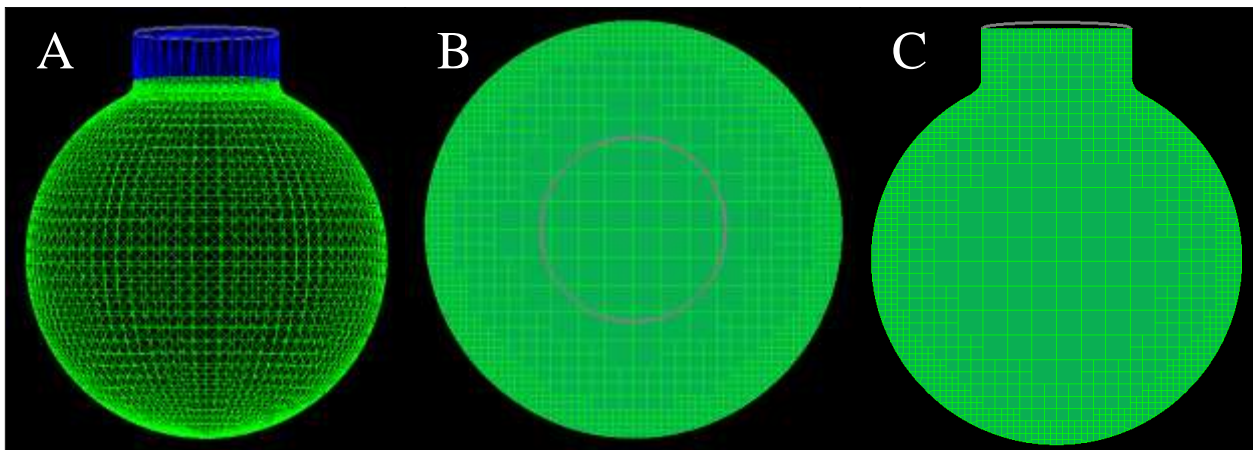


Figure 5.5 - (A) Harpoon 0.90 base level mesh of the bulb. (B) Top mesh view of a cross section of the center of the model and (C) side view of the center cross section of the model.

5.1.4 – CFD Results

An arbitrary flow time of 1.0 second was chosen to compare CFD to experimental results (corresponding to the 100th CFD case file when using a time step of 0.01 seconds). As described

above, two plane locations were chosen for analysis. In each plane, the velocity profiles were compared at two rake locations. The top and bottom rakes were taken 13.4 mm and 3.4 mm above the location of the diameter of the bulb, respectively, for both the 1st and 2nd plane locations (Figure 5.6).

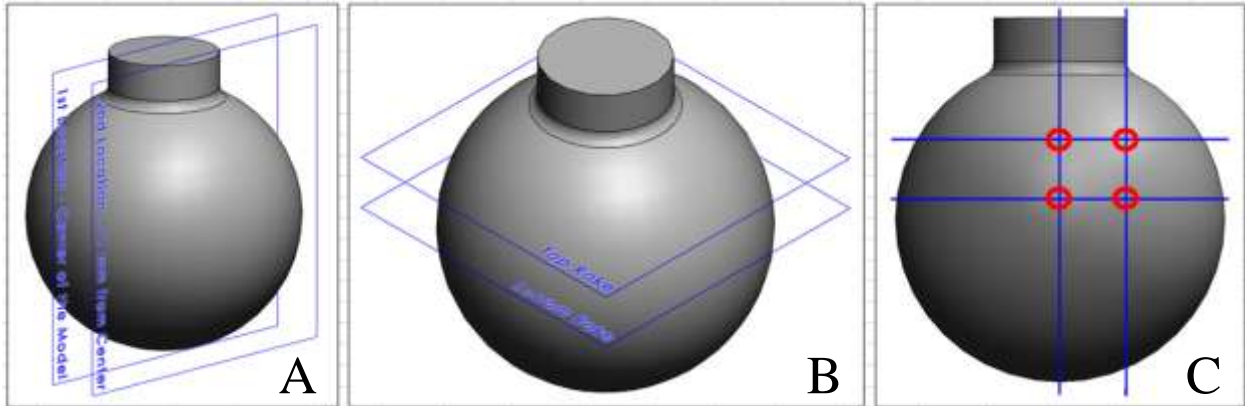


Figure 5.6 - (A) View representing both laser sheet planes, (B) view displaying the two rake locations, and (C) front view of the model showing all four rake locations.

5.1.4.1 – 1st Location – Center Plane of Bulb

Figure 5.7 represents the Fluent grid displaying the locations of the top and bottom rakes for the 1st location plane (occurring in the center plane of the bulb). An evenly spaced rake of 20 data points was extracted for both the top and bottom rakes. The CFD velocity profiles corresponding to the 1st location (center plane of the bulb model) top and bottom rakes can be seen in Figure 5.8 (for a flow time of 1.0 second). The positions (x-axis) were normalized to allow for comparison between the CFD and experimental results.

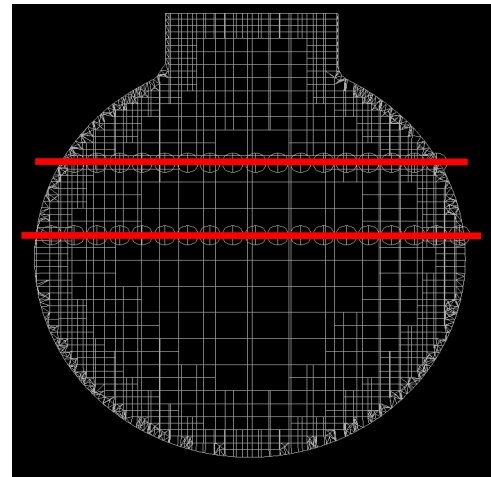


Figure 5.7 - Fluent grid showing top and bottom rakes.

For comparison, a second flow time of 0.5 seconds was analyzed for the same rake locations as specified above. The velocity fields occurring at this time for the 1st location can be seen in Figure 5.9. It is noted that the velocity magnitudes vary only slightly from time = 0.5 seconds to

time = 1.0 second. Because the model is expanding 9.5% over 2.5 seconds, the extents and dimensions of the bulb are changing by very small amounts throughout the expansion. Therefore, at a given rake location (constant y location from time = 0.5 seconds to time = 1.0 second), the extents of the bulb change slightly from 0.5 seconds to 1.0 second, and the velocity magnitudes remain similar between the two times (an average of 3.5% difference in magnitude between the top rake of time = 1.0 second and the top rake of time = 0.5 seconds and an average of 2.4% difference between the bottom rake of time = 1.0 second and the bottom rake of time = 0.5 seconds).

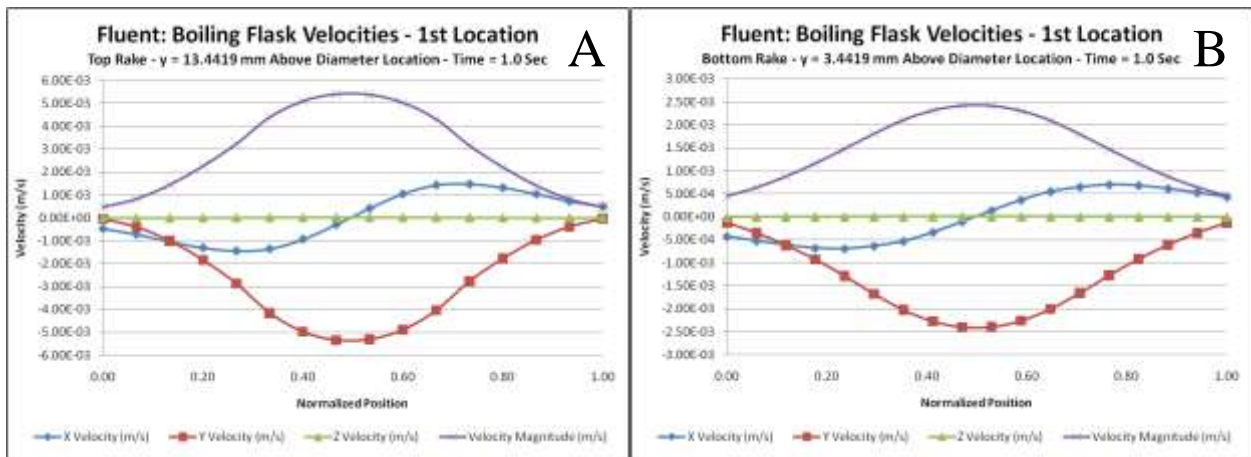


Figure 5.8 - Velocity profile plots at the 1st location (center plane of the bulb) for the (A) top rake ($y = 13.4$ mm above the diameter) and (B) bottom rake ($y = 3.4$ mm above the diameter) for time = 1.0 second.

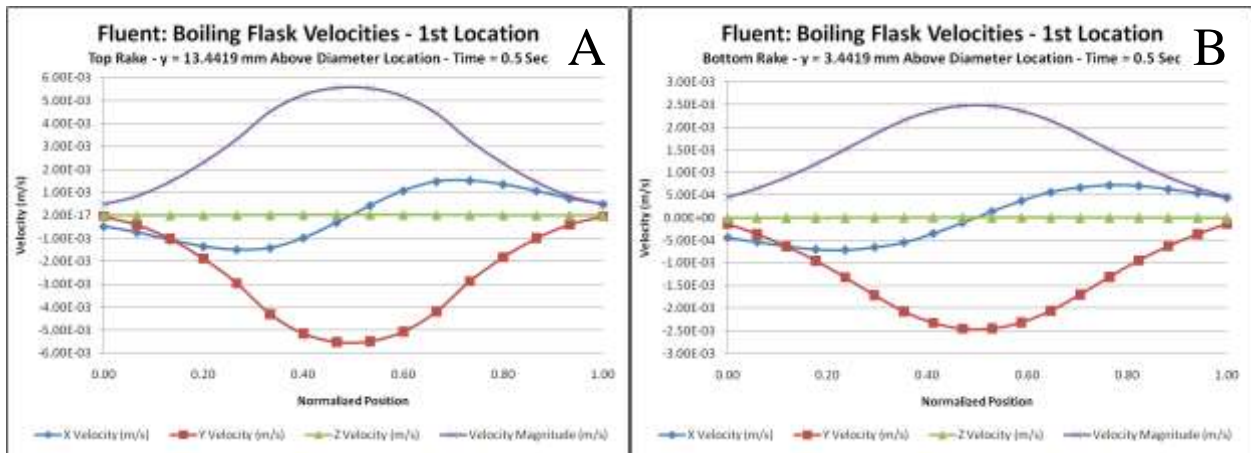


Figure 5.9 - Velocity profile plots at the 1st location (center plane of the bulb) for the (A) top rake ($y = 13.4$ mm above the diameter) and (B) bottom rake ($y = 3.4$ mm above the diameter) for time = 0.5 seconds.

5.1.4.2 – 2nd Location – 11 mm from Center Plane of Bulb

A second laser sheet location was chosen 11 mm offset from the center plane of the bulb for further validation (Figure 5.6A). Figure 5.10 shows the Fluent grid corresponding to the 2nd location where the top and bottom rake locations are visible (occurring at $y = 13.4$ mm and $y = 3.4$ mm above the diameter, respectively).

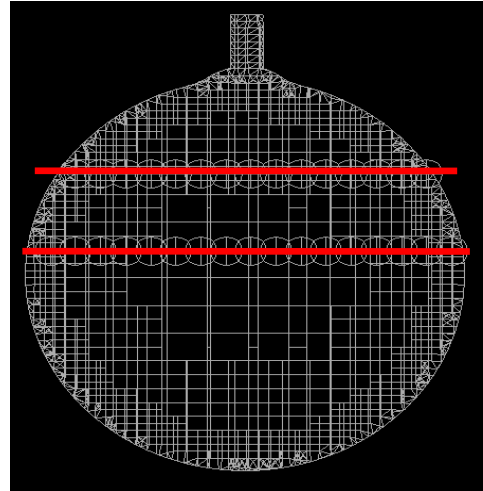


Figure 5.10 - 2nd Location showing top and bottom rakes.

The CFD velocity profiles corresponding to the 2nd location and a flow time of 1.0 second can be seen in Figure 5.11. Similarly, the Fluent results for the 2nd location occurring at a flow time = 0.5 seconds are shown in Figure 5.12. Again, the positions were normalized to allow for comparisons between the CFD and experimental results.

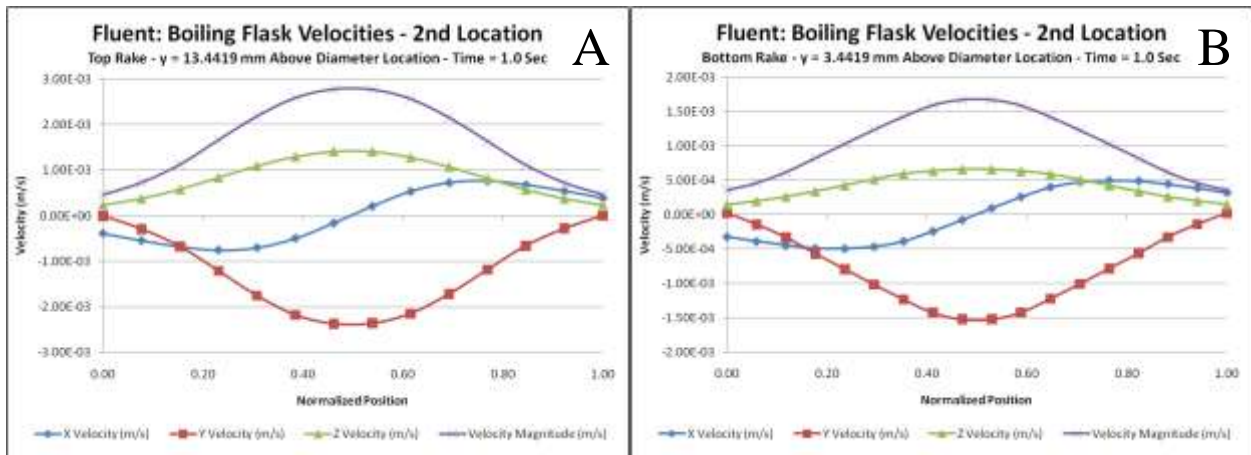


Figure 5.11 - Velocity profile plots at the 2nd location (11 mm from the center of the bulb) occurring at a flow time of 1.0 second for the (A) top rake ($y = 13.4$ mm above the diameter) and (B) bottom rake ($y = 3.4$ mm above the diameter).

Again, it is seen that the magnitudes between time = 0.5 seconds and time = 1.0 second vary slightly for a given rake location. For the 2nd location, the magnitudes vary by an average of 1.9% between the top rake of time = 1.0 second and the top rake of time = 0.5 seconds and an average of 1.8% between the bottom rake of time = 1.0 second and the bottom rake of time = 0.5 seconds.

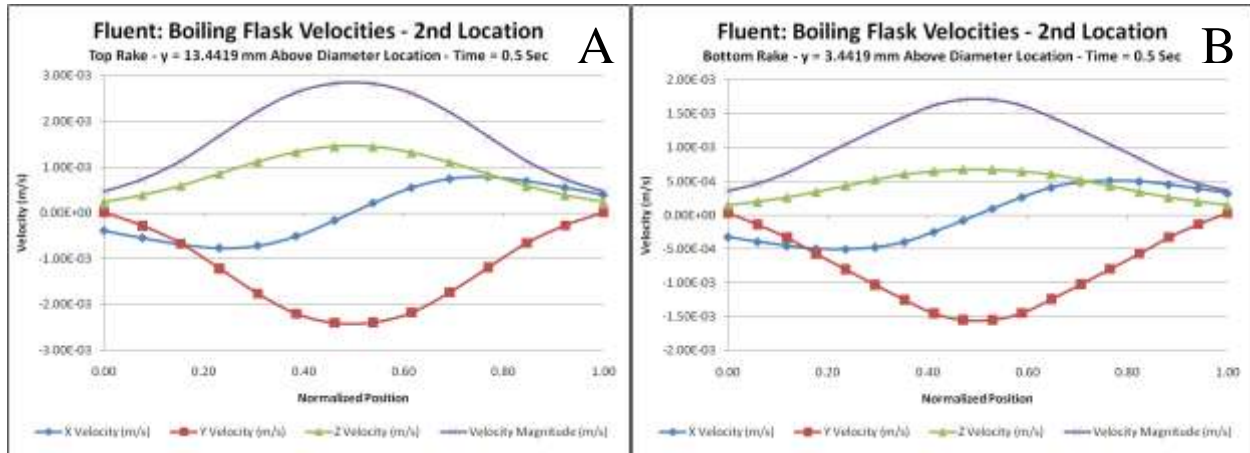


Figure 5.12 - Velocity profile plots at the 2nd location (11 mm from the center of the bulb) occurring at a flow time of 0.5 seconds for the (A) top rake ($y = 13.4$ mm above the diameter) and (B) bottom rake ($y = 3.4$ mm above the diameter).

5.2 – Experimental Methods Used for Validation

5.2.1 – Compliant Model Creation

Using the modeling techniques previously described in section 2.6, multiple compliant models of the boiling flask bulb were obtained. A single model was chosen for final analysis based on the quality of the model. Specifically, the most uniform model was chosen with the least amount of air bubbles or voids in the Ultraflex material; reducing the amount of laser refraction occurring throughout the model. The model was attached to the fitting in the experimental housing and filled with a glycerin/particle mix (approximately 0.007 grams / 150 mL of glycerin). Figure 5.13 represents the experimental boiling flask model used for stereoPIV validation. Note that the compliant model in Figure 5.13 is sitting on a flat surface so the bottom appears to be flat on the bottom.



Figure 5.13 - Compliant boiling flask model used for validation (model is sitting on flat surface).

5.2.2 – Experimental Setup

The experimental techniques described in Chapter 4 were applied to the boiling flask model for validation with the experimental setup shown in Figure 4.8. Similar to the CFD analysis, a

constant flow rate of 3.20 mL/sec was applied to the experimental boiling flask model (representing 9.5% expansion). Each of the cameras was set to 17° from the perpendicular of the light sheet (34° between cameras). In order to locate the center of the model for the 1st location analysis, the laser sheet was positioned at the diameter of the model (just inside the model membrane), then moved back towards the center 27.2 mm (the radius of the model). The distance from the object to the image was measured to be 25.75” (distance from the laser sheet plane to the CCD array in the camera). As stated above, the second laser sheet location was 11 mm from the center of the bulb model. The laser optics were moved 11 mm from the center location and the distance from the object to the image measured to be 25.30”.

5.2.4 – Insight 3G

The methods described in Chapter 4 were used to acquire and process the stereoPIV images for experimental validation. The settings used in the validation experiments are described in the following sections.

5.2.4.1 – Image Capture

Figure 5.14 represents the capture timing settings used to capture the validation images. Because the fluid flow is considered slow flow, single capture was used with a pulse rate of 20 Hz (delta T of 0.05 seconds between each frame). To reduce the effects of ambient light, an exposure time of 200 μs was used for each of the cameras. A trigger was used to configure the start of the image capture with the start of the LabVIEW pump motion (see Figure 4.9). Because a period of 5 seconds was used, a total of 100 pictures were required (20 pictures/second), but 105 images were actually captured to account for any residual fluid motion. In order to illustrate the repeatability of the experimental setup, three sets of data were taken for each of the two laser sheet locations. After each set of data was obtained,

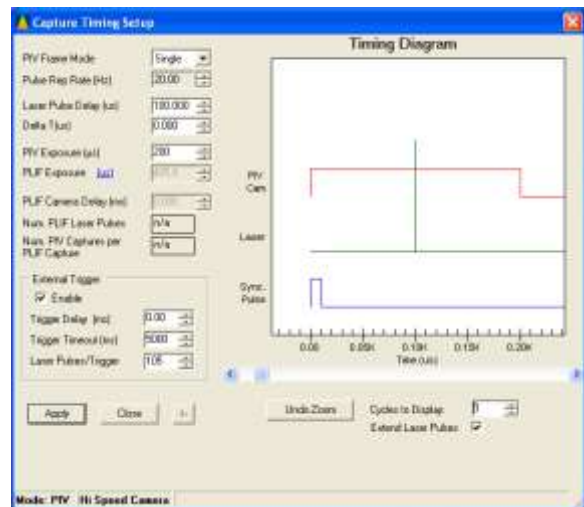


Figure 5.14 - TSI capture settings used for experimental validation.

the file names of the images were updated to represent image numbers (numbered from 0 to 104). Using a laser pulse delay of 100 μs and a ΔT of 50,000 μs , image pair 19 to 20 corresponds to a flow time of 1.0 second while pair 9 to 10 corresponds to a flow time of 0.5 seconds.

5.2.4.2 – Creating Calibration Files

Before image processing was started, optical calibrations were manually created to account for the magnification changes that occurred from one side of the image to the other (see section 4.4.1). The parameters used to create the 1st and 2nd location perspective calibration files are shown in Figure 5.15 and Figure 5.16, respectively. For example, the distance from the laser sheet (object) to the CCD array (image plane) was measured to be 654.05 mm for the 1st location. The values in the red boxes represent measured distances and angles acquired from the experimental setup while the purple boxes represent fixed specifications from the cameras used. The camera locations (blue boxes) were calculated by Insight based on the values from the red and purple boxes and were verified by measuring the distance from the light sheet to the front of the camera lens.



Figure 5.15 - Perspective calibration parameters used for 1st location.



Figure 5.16 - Perspective calibration parameters used for 2nd location.

A stereo AutoMapping procedure was then completed to optimize the perspective calibration by correcting the misalignment errors existing in the measurements between the light sheet location and the CCD array in the camera. This procedure was completed for each location to update the manual calibration files. A series of AutoMapping iterations was performed until the parameters were considered converged and the final pixel to length conversions calculated. Figure 5.17 represents the AutoMapping results for both laser sheet locations. It is seen that after the 4th iteration, each of the results were converged.

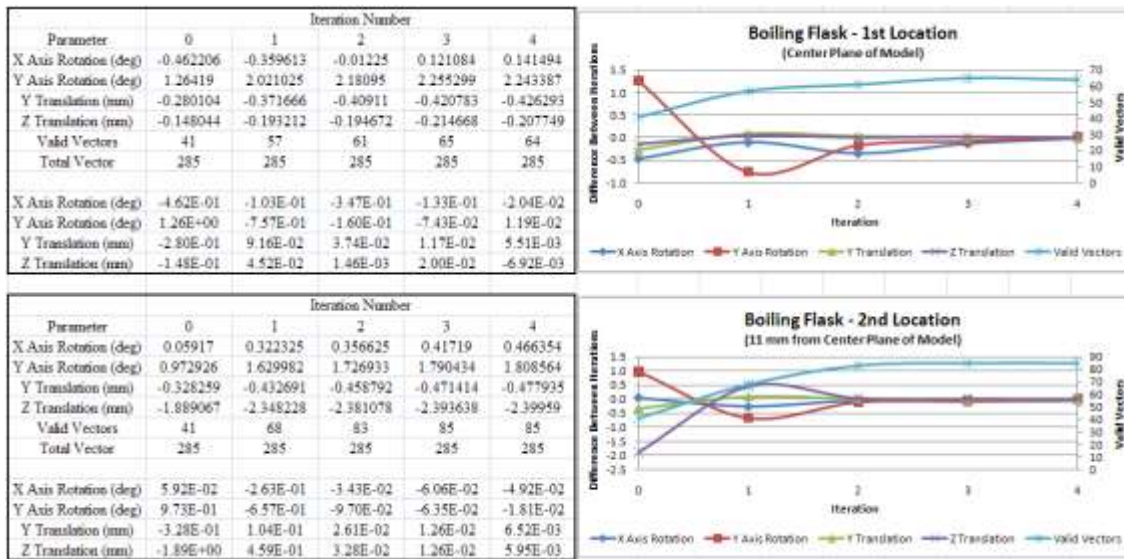


Figure 5.17 - Stereo AutoMapping results for the (Top) 1st location and (Bottom) 2nd location.

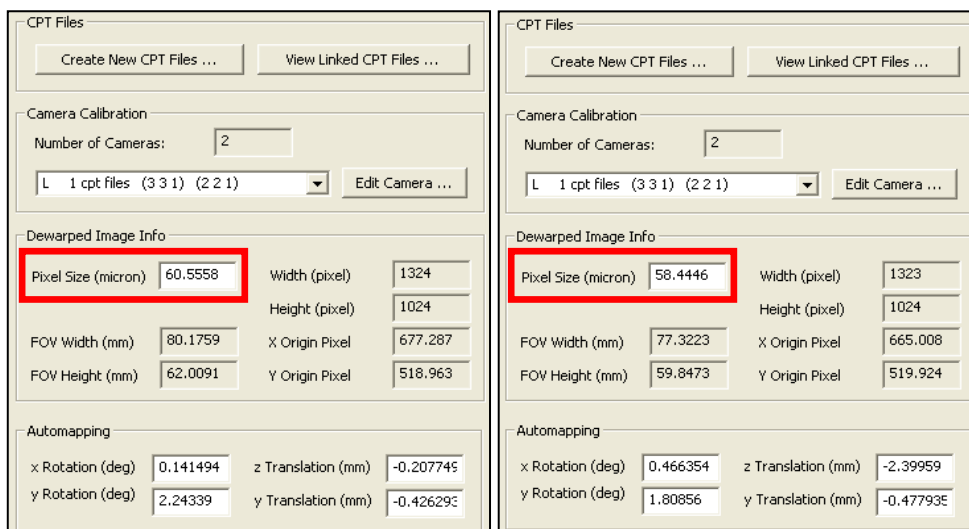


Figure 5.18 - Final calibration files for (Left) 1st location and (Right) second location after stereo AutoMapping. The red boxes represent the final conversion factors.

With the stereo AutoMapping results recorded, the calibration files were updated and shown in Figure 5.18. It is seen that the pixel to length conversion for the 1st location is 60.56 μm and 58.44 μm for the 2nd location. These conversions from pixels to physical distances are referred to here after as conversion factors.

5.4.2.3 – StereoPIV Processing Parameters

A processing mask was applied for each location to represent a processing boundary. All particles inside the boundary were analyzed while everything outside was ignored. Figure 5.19 represents the processing masks used for both the 1st and 2nd locations (shown as the dotted line). The image processing

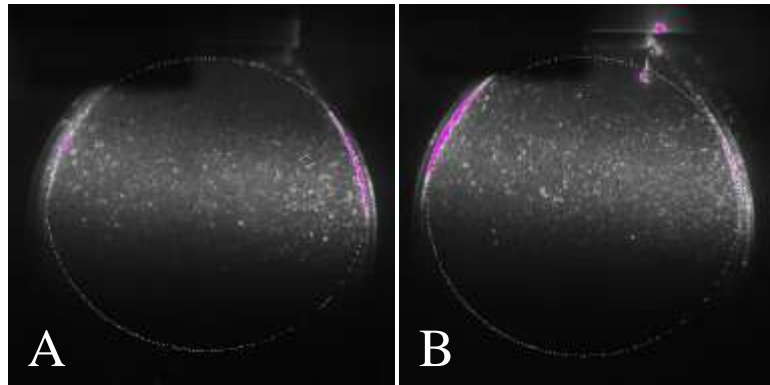


Figure 5.19 - Processing masks for (A) 1st location and (B) 2nd location.

parameters described in section 4.4.3 were applied to the boiling flask model. Using a deltaT of 50,000 μs , each of the image sets was analyzed with the appropriate optical calibration and processing mask applied.

5.2.5 – StereoPIV Results Compared to CFD

5.2.5.1 – 1st Location – Center Plane of Bulb

Three different data sets were collected for the 1st laser sheet location. Figure 5.20 displays the LabVIEW outputs from the three sets of collected data.



Figure 5.20 - LabVIEW outputs for the 1st locations (A) 1st set, (B) 2nd set, and (C) 3rd set.

Corresponding to the rakes taken from the CFD results, velocity profiles were extracted for each of the data sets at two rake locations. The top and bottom rakes were taken 13.4 mm and 3.4 mm above the location of the diameter of the bulb, respectively. Figure 5.21 displays the locations of the top and bottom rakes with velocity vectors contoured by velocity magnitude.

Figure 5.22 represents the stereoPIV velocity profiles for time = 1.0 second for both the top and bottom rake locations ($y = 13.4$ mm above the diameter and $y = 3.4$ mm above the diameter, respectively), while Figure 5.23 represents the results occurring at time = 0.5 seconds. The results from all three collected data sets are shown on the same plot to illustrate the repeatability of the stereoPIV experiments. It is shown that the experiments are repeatable because the sets are overlapping (dotted line represents 1st set, solid line represents 2nd set, and circles represent the 3rd set).

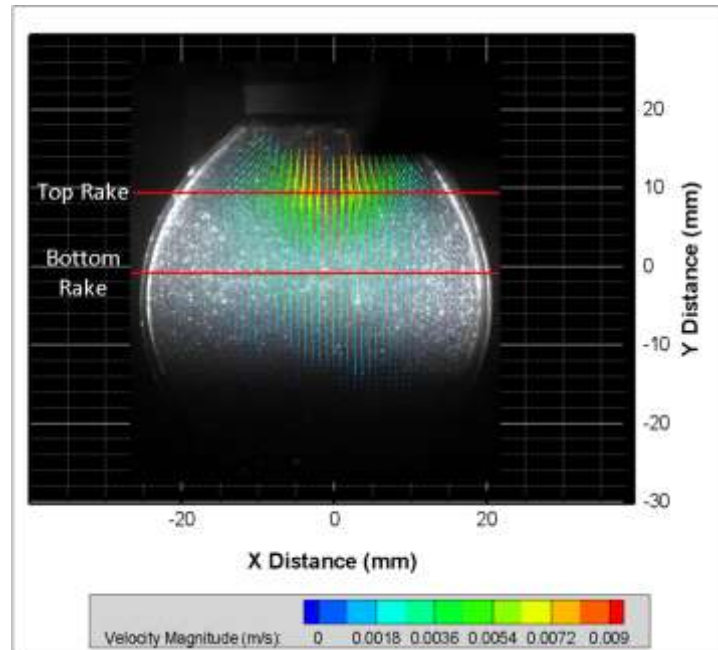


Figure 5.21 - Top and bottom rake locations for the 1st laser sheet location (center of the bulb model).

Similar to the CFD results (section 5.1.4.1), the velocity magnitudes of the stereoPIV results should vary only slightly between time = 1.0 second and time = 0.5 seconds (1.8% difference for CFD predictions). It is seen, however, that the experimental average maximum y-velocity magnitude between the top rake of time = 1.0 seconds (average velocity = $-4.76E-3$ m/s) and top rake of time = 0.5 second (average velocity = $-4.44E-3$ m/s) varies by 7.0%. This indicates that the experimental results between different physical times can vary by approximately 7.0% with the larger times having better agreement with the predicted results.

Absolute differences and percent differences relative to velocity magnitude (based on maximum velocities) were calculated between stereoPIV and predicted CFD results for each velocity component and are shown in Table 5.1 and Table 5.2, respectively.

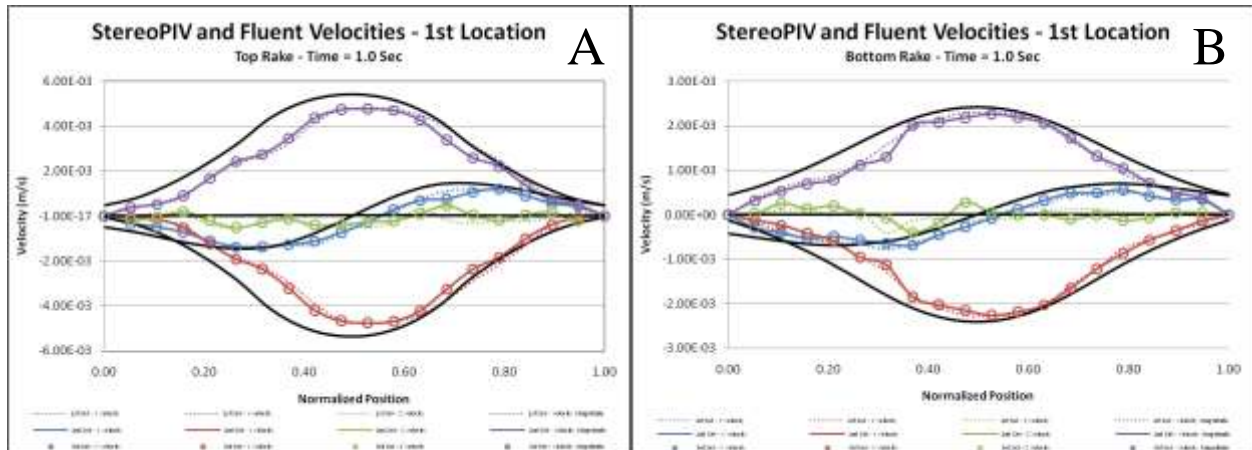


Figure 5.22 - StereoPIV velocity profiles for time = 1.0 second with the predicted CFD results (shown as black solid lines) for the (A) top rake location ($y = 13.4$ mm above the diameter) and (B) the bottom rake location ($y = 3.4$ mm above the diameter) for the 1st laser sheet location (Purple = velocity magnitude, Blue = x-velocity, Red = y-velocity, Green = z-velocity). Different sets are indicated by dashed lines, solid lines, and circles.

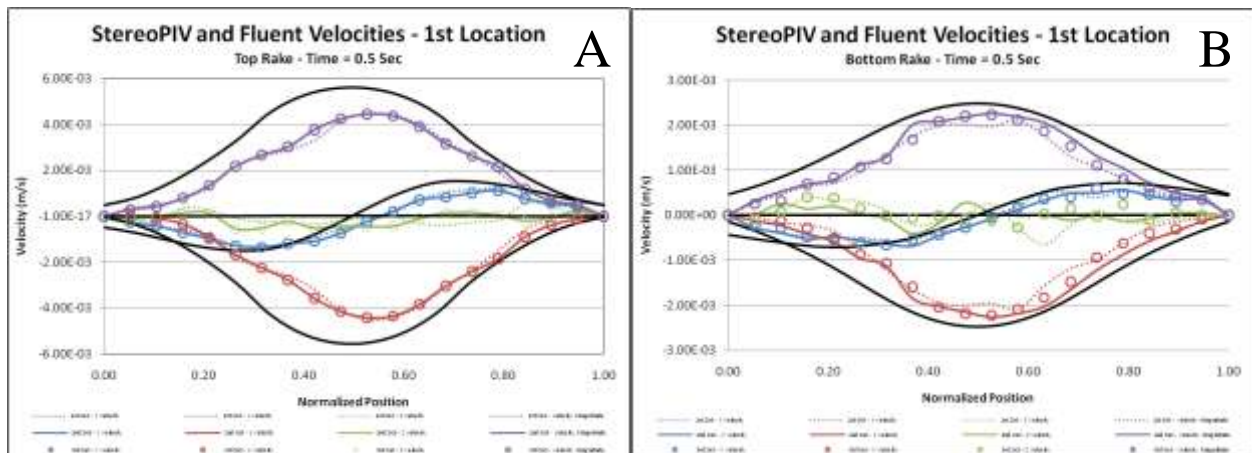


Figure 5.23 - StereoPIV velocity profiles for time = 0.5 seconds with the predicted CFD results (shown as black solid lines) for the (A) top rake location ($y = 13.4$ mm above the diameter) and (B) the bottom rake location ($y = 3.4$ mm above the diameter) for the 1st laser sheet location (Purple = velocity magnitude, Blue = x-velocity, Red = y-velocity, Green = z-velocity). Different sets are indicated by dashed lines, solid lines, and circles.

Table 5.1 - Absolute difference (based on maximum velocity) between stereoPIV and predicted CFD results using the conversion factor calculated in Insight 3G. (VM = velocity magnitude)

1st Location - Insight 3G Calculated Conversion Factor = 60.56 μm									
Top Rake Location ($y = 13.4$ mm above diameter)					Bottom Rake Location ($y = 3.4$ mm above diameter)				
Time = 1.0 Second					Time = 1.0 Second				
	X	Y	Z	VM		X	Y	Z	VM
Avg	2.72E-04	5.78E-04	3.98E-04	6.12E-04	Avg	1.63E-04	1.32E-04	2.16E-04	1.43E-04
Time = 0.5 Seconds					Time = 0.5 Seconds				
	X	Y	Z	VM		X	Y	Z	VM
Avg	3.75E-04	1.08E-03	2.99E-04	1.12E-03	Avg	1.61E-04	2.65E-04	3.55E-04	2.72E-04

Table 5.2 - Percent difference relative to velocity magnitude (based on maximum velocity) between stereoPIV and predicted CFD results using the conversion factor calculated in Insight 3G. (VM = velocity magnitude)

1st Location - Insight 3G Calculated Conversion Factor = 60.56 μm									
Top Rake Location ($y = 13.4$ mm above diameter)					Bottom Rake Location ($y = 3.4$ mm above diameter)				
Time = 1.0 Second					Time = 1.0 Second				
	X	Y	Z	VM		X	Y	Z	VM
Avg	-5.0%	10.7%	7.4%	-11.3%	Avg	-6.7%	5.5%	8.9%	-5.9%
Time = 0.5 Seconds					Time = 0.5 Seconds				
	X	Y	Z	VM		X	Y	Z	VM
Avg	-6.7%	19.4%	5.4%	-20.0%	Avg	-6.5%	10.7%	14.3%	-11.0%

The error in Table 5.1 was reduced by examining the conversion factor. An optical test was completed to verify that the conversion being calculated in Insight was correct and to insure that the index

matching between the compliant model and the carrier fluid was sufficient; not introducing error to the results.

With the boiling flask model

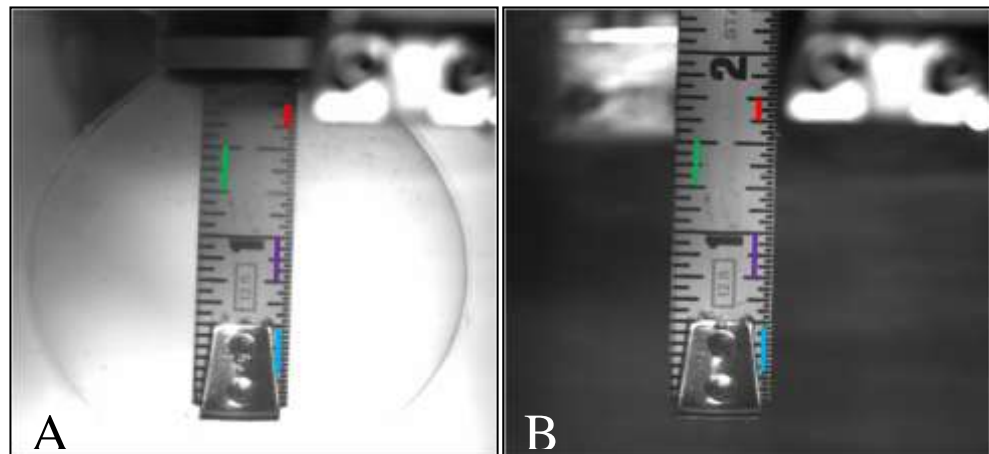


Figure 5.24 - (A) Scale inserted into compliant model and (B) scale removed from model. (Both occur in the center plane of the model)

installed in the experimental housing, a scale was inserted at the center plane of the model and an image acquired. The model was then removed from the setup and the scale replaced to obtain a

second image (Figure 5.24). Table 5.3 represents the measured distances, the number of pixels that represents the known lengths (calculated in ImageJ), and the resulting pixel to length conversion factors corresponding to the colored lines in Figure 5.24.

Table 5.3 - Measured distances corresponding to the colored lines in Figure 5.24.

With Bulb	Length (in)	Pixels	Pixel to Length Ratio ($\mu\text{m} / \text{pixel}$)	Without Bulb	Length (in)	Pixels	Pixel to Length Ratio ($\mu\text{m} / \text{pixel}$)
Red Line	1/8	50	63.50	Red Line	1/8	50	63.50
Green Line	1/4	100	63.50	Green Line	1/4	99	64.14
Purple Line	1/4	98	64.80	Purple Line	1/4	98	64.80
Blue Line	1/4	98	64.80	Blue Line	1/4	98	64.80

Average Pixel to Length Conversion Factor = 64.15 $\mu\text{m}/\text{pixel}$	Average Pixel to Length Conversion Factor = 64.31 $\mu\text{m}/\text{pixel}$
--	--

An average measured pixel to length conversion factor was then calculated and compared to the conversion factor used for the above analyses. It is clear from the similarities in pixel to length conversions from each of the two conditions that we successfully indexed matched the compliant model material with the carrier fluid. We can also conclude that large errors are not being introduced between the CFD and experimental results because of refraction. However, the previous conversion calculated in Insight was 60.56 $\mu\text{m}/\text{pixel}$ for the first location (Figure 5.18), but the newly measured conversion was 64.23 μm per pixel (a 6% difference). This difference in conversion factors introduces a significant amount of error because the sizes of the images are 1324 x 1024 (Figure 5.18). The 4 μm per pixel difference between the Insight and the measured conversion factors leads to a 5.3 mm difference in the width of the image and a 4.1 mm difference in the height of the image.

Particle displacements are measured in pixels then converted to physical lengths to finally calculate velocities. If an inconsistency exists in the conversion factor the velocity magnitudes will be incorrect. Therefore, the stereoPIV results from the above analyses were scaled based on new measured conversion factor and compared to the predicted CFD results. For example, each velocity vector from Figure 5.22 and Figure 5.23 was multiplied by the ratio of the new conversion factor to the old (64.23 / 60.56). Figure 5.25 and Figure 5.26 represent the stereoPIV velocity profiles compared to the predicted CFD results using the newly measured conversion factor for time = 1.0 second and time = 0.5 seconds, respectively. It is seen that the velocity

magnitudes agree better with the predicted CFD results using the measured conversion factor. Table 5.4 and Table 5.5 represent the absolute differences and percent differences relative to velocity magnitude (based on maximum velocity) that exist between the stereoPIV and predicted CFD results when using the newly measured conversion factor; indicating that the percent differences have decreased. For example, the relative percent difference between the y-velocity component for the top rake at time = 1.0 second decreases from 10.7% to 5.4% when using the measured conversion factor.

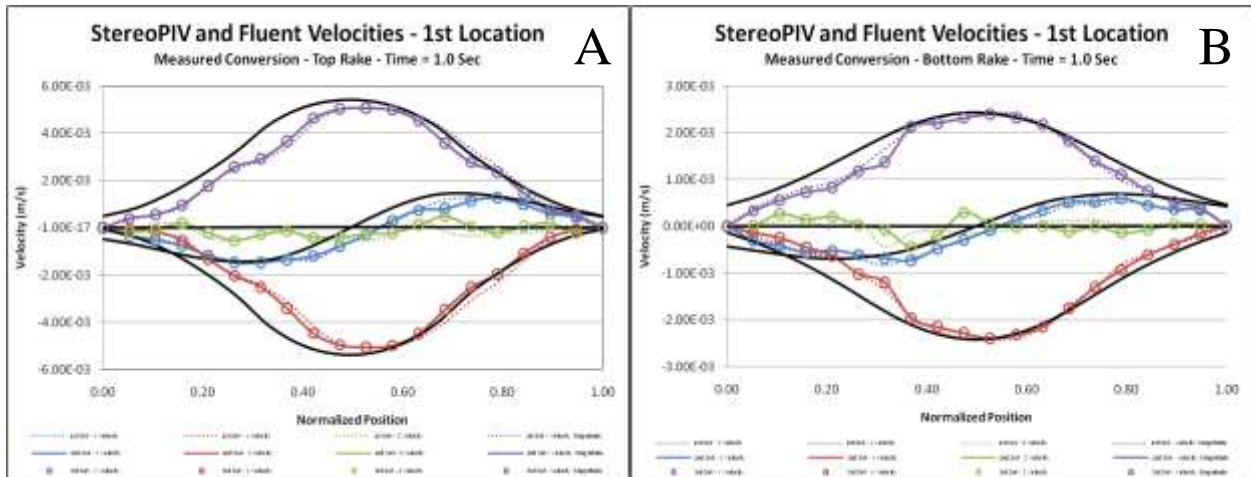


Figure 5.25 - StereoPIV velocity profiles using the measured conversion factor (1 pix = 64.24 μm) for time = 1.0 second with the predicted CFD results (shown as black solid lines) for the (A) top rake location and (B) bottom rake location for the 1st laser sheet location (Purple = velocity magnitude, Blue = x-velocity, Red = y-velocity, Green = z-velocity. Different sets are indicated by dashed lines, solid lines, and circles).

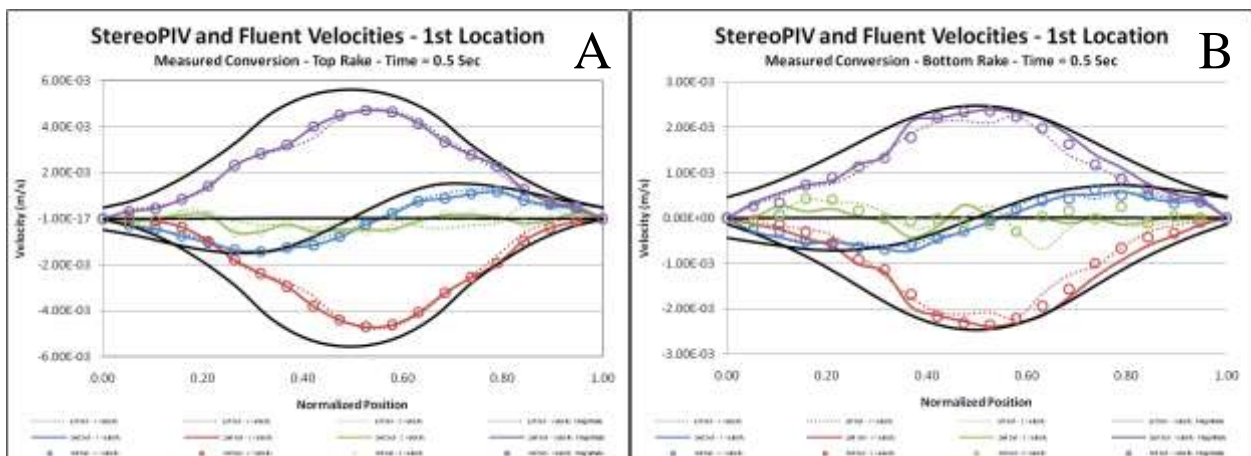


Figure 5.26 - StereoPIV velocity profiles using the measured conversion factor (1 pix = 64.24 μm) for time = 0.5 seconds with the predicted CFD results (shown as black solid lines) for the (A) top rake location and (B) bottom rake location for the 1st laser sheet location (Purple = velocity magnitude, Blue = x-velocity, Red = y-velocity, Green = z-velocity. Different sets are indicated by dashed lines, solid lines, and circles).

Table 5.4 - Absolute difference (based on maximum velocity) between stereoPIV and predicted CFD results using the measured conversion factor. (VM = velocity magnitude)

1st Location - Measured Conversion Factor = 64.24 μm									
Top Rake Location (y = 13.4 mm above diameter)					Bottom Rake Location (y = 3.4 mm above diameter)				
Time = 1.0 Second					Time = 1.0 Second				
	X	Y	Z	VM		X	Y	Z	VM
Avg	1.99E-04	2.89E-04	4.23E-04	3.22E-04	Avg	1.30E-04	5.02E-06	2.29E-04	5.01E-06
Time = 0.5 Seconds					Time = 0.5 Seconds				
	X	Y	Z	VM		X	Y	Z	VM
Avg	3.06E-04	8.10E-04	3.19E-04	8.46E-04	Avg	1.27E-04	1.32E-04	3.77E-04	1.39E-04

Table 5.5 - Percent difference relative to velocity magnitude (based on maximum velocity) between stereoPIV and predicted CFD results using the measured conversion factor. (VM = velocity magnitude)

1st Location - Measured Conversion Factor = 64.24 μm									
Top Rake Location (y = 13.4 mm above diameter)					Bottom Rake Location (y = 3.4 mm above diameter)				
Time = 1.0 Second					Time = 1.0 Second				
	X	Y	Z	VM		X	Y	Z	VM
Avg	-3.7%	5.4%	7.8%	-6.0%	Avg	-5.4%	-0.2%	9.5%	-0.2%
Time = 0.5 Seconds					Time = 0.5 Seconds				
	X	Y	Z	VM		X	Y	Z	VM
Avg	-5.5%	14.5%	5.7%	-15.2%	Avg	-5.1%	5.3%	15.2%	-5.6%

5.2.5.2 – 2nd Location – 11mm from Center Plane of Bulb

Figure 5.27 displays the LabVIEW outputs from the three sets of collected data for the 2nd laser sheet location (11 mm from the center plane of the bulb).



Figure 5.27 - LabVIEW outputs for the 2nd locations (A) 1st set, (B) 2nd set, and (C) 3rd set.

Figure 5.28 represents the locations of the top and bottom rakes with respect to the diameter of the model for the 2nd laser sheet location. Similar to the 1st laser sheet location, the top rake

occurs 13.4 mm above the diameter while the bottom rake is 3.4 mm above the diameter of the bulb. Velocity vectors contoured by velocity magnitude are also displayed.

Using the calculated Insight 3G conversion factor for the 2nd location (1 pix = 58.44 μm), Figure 5.29 and Figure 5.30 represent the stereoPIV with the predicted CFD results for time = 1.0 second and time = 0.5 seconds, respectively. Table 5.6 and Table 5.7 represent the absolute differences and percent differences relative to velocity magnitude (based on maximum velocities) between the stereoPIV and predicted CFD results for each component of velocity, respectively.

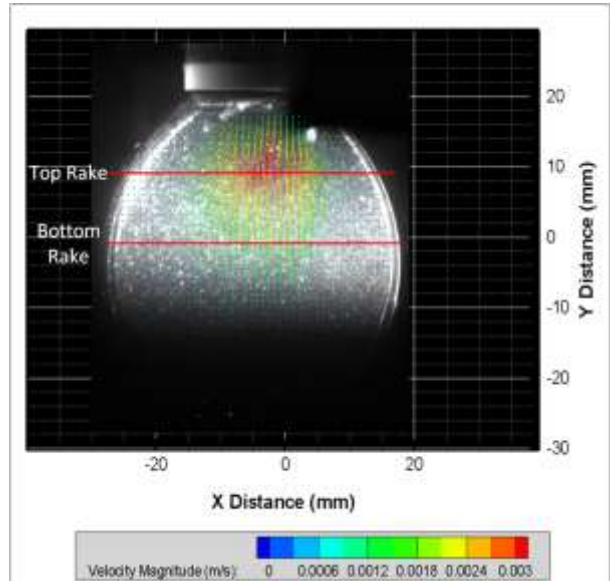


Figure 5.28 - Top and bottom rake locations for the 2nd laser sheet location.

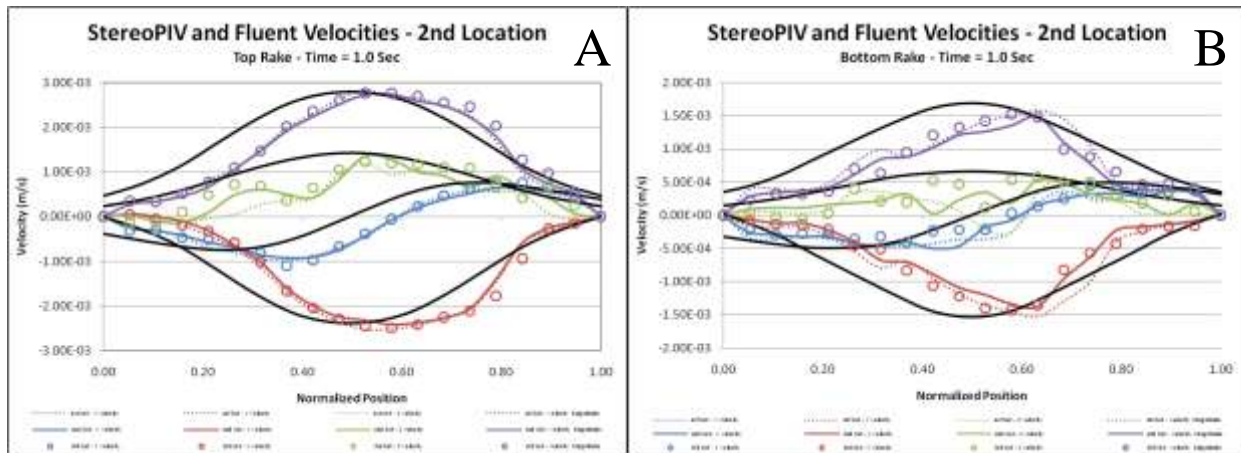


Figure 5.29 - StereoPIV velocity profiles for time = 1.0 second with the predicted CFD results (shown as black solid lines) for the (A) top rake location (y = 13.4 mm above the diameter) and (B) the bottom rake location (y = 3.4 mm above the diameter) for the 2nd laser sheet location (Purple = velocity magnitude, Blue = x-velocity, Red = y-velocity, Green = z-velocity). Different sets are indicated by dashed lines, solid lines, and circles).

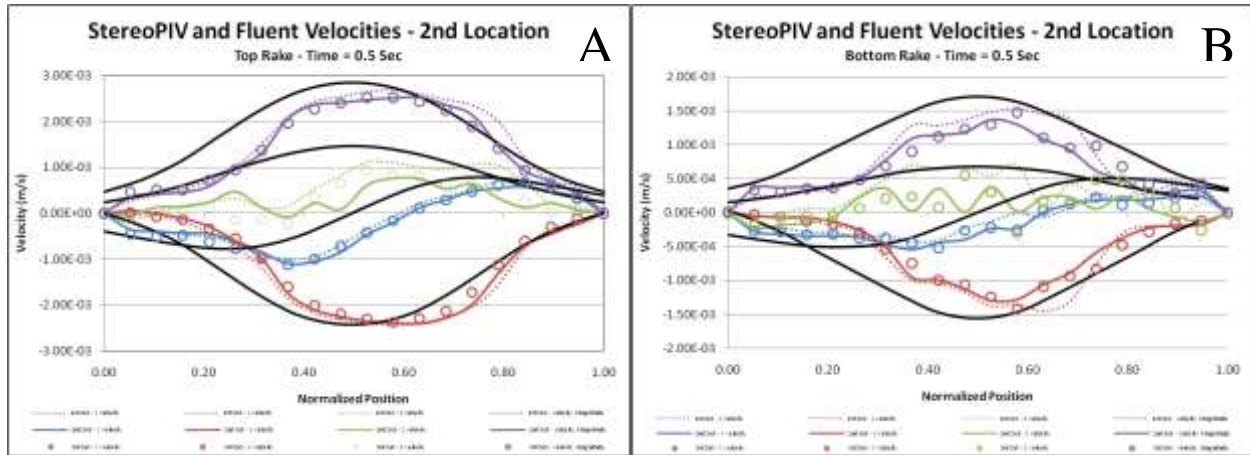


Figure 5.30 - StereoPIV velocity profiles for time = 0.5 seconds with the predicted CFD results (shown as black solid lines) for the (A) top rake location ($y = 13.4$ mm above the diameter) and (B) the bottom rake location ($y = 3.4$ mm above the diameter) for the 2nd laser sheet location (Purple = velocity magnitude, Blue = x-velocity, Red = y-velocity, Green = z-velocity). Different sets are indicated by dashed lines, solid lines, and circles.

Table 5.6 - Absolute difference (based on maximum velocity) between stereoPIV and predicted CFD results using the conversion factor calculated in Insight 3G. (VM = velocity magnitude)

2nd Location - Insight 3G Calculated Conversion Factor = 58.44 μm									
Top Rake Location ($y = 13.4$ mm above diameter)					Bottom Rake Location ($y = 3.4$ mm above diameter)				
Time = 1.0 Second					Time = 1.0 Second				
	X	Y	Z	VM		X	Y	Z	VM
Avg	1.82E-04	1.89E-04	4.19E-04	3.89E-04	Avg	2.76E-04	6.52E-04	7.10E-04	9.30E-04
Time = 0.5 Seconds					Time = 0.5 Seconds				
	X	Y	Z	VM		X	Y	Z	VM
Avg	1.52E-04	8.84E-04	2.74E-04	9.01E-04	Avg	1.86E-04	1.60E-04	1.24E-04	2.45E-04

Table 5.7 - Percent difference relative to velocity magnitude (based on maximum velocity) between stereoPIV and predicted CFD results using the conversion factor calculated in Insight 3G. (VM = velocity magnitude)

2nd Location - Insight 3G Calculated Conversion Factor = 58.44 μm									
Top Rake Location ($y = 13.4$ mm above diameter)					Bottom Rake Location ($y = 3.4$ mm above diameter)				
Time = 1.0 Second					Time = 1.0 Second				
	X	Y	Z	VM		X	Y	Z	VM
Avg	-6.6%	6.8%	-15.1%	-14.0%	Avg	-9.7%	23.0%	-25.1%	-32.9%
Time = 0.5 Seconds					Time = 0.5 Seconds				
	X	Y	Z	VM		X	Y	Z	VM
Avg	9.1%	-52.8%	16.3%	53.8%	Avg	-10.9%	9.4%	-7.3%	-14.4%

Similar to the 1st laser sheet location, a new calibration conversion was desired to check the accuracy of the calculated factor (currently 58.4 $\mu\text{m}/\text{pixel}$). However, at the 2nd location, a scale

was unable to be inserted into the housing. Therefore, multiple locations outside of the setup were captured to establish a trend then interpolated at the 2nd location. The measured conversion factor was found to be 61.36 μm . Figure 5.31 and Figure 5.32 represent the stereoPIV velocity profiles compared to the predicted CFD results using the newly measured conversion factor for time = 1.0 second and time = 0.5 seconds, respectively.

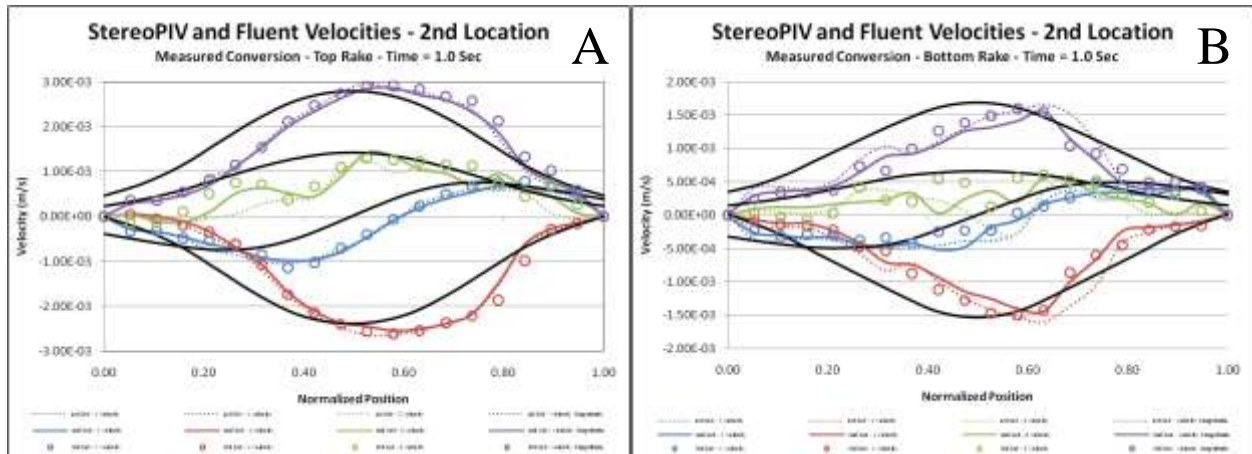


Figure 5.31 - StereoPIV velocity profiles using the measured conversion factor (1 pix = 61.36 μm) for time = 1.0 second with the predicted CFD results (shown as black solid lines) for the (A) top rake location and (B) bottom rake location for the 2nd laser sheet location (Purple = velocity magnitude, Blue = x-velocity, Red = y-velocity, Green = z-velocity. Different sets are indicated by dashed lines, solid lines, and circles).

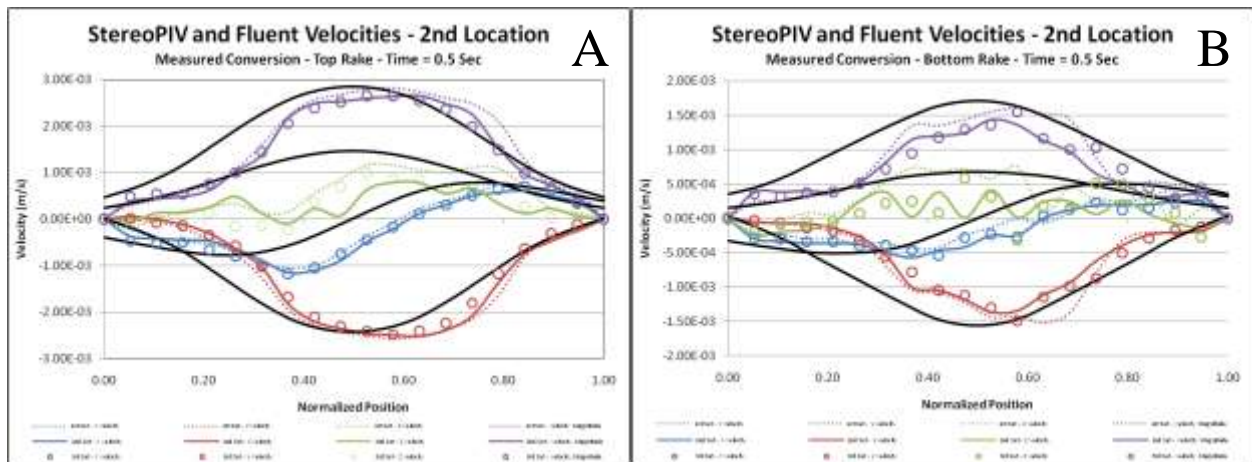


Figure 5.32 - StereoPIV velocity profiles using the measured conversion factor (1 pix = 61.36 μm) for time = 0.5 seconds with the predicted CFD results (shown as black solid lines) for the (A) top rake location and (B) bottom rake location for the 2nd laser sheet location (Purple = velocity magnitude, Blue = x-velocity, Red = y-velocity, Green = z-velocity. Different sets are indicated by dashed lines, solid lines, and circles).

Table 5.8 and Table 5.9 represent the differences (absolute and percent difference relative to velocity magnitude) that exist between the experimental and predicted CFD results using the

measured conversion factor, respectively. Again, an overall better agreement was found between the stereoPIV and the predicted CFD results when using the measured conversion factor.

Table 5.8 - Absolute difference (based on maximum velocity) between stereoPIV and predicted CFD results using the measured conversion factor. (VM = velocity magnitude)

2nd Location - Measured Conversion Factor = 61.36 μm									
Top Rake Location (y = 13.4 mm above diameter)					Bottom Rake Location (y = 3.4 mm above diameter)				
Time = 1.0 Second					Time = 1.0 Second				
	X	Y	Z	VM		X	Y	Z	VM
Avg	6.71E-05	2.29E-04	8.65E-05	1.33E-04	Avg	3.56E-04	8.85E-04	8.69E-04	1.22E-03
Time = 0.5 Seconds					Time = 0.5 Seconds				
	X	Y	Z	VM		X	Y	Z	VM
Avg	1.84E-04	1.00E-03	3.20E-04	1.03E-03	Avg	1.70E-04	9.08E-05	9.68E-05	1.72E-04

Table 5.9 - Percent difference relative to velocity magnitude (based on maximum velocity) between stereoPIV and predicted CFD results using the measured conversion factor. (VM = velocity magnitude)

2nd Location - Measured Conversion Factor = 61.36 μm									
Top Rake Location (y = 13.4 mm above diameter)					Bottom Rake Location (y = 3.4 mm above diameter)				
Time = 1.0 Second					Time = 1.0 Second				
	X	Y	Z	VM		X	Y	Z	VM
Avg	-2.4%	-8.2%	-3.1%	4.8%	Avg	-12.6%	31.3%	-30.7%	-43.2%
Time = 0.5 Seconds					Time = 0.5 Seconds				
	X	Y	Z	VM		X	Y	Z	VM
Avg	11.0%	-59.9%	19.1%	61.4%	Avg	-10.0%	5.3%	-5.7%	-10.1%

5.3 – Conclusions About Boiling Flask Experiments

The above analyses have shown that the experimental setup and processes being used to acquire and analyze stereoPIV data yield accurate results. Several conclusions and suggestions have been made for future analyses and are summarized below:

- A constant applied flow rate should be used to expand and contract the experimental model to maximize control of the expansion. This flow rate should be at least 3 mL/sec to allow for the appropriate pixel displacements to occur between each image set (using a deltaT of 0.05 seconds between each image). An alternative to increasing the flow rate would be to decrease the laser pulsing frequency (currently 20 pulses / sec). If the frequency were decreased, the deltaT between frames would increase, and a larger displacement would occur between sequential image sets.

- When creating a manual perspective calibration file (calculated by Insight), it is important to correctly measure and enter the appropriate distance from the image to the object. If this distance is off by a slight amount, the conversion from pixels to physical length (conversion factor) will be incorrect and will lead to large differences in the velocity magnitudes. It is also important to create a measured conversion factor and scale the results by the ratio of the measured to the calculated factor to correct any errors that may be induced by the conversion factor calculated by Insight (see section 5.2.5.1)
- In order to properly capture the motion of the seeded particles, a minimum of five to eight pixels must be displaced between an image pair. Therefore, velocity profile rakes are more accurate when extracted at locations that yield high particle displacement (typically near the inlet).
- As seen between the results from time = 1.0 second to time = 0.5 seconds, a larger physical time is desired for more uniform and accurate results.
- The presence of large error for the z-component of velocity between the stereoPIV and predicted CFD results is occurring because the camera angles from the light sheet were not optimized. As explained in section 4.1, a camera angle is ideal as to capture the pure z-component of velocity. However, because the angles used in this work were relatively small (to allow for the image in the light sheet to be in focus from one side of the image to the other), the accuracy of the z-component was significantly reduced. If future work is completed, the use of Scheimpflug mounts is recommended. These would allow the camera angles to be maximized without sacrificing the quality of the images and yield the smallest z-component errors.
- Be aware of the non-uniform expansion that exists in the experimental setup. If the model tends to expand towards the pump location, the skew depicted in Figure 5.33 will occur (the velocity on the left side will be less than predicted and the velocity on the right will be slightly higher than predicted). The solid red line indicates where the rake should be occurring. If uniform expansion was occurring, the rake would be a straight line across the model (left image). However, if the expansion is non-uniform, the location of the rake is no longer horizontal and the dotted line would represent the actual rake location. The blue arrows indicate that the actual rake yields less than predicted velocities on the left side of the model with higher velocities occurring on the right side. The effects of non-uniform

expansion are illustrated in the above results section (section 5.2.5). Figure 5.29, for example, shows velocities less than predicted on the left side of the model, but higher than predicted on the right side; an indication of non-uniform expansion of the experimental model.

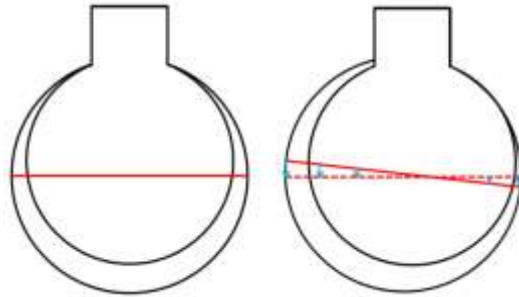


Figure 5.33 - Difference in velocity profile caused by non-uniform expansion.

Chapter 6: StereoPIV Results in Alveolus Models

6.1 – Experimental Healthy Human Model

A total of forty-two data sets were collected for the healthy human model; three sets of data for each of the fourteen different laser plane locations. In order to illustrate the three-dimensional effects of all of the results, six laser locations were analyzed and compared. Figure 6.1 represents the isometric and top views of the approximate locations chosen for analysis.

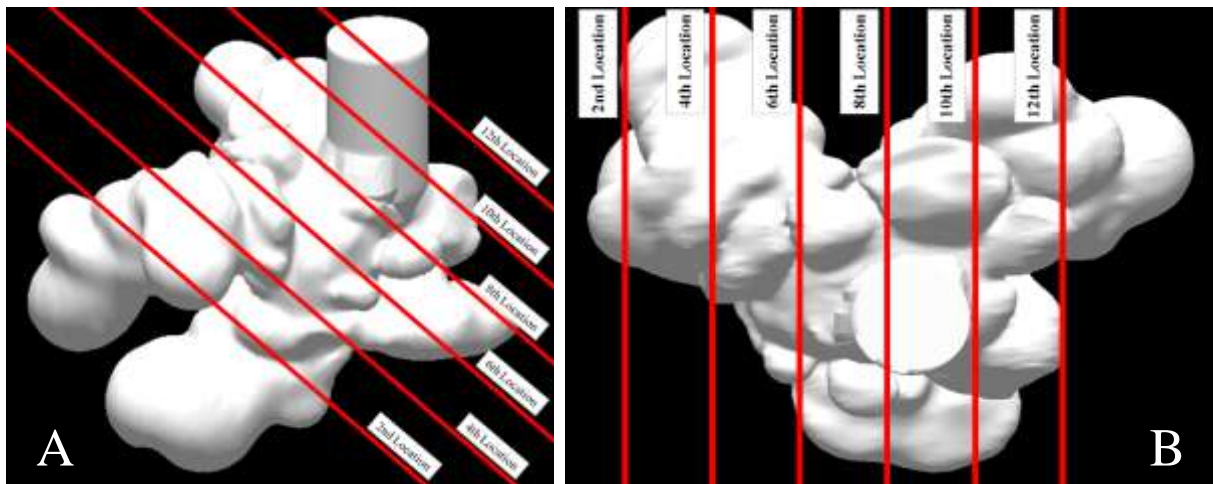


Figure 6.1 - (A) Isometric and (B) top views of the chosen locations for data analysis for the healthy human model.

6.1.1 – Locations of Potential Recirculation

When collecting stereoPIV data, care was taken in choosing which laser sheet planes to analyze.

Regions where recirculation would be most likely to occur were desired. According to literature, flow rate ratios (ratio of the alveolar to duct flow rate) approximately below 0.05 produce recirculating flows (Tippe and Tsuda 2000; Tsuda et al. 1995; Kumar et al. 2009b). These small ratios exist where the ductal flow is large compared to the alveolar flow, or in regions where the alveolar mouth diameter is small compared to the alveolar depth. It was clear from observation that there was no overwhelming flow directly adjacent to the mouth diameter of the alveoli. All of

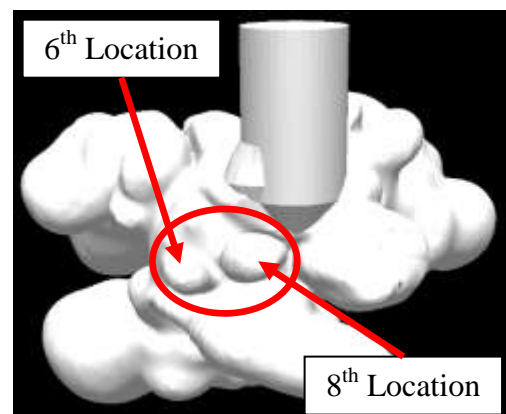


Figure 6.2 - Regions where recirculation would be most likely to occur.

the flow traveled into the alveoli with the contours of the model, essentially yielding an infinite alveolar to ductal flow ratio. Therefore, we focused on the geometry differences in this study rather than the flow rate ratios.

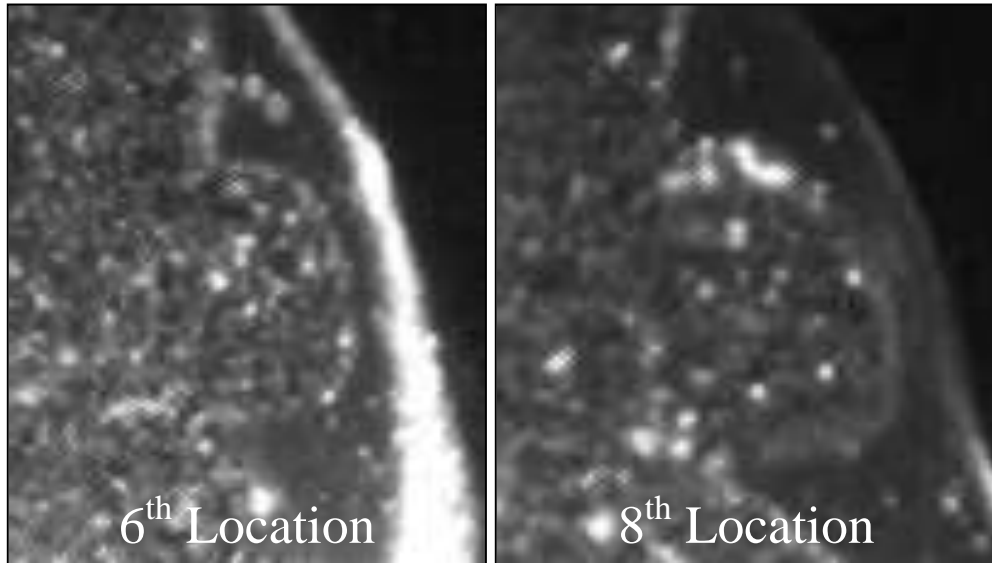


Figure 6.3 - Raw PIV images (showing the distribution of particles) of the 6th and 8th locations representing regions where recirculation would occur.

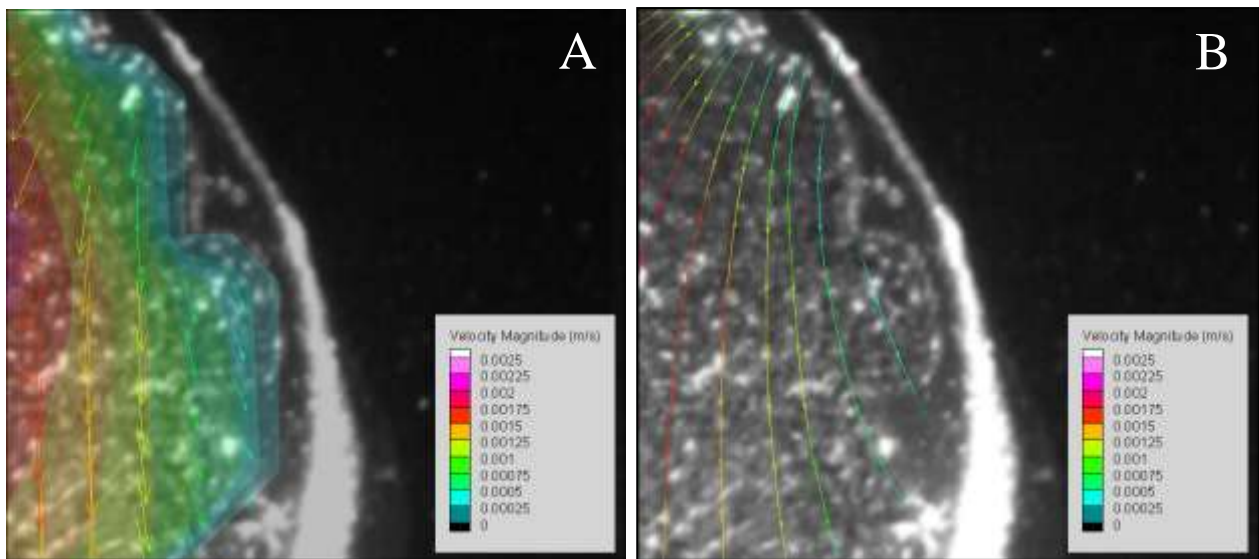


Figure 6.4 - Zoomed in views of the (A) vector and (B) streamline plots (contoured by velocity magnitude) for the 6th location in the healthy human model (refer to Figure 6.1 for the 6th location with respect to the whole model).

Of the data collected from the fourteen laser plane locations in the healthy model, the 6th and 8th locations displayed geometry that would be most likely to induce recirculation. Figure 6.2

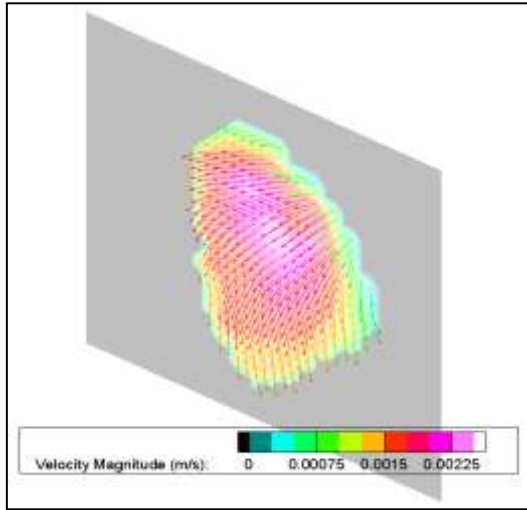


Figure 6.5 - Isometric view of the 6th location illustrating the z vectors.

illustrate the regions in the healthy model where recirculating eddies would be most likely to occur.

Figure 6.3 represents the raw PIV images illustrating particle dispersion of the two locations seen in Figure 6.2. The circular regions display the small pouches that would most likely induce recirculation. The following results first reveal the flow fields that exist at these two particular locations and conclude whether recirculating or reversible flow is occurring. Figure 6.4 represents the velocity and streamline plots for the potential recirculation region at the 6th location

(Figure 6.3). It is seen that reversible flow is present throughout the entire model, and a maximum experimental fluid velocity magnitude of 2.5 mm/s occurs near the center of the region. Reversible flow is concluded because the streamlines do not exhibit any eddy pattern. The lines go into the model in a very uniform manner without sharp direction changes. Figure 6.5 represents an isometric view of the 6th location vectors (contoured by velocity magnitude), illustrating the z-direction (third-dimension) vectors.

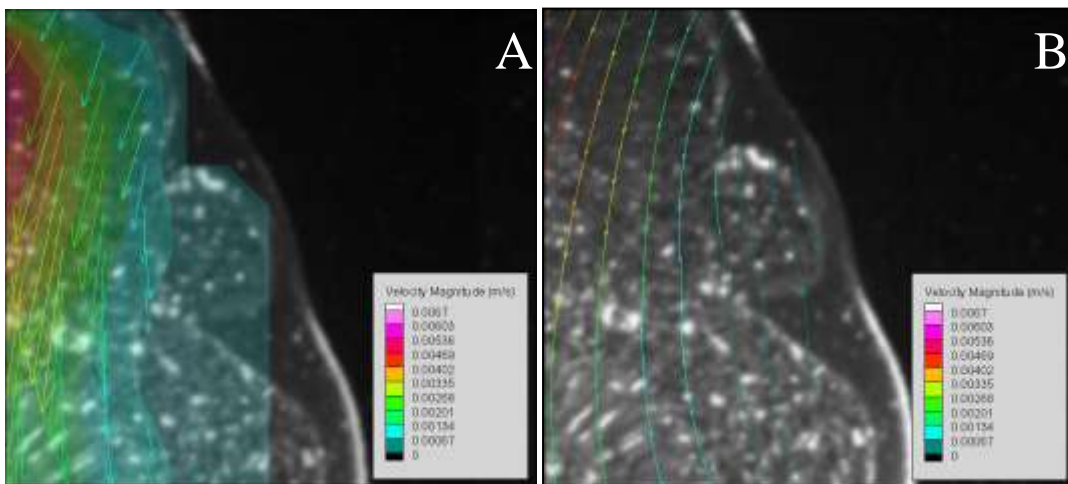


Figure 6.6 - Zoomed in views of the (A) vector and (B) streamline plots (contoured by velocity magnitude) for the 8th location in the healthy human model (refer to Figure 6.1 for the 8th location with respect to the whole model).

Similar in geometry to the 6th location, the 8th location (Figure 6.3) has features that could potentially induce recirculation (small alveolar mouth diameter). Figure 6.6 represents the 2D velocity field and streamline plots occurring in the 8th location of the healthy human model (both contoured by velocity magnitude). Reversible flow is also found in this location because the streamlines are uniform and follow the contours of the model boundary (no sharp changes in vector direction). The maximum velocity magnitude occurring at this 8th location is 6.7 mm/s. This is larger than the 6th location velocity because the 8th location is closer to the inlet of the model. Figure 6.7 represents an isometric view of the velocity vectors occurring at the 8th location (contoured by velocity magnitude), illustrating the z-component of velocity.

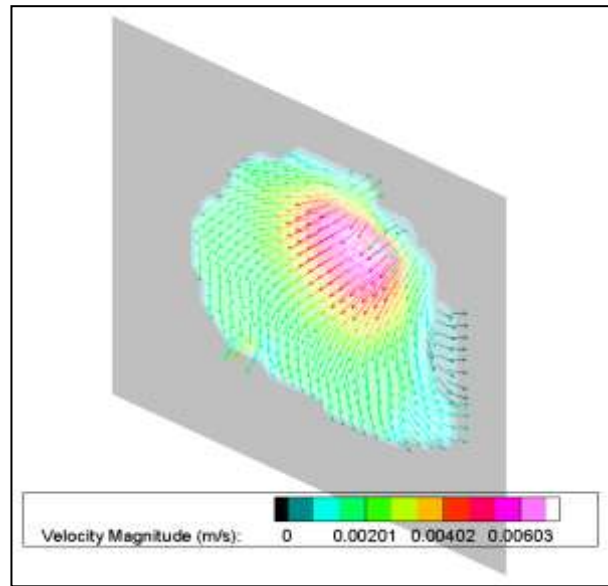


Figure 6.7 - Isometric view of the 8th location illustrating the z vectors.

6.1.2 – 3-Dimensional Flow Fields

Of the three sets of data collected for each laser location, the second set was chosen to display because of the consistency of the results. Variability existing in the three sets is discussed in section 5.2.5. Figure 6.8 represents the 2D vector results for the second set location analyzed in Figure 6.1A. In order to maximize the resolution of the velocity fields in Figure 6.8, the contours were scaled independently for each laser sheet location. It is seen that as the planar location moves closer to the inlet of the model (between locations 8 and 10), the velocities maximize. Based on the constant inlet flow rate applied to the model, the maximum experimental velocity occurring in the plane of the inlet is 38.6 mm/sec (1.94 mL/sec flow rate with an 8.0 mm duct diameter).

To visualize the three-dimensional results of the healthy human model, Figure 6.9 represents all six planar locations analyzed with contours of the global velocity magnitude to illustrate the overall range of velocities that exist within the model. Figure 6.10 displays the same six locations but from an exploded view, illustrating both contours and velocity vectors.

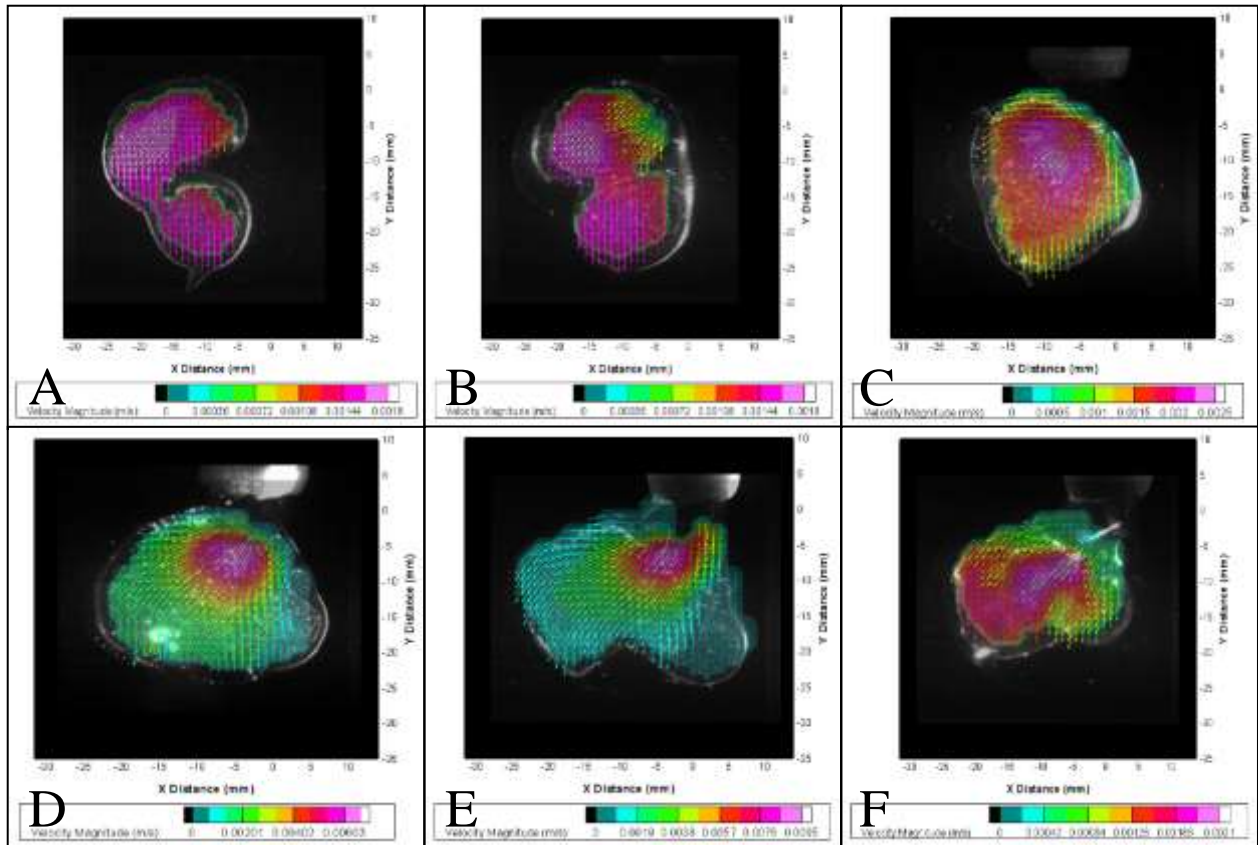


Figure 6.8 - 2D experimental velocity vector results for the six analyzed locations (A – F) corresponding to the 2nd through the 12th locations (see Figure 6.1A for locations). Each image is contoured by velocity magnitude and is independent of each location.

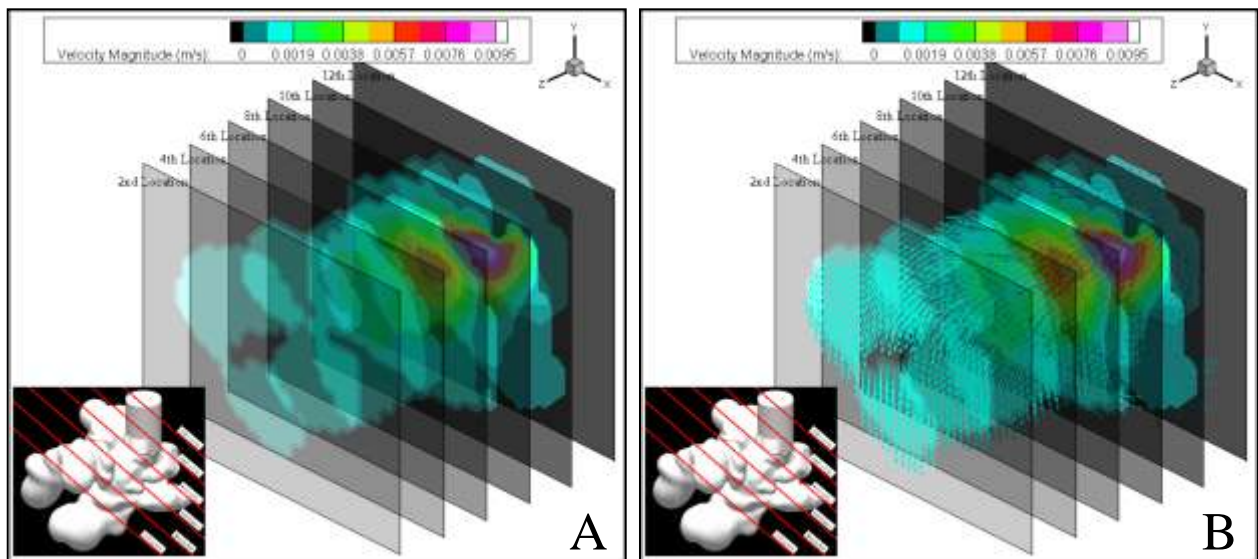


Figure 6.9 - All six planar locations analyzed showing (A) contours and (B) vectors contoured by the global velocity magnitude.

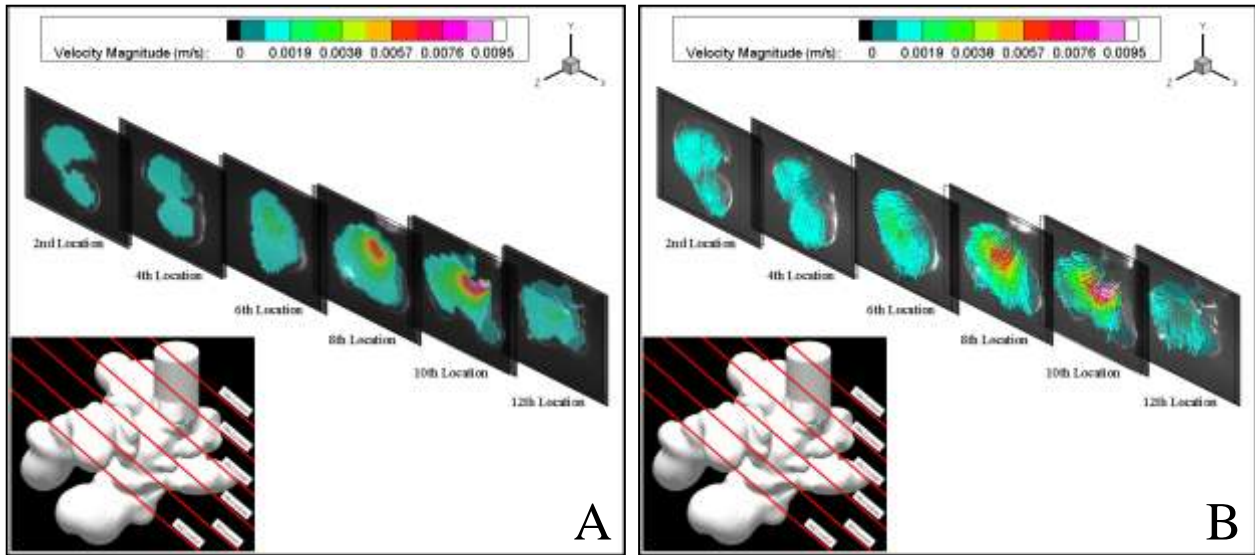


Figure 6.10 - Exploded view of all six planar locations analyzed showing (A) contours and (B) vectors contoured by the global velocity magnitude. (The maximum velocity that occurred in the planes analyzed was 9.5 mm/sec).

Finally, Figure 6.11 displays the top view of the healthy human model results representing the magnitude and direction of the z-component of velocity.

It was shown in Chapter 5 that the experimental z-component of velocity varied the most from the predicted CFD results. Therefore, the z-component vectors shown in Figure 6.11 are estimates to the behavior of the flow field occurring in the z-direction.

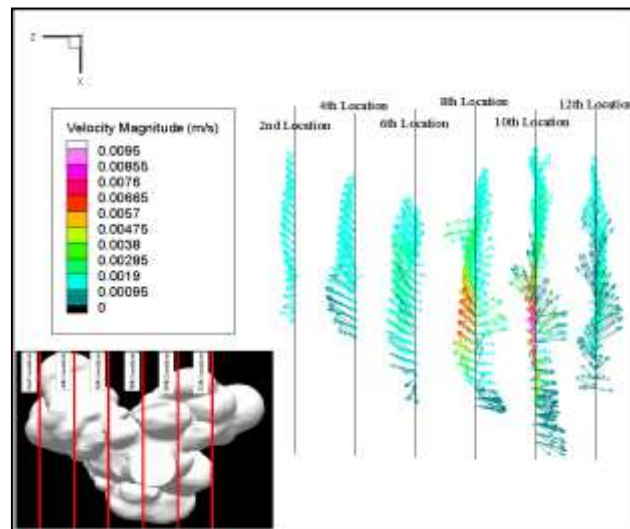


Figure 6.11 - Top view of the healthy human model representing the magnitude and direction of the z-component of velocity.

6.2 – In Vivo Healthy Human Predictions

6.2.1 – Scaling Experimental Healthy Results to In Vivo

After all of the experimental data was collected, the results were scaled back to represent velocity predictions. The shapes of the flow fields remained the same, but the overall magnitudes were affected. The velocities were scaled using the assumption that the *in vivo* conditions were well represented experimentally (Chapter 3). Therefore, the non-dimensional velocities, u^* , can be equated by

$$u_{in vivo}^* = u_{exp}^* \quad (6.1)$$

The *in vivo* velocities were predicted using Equation 6.1 by substitution of the non-dimensional parameters that were used to derive the Navier-Stokes equations in non-dimensional form (Equation 3.1). Specifically, $u = u^* U$ (where U represents the time and spatially averaged velocity at the model inlet), such that Equation 6.1 becomes

$$u_{in vivo} = u_{exp} \left[\frac{U_{in vivo}}{U_{exp}} \right] \quad (6.2)$$

where

$$u_{in vivo} = u_{exp} \left[\frac{\frac{Re_{in vivo} v_{in vivo}}{d_{in vivo}}}{\frac{Re_{exp} v_{exp}}{d_{exp}}} \right] \quad (6.3)$$

which can be used to determine the predicted *in vivo* velocities from the experimental stereoPIV measurements.

The *in vivo* and experimental model properties and flow conditions for the healthy human model are shown in Table 6.1 and Table 6.2, respectively. The Reynolds numbers for normal and

heavy *in vivo* breathing were calculated to be 0.009 and 0.035, respectively. Using the material properties for *in vivo* and experimental conditions, the experimental velocities were multiplied by 0.02469 (Equation 6.3) to achieve the *in vivo* flow field for a Re of 0.009 and multiplied by 0.09341 to represent the *in vivo* field for a Re of 0.035.

Table 6.1 - Model and material properties for the healthy human model.

Symbol	Property	<i>In Vivo</i> (Air at 20°C)	Experimental (Glycerin at 20°C)
d	Acinus Inner Duct Diameter (mm)	0.41	8.00
V_i	Mean Acinus Volume (mm ³)	1.25	9013.46
ν	Kinematic Viscosity (mm ² /sec)	17.10	909.80

Table 6.2 - *In vivo* and experimental flow conditions for the healthy human model.

		Time Averaged Re at Model Inlet	Expansion (%)	Breathing Frequency (breaths/min)	Time Average Flow Rate at Model Inlet (mL/sec)	U, Time and Spatially Averaged Velocity at Model Inlet (mm/sec)
<i>In Vivo</i>	Normal Breathing	0.009	16	15.7	1.30E-04	0.97
	Heavy Breathing	0.035	60	15.7	4.91E-04	3.66
Experimental	Used in This Work	0.138	35	15.0	1.94	38.60

Referring to section 2.4, an inlet duct was created for the healthy human model. The cylindrical geometry was added using arbitrary dimensions and created to fit with the surrounding model

contours. When the final model was scaled back to *in vivo* dimensions, the model was scaled based on dimensions of alveoli rather than the arbitrary duct diameter (see Figure 2.16 for the dimensions used for scaling to *in vivo* sizes). Therefore, the ratio of the experimental diameter to the *in vivo* duct diameter was 19.4 for the healthy model. Regardless of the dimensions used to create the inlet duct, the ratio between any distance for the experimental and *in vivo* models will always be the scaling factor used (if uniform scaling by length is applied to the entire model). Because the experimental healthy model was created 19.4x *in vivo* size, the x, y, and z distances were divided by 19.4 to represent the correct scaled *in vivo* dimensions of the model.

Figure 6.12 represents the scaled *in vivo* 2D results for all six of the locations analyzed for an *in vivo* Re of 0.009. Each image is contoured by *in vivo* velocity magnitude and is independent from each location.

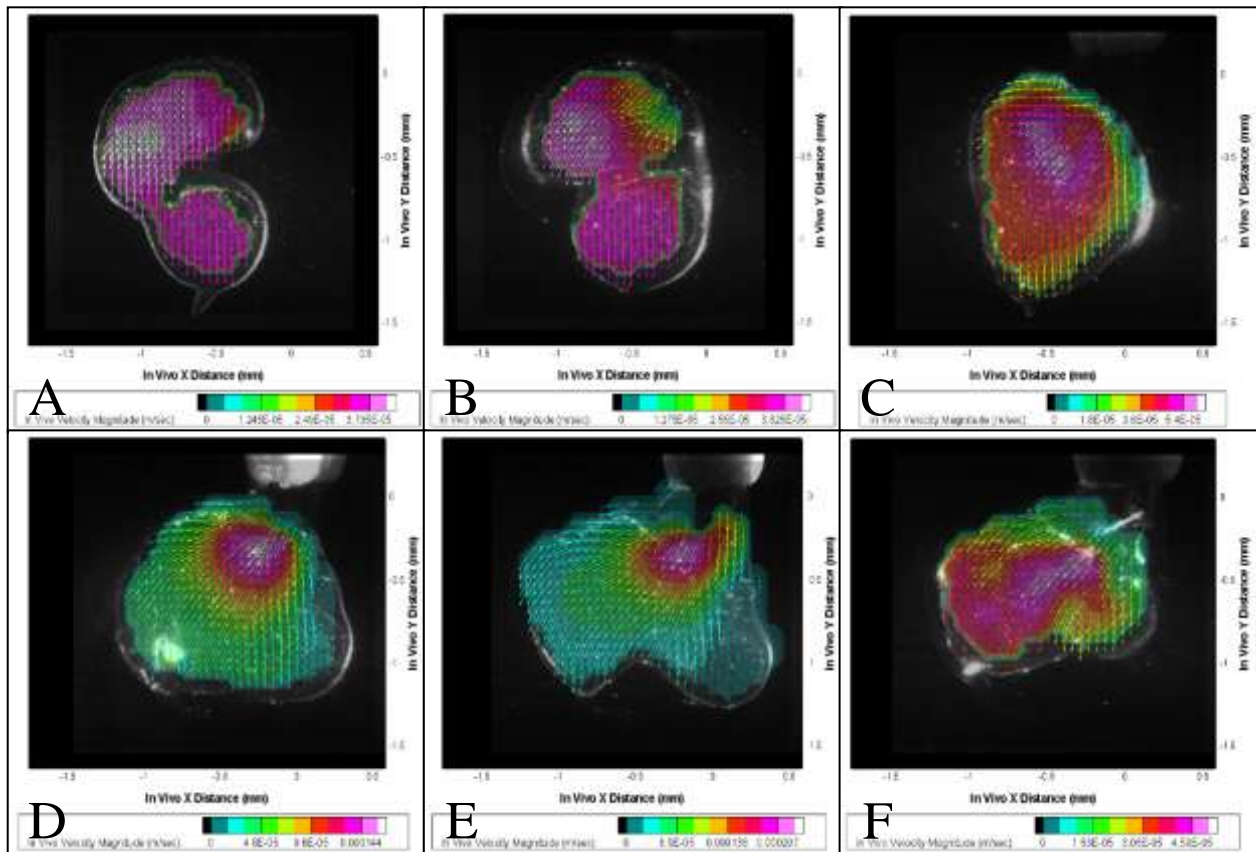


Figure 6.12 - 2D *in vivo* velocity vector results for the six analyzed locations (A – F) corresponding to the 2nd through the 12th locations (see Figure 6.1A for locations) for Re = 0.009.

Figure 6.13 illustrates the *in vivo* flow fields (for a Re of 0.009) for all six planar locations analyzed contoured by the global *in vivo* velocity magnitude, while Figure 6.14 illustrates the exploded view of all six locations.

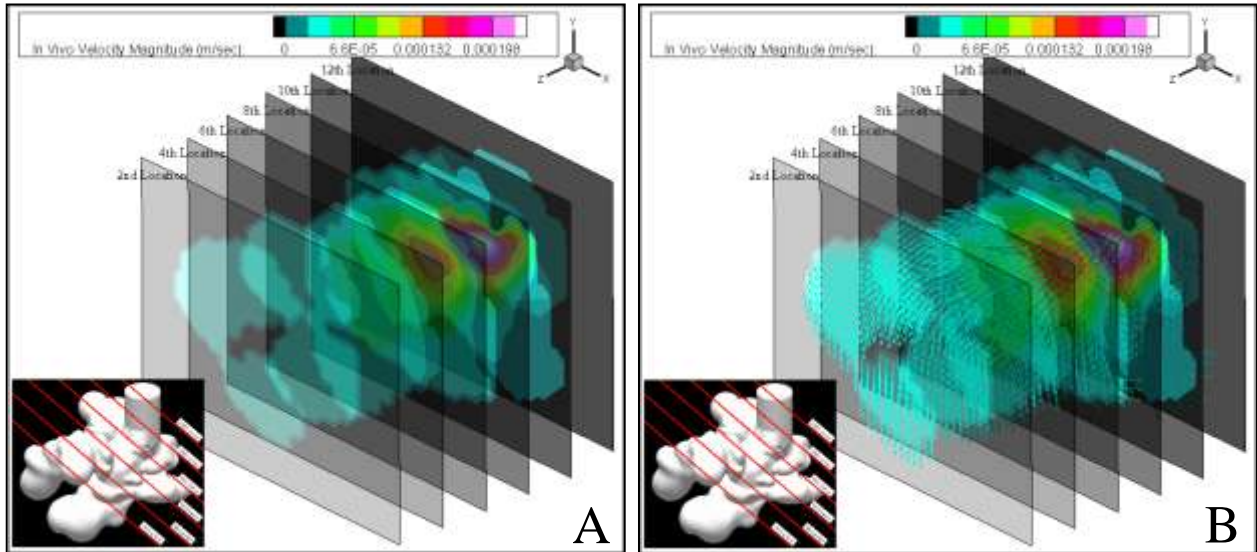


Figure 6.13 - In vivo results for all six planar locations analyzed showing (A) contours and (B) vectors contoured by the global velocity magnitude for Re = 0.009. (The maximum velocity that occurred in the planes analyzed was 0.22 mm/sec)

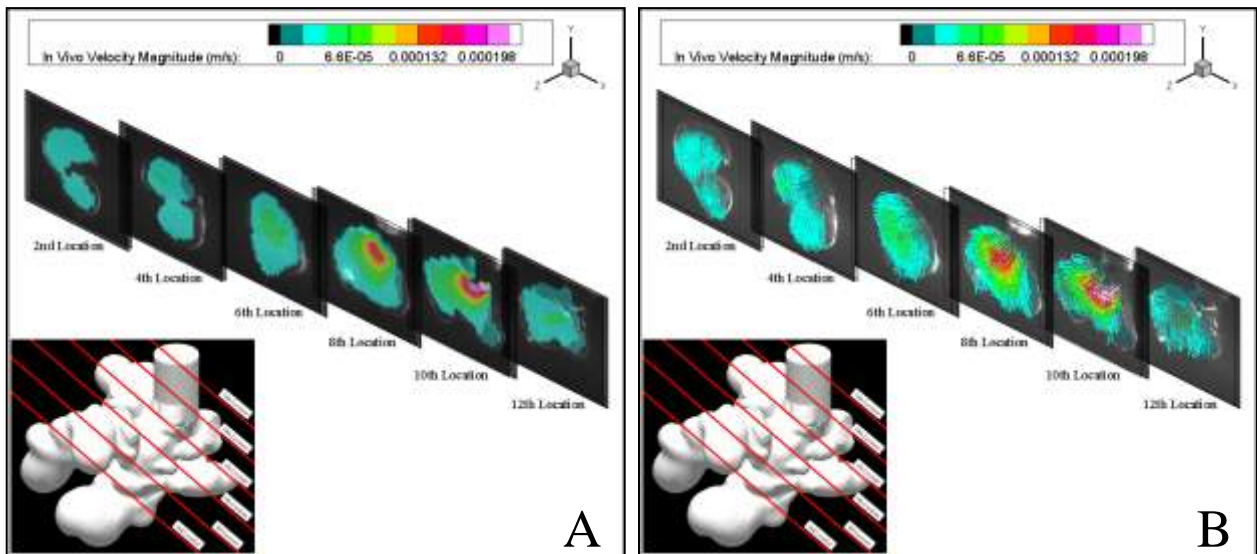


Figure 6.14 - Exploded view of all six planar locations analyzed showing (A) contours and (B) vectors contoured by the in vivo global velocity magnitude for a Re = 0.009. (The maximum velocity that occurred in the planes analyzed was 0.22 mm/sec)

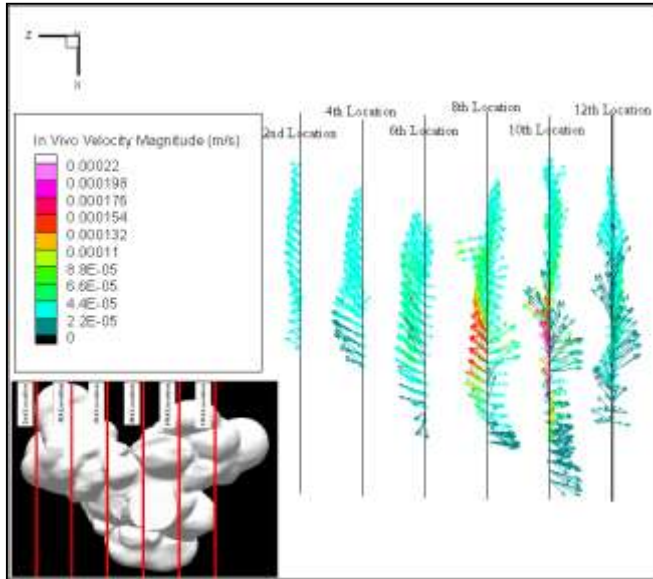


Figure 6.15 - Top view of the healthy human model representing the *in vivo* magnitude and direction of the z-component of velocity (for $Re = 0.009$).

Finally, Figure 6.15 illustrates the top view of the healthy human model *in vivo* results representing the magnitude and direction of the z-component of velocity for a Re of 0.009. Figure 6.16 represents the scaled *in vivo* 2D results for all six of the locations analyzed for an *in vivo* Re of 0.035. Each image is contoured by *in vivo* velocity magnitude and is independent from each location. Figure 6.17 illustrates the healthy *in vivo* flow fields (for a Re of 0.035) for all six planar locations analyzed contoured by the global *in vivo* velocity magnitude, while

Figure 6.18 illustrates the exploded view of all six locations.

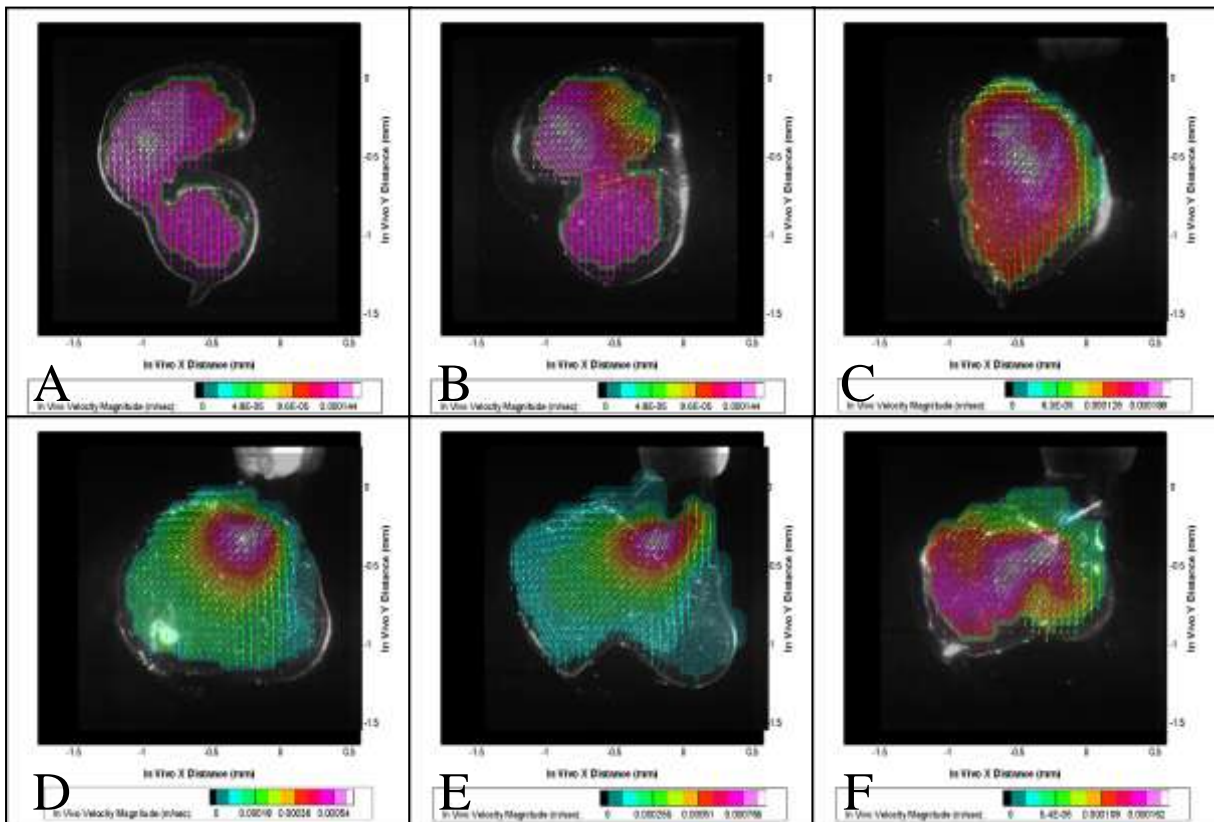


Figure 6.16 - 2D *in vivo* velocity vector results for the six analyzed locations (A – F) corresponding to the 2nd through the 12th locations (see Figure 6.1.A for locations) for $Re = 0.035$.

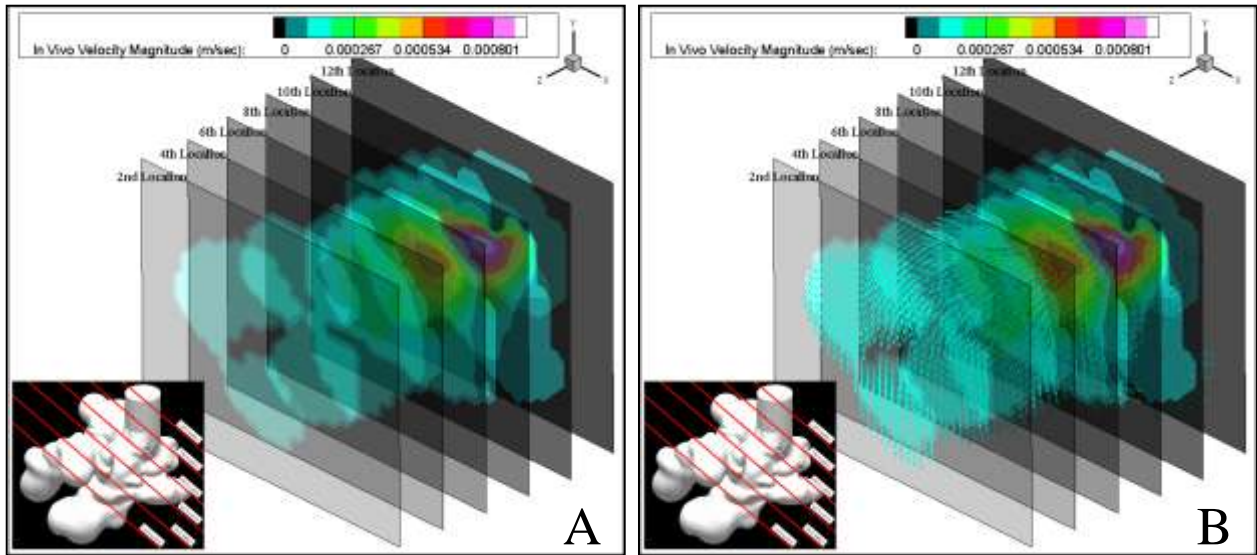


Figure 6.17 - In vivo results for all six planar locations analyzed showing (A) contours and (B) vectors contoured by the global velocity magnitude for $Re = 0.035$. (The maximum velocity that occurred in the planes analyzed was 0.89 mm/sec)

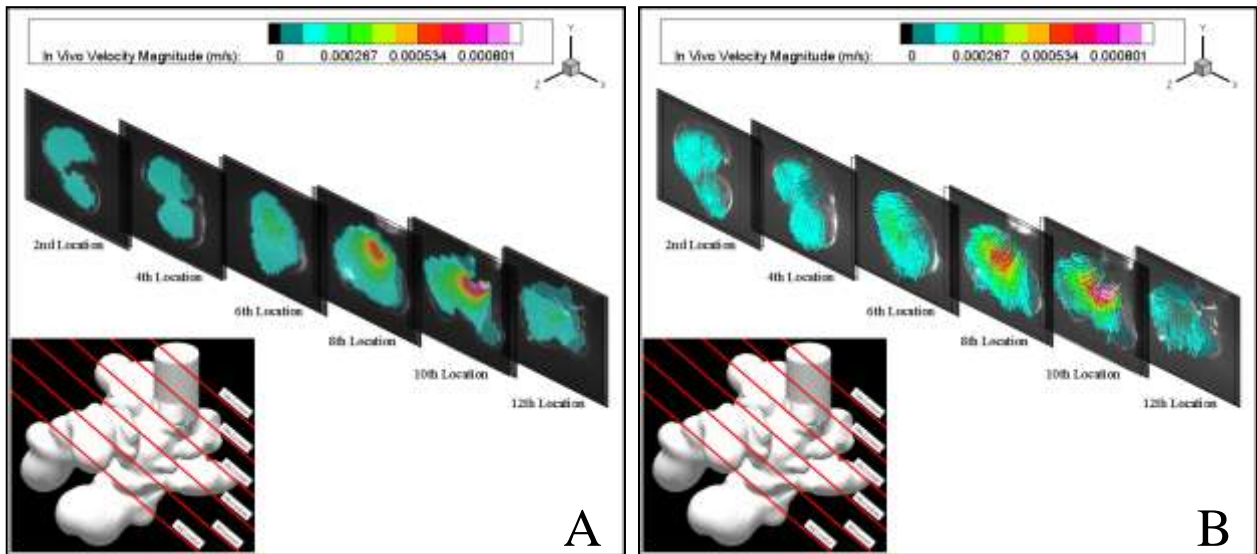


Figure 6.18 - Exploded view of all six planar locations analyzed showing (A) contours and (B) vectors contoured by the in vivo global velocity magnitude for a $Re = 0.035$. (The maximum velocity that occurred in the planes analyzed was 0.89 mm/sec)

Finally, Figure 6.19 illustrates the top view of the healthy model representing the *in vivo* velocity magnitude and direction of the z-component of velocity for an *in vivo* Re of 0.035.

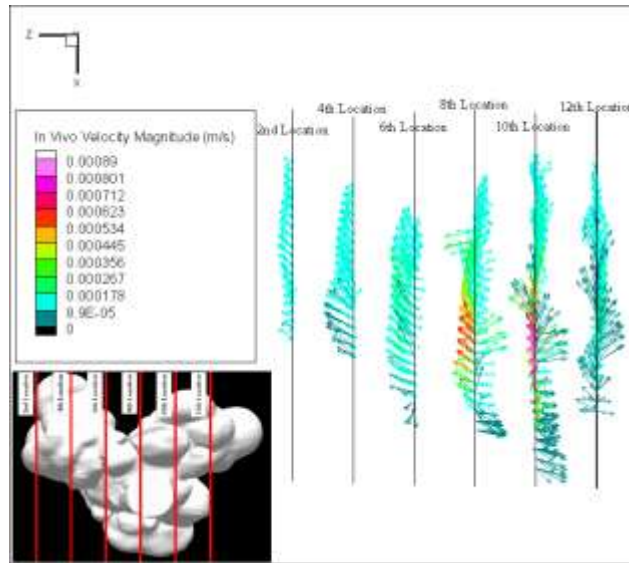


Figure 6.19 - Top view of the healthy human model representing the in vivo magnitude and direction of the z-component of velocity (for $Re = 0.035$).

6.3 – Experimental Emphysemic Human Model

A total of thirty-six data sets were collected for the emphysemic human model; three sets of data for twelve laser plane locations. In order to illustrate the three-dimensional effect of all of the results, five locations were analyzed and compared. Figure 6.20 represents the isometric and top views of the approximate locations chosen for analysis.

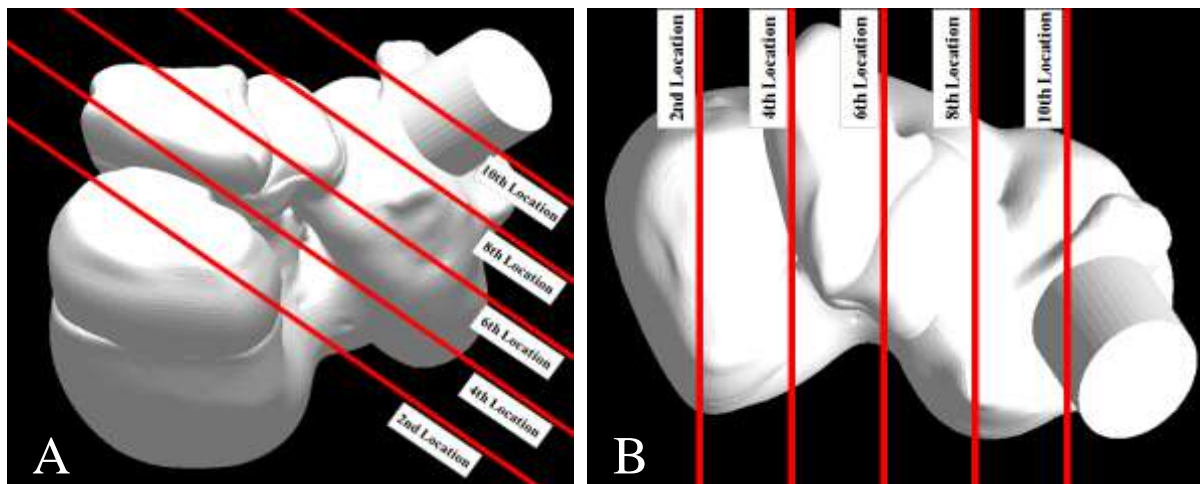


Figure 6.20 - (A) Isometric and (B) top views of the chosen locations for data analysis for the emphysemic human model.

Because of the oversized geometry, as compared to the healthy model, there were no specific regions that would suggest recirculation. No regions existed where the alveolar mouth diameter was smaller than the alveolar depth. Therefore, the results from the entire emphysemic model were presented, similar to section 6.1.2 above. Of the three sets of data collected for each location, the third set was chosen to display because of the consistency of the results. The variability occurring between the three sets is discussed in section 5.2.5. Figure 6.21 represents the 2D vector results for all third set locations analyzed in Figure 6.20A.

To visualize the three-dimensional results of the emphysemic human model, Figure 6.22 illustrates all five planar locations analyzed with contours of the global velocity magnitude.

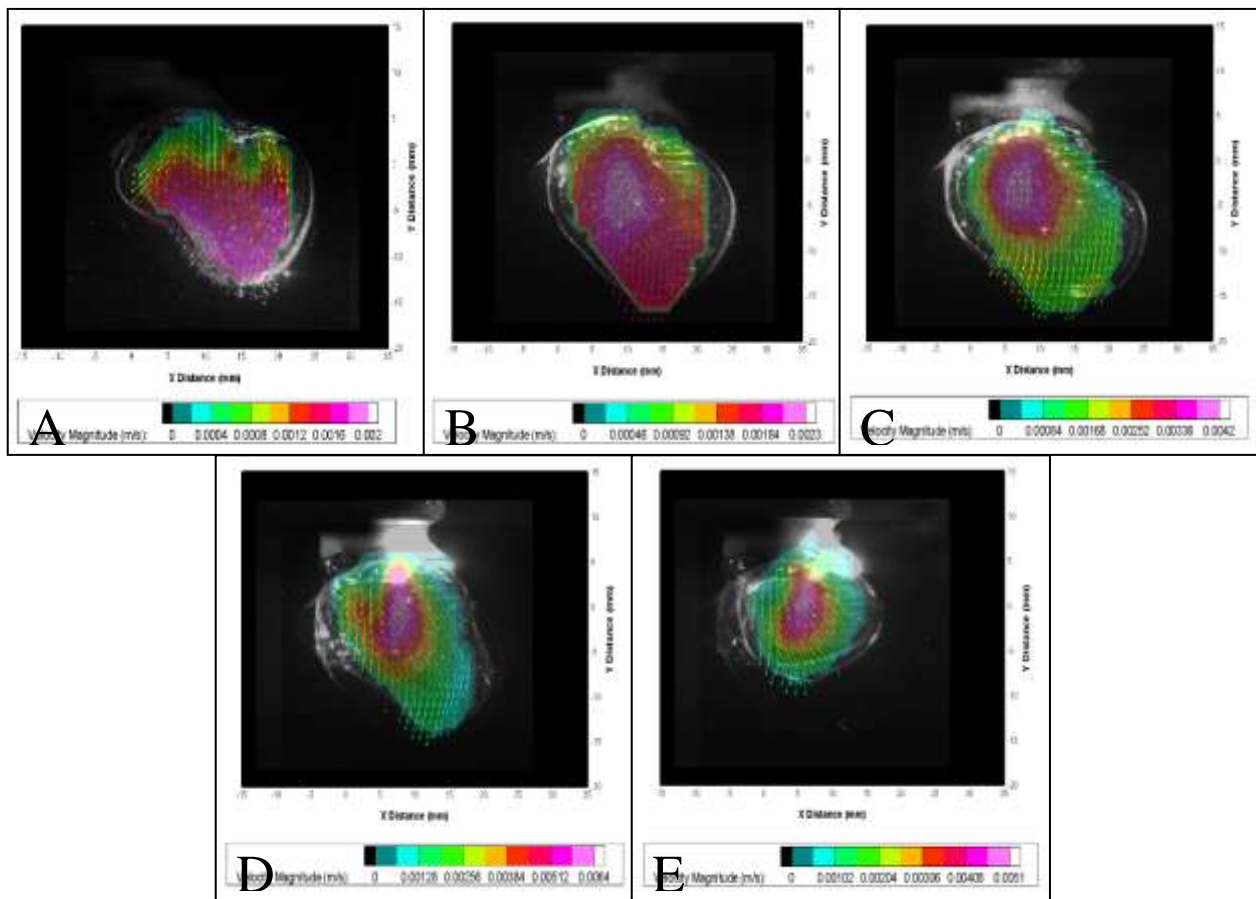


Figure 6.21 - 2D velocity vector results for the five analyzed locations (A – E) corresponding to the 2nd through the 10th locations (see Figure 6.20A for locations). Each image is contoured by velocity magnitude and is independent of each location.

Figure 6.23 displays the same five locations but from an exploded view, illustrating both contours and velocity vectors. Finally, Figure 6.24 displays the top view of the emphysemic human model results representing the magnitude and direction of the z-component of velocity.

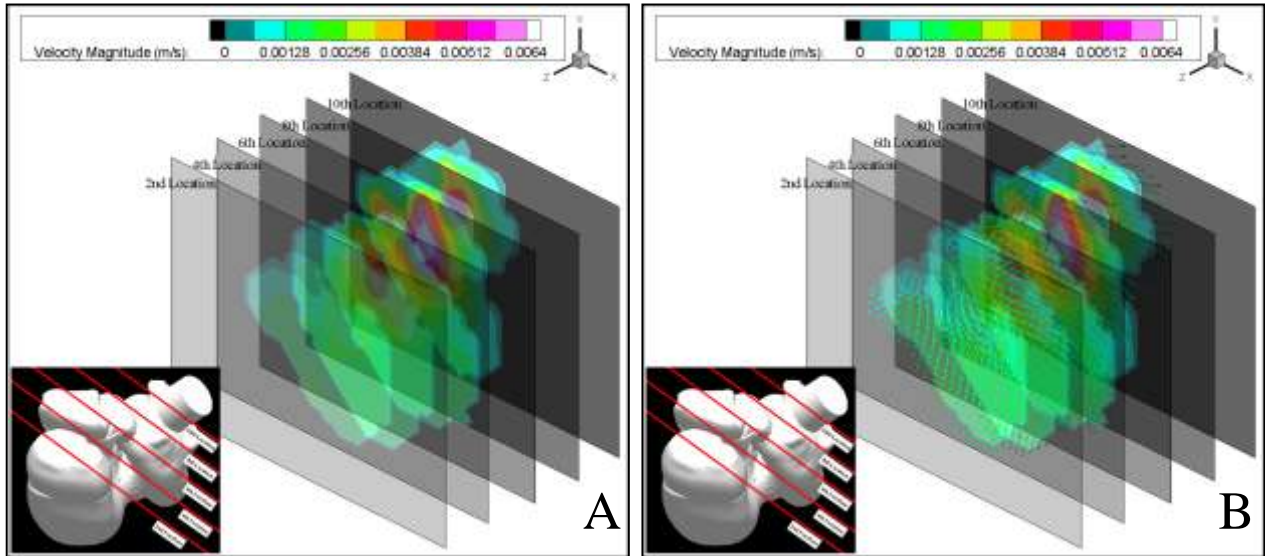


Figure 6.22 - All five planar locations analyzed showing (A) contours and (B) vectors contoured by the global velocity magnitude. (The maximum velocity that occurred in the planes analyzed was 6.4 mm/sec)

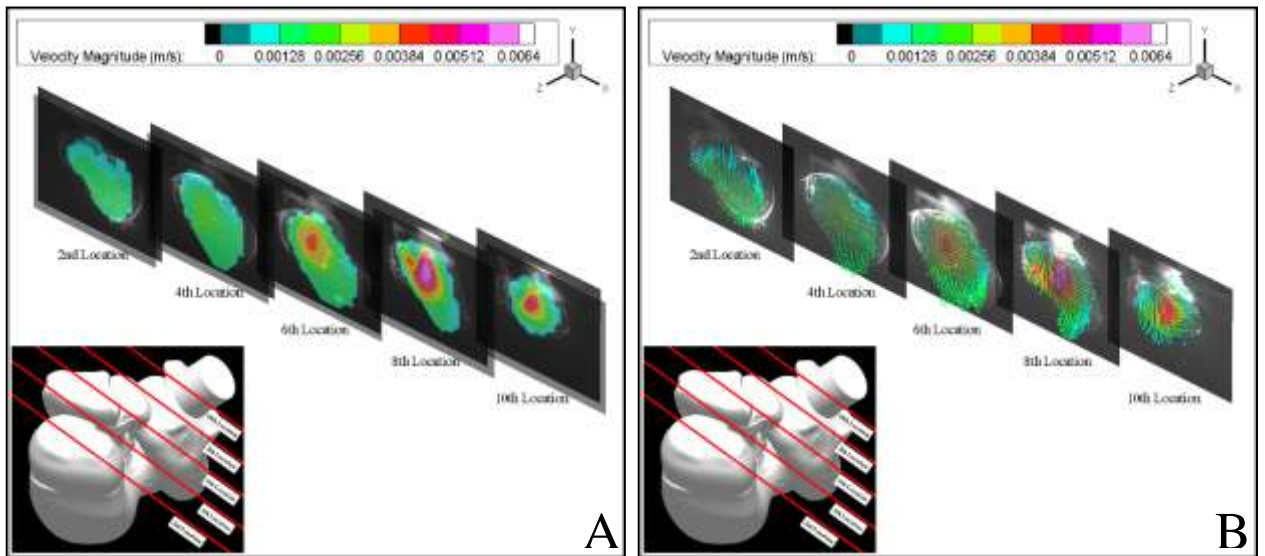


Figure 6.23 - Exploded view of all five planar locations analyzed showing (A) contours and (B) vectors contoured by the global velocity magnitude. (The maximum velocity that occurred in the planes analyzed was 6.4 mm/sec)

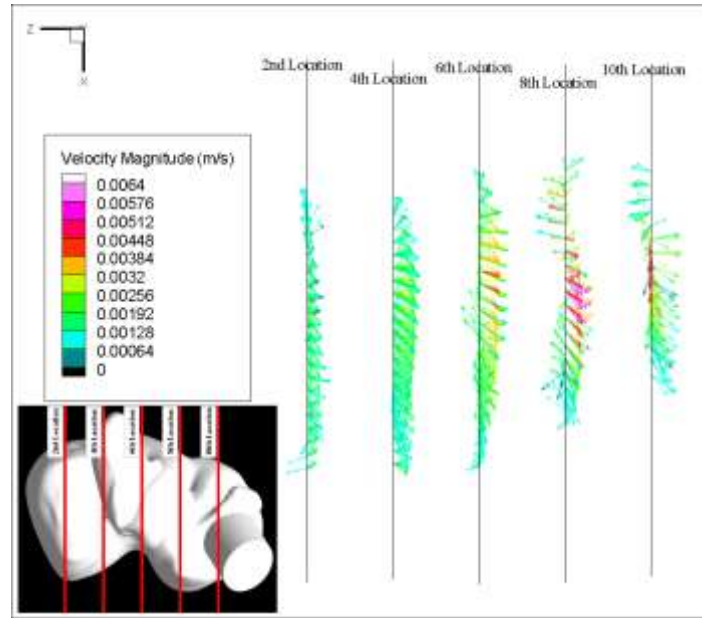


Figure 6.24 - Top view of the emphysema human model representing the magnitude and direction of the z-component of velocity.

6.4 – *In Vivo* Emphysemic Human Predictions

6.4.1 – Scaling Experimental Emphysemic Results to *In Vivo*

Because the emphysemic model was 8.9x *in vivo* size (by length scale), the x, y, and z distances were divided by 8.9 to represent the scaled *in vivo* dimensions of the model. Similar to the healthy model, the experimental emphysemic velocities were scaled using Equation 6.3 and the model properties in Table 6.3. Table 6.4 represents the *in vivo* and experimental flow conditions for the emphysemic model. The Reynolds number for normal *in vivo* emphysemic breathing was calculated to be 0.035. Using the material properties for *in vivo* and experimental conditions, the experimental velocities were multiplied by 0.04204 (Equation 6.3) to achieve the *in vivo* flow fields for an emphysemic Re of 0.035. This is smaller than the conversion used for the healthy Re of 0.035 because the emphysemic *in vivo* diameter is 2x larger than the healthy. Therefore, even though the Re are the same, the conversions vary because of the model properties.

Table 6.3 - Model and material properties for the emphysemic human model.

Symbol	Property	<i>In Vivo</i> (Air at 20°C)	Experimental (Glycerin at 20°C)
d	Acinus Inner Duct Diameter (mm)	0.90	8.00
V_i	Mean Acinus Volume (mm ³)	14.39	10488.60
ν	Kinematic Viscosity (mm ² /sec)	17.10	909.80

Table 6.4 - *In vivo* and experimental flow conditions for the emphysemic human model.

		Time Averaged Re at Model Inlet	Expansion (%)	BF (breaths/min)	Time Average Flow Rate at Model Inlet (mL/sec)	U, Time and Spatially Averaged Velocity at Model Inlet (mm/sec)
<i>In Vivo</i>	Normal Breathing	0.035	11	16.0	1.03E-03	1.61
Experimental	Used in This Work	0.138	30	15.0	1.94	38.60

Figure 6.25 represents the scaled *in vivo* 2D results for all five of the locations analyzed for an emphysemic *in vivo* Re of 0.035. Each image is contoured by *in vivo* velocity magnitude and is independent from each location. Figure 6.26 illustrates the healthy *in vivo* flow fields (for a Re of 0.035) for all five planar locations analyzed contoured by the global *in vivo* velocity magnitude, while Figure 6.27 illustrates the exploded view of all six locations.

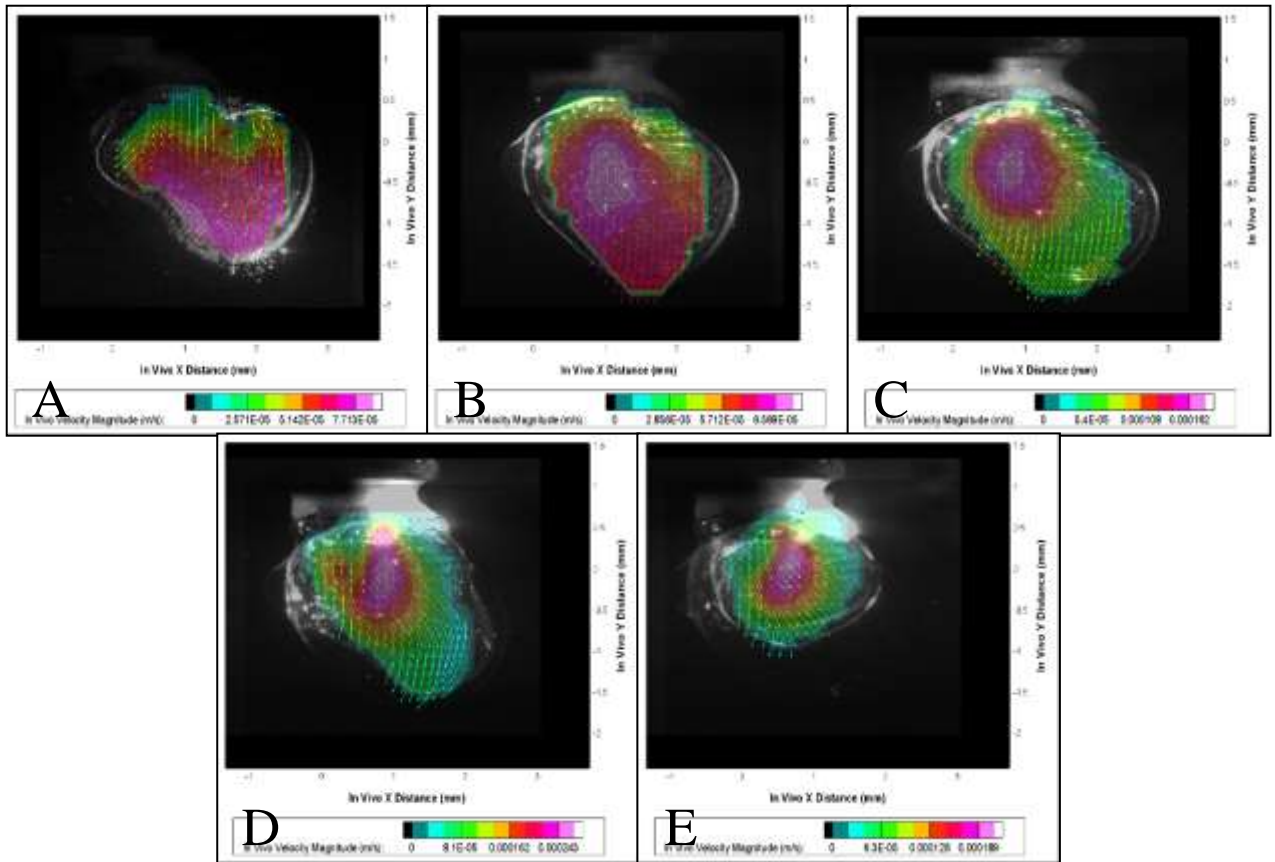


Figure 6.25 - 2D in vivo velocity vector results for the five analyzed locations (A – E) corresponding to the 2nd through the 10th locations (see Figure 6.20A for locations) for $Re = 0.035$.

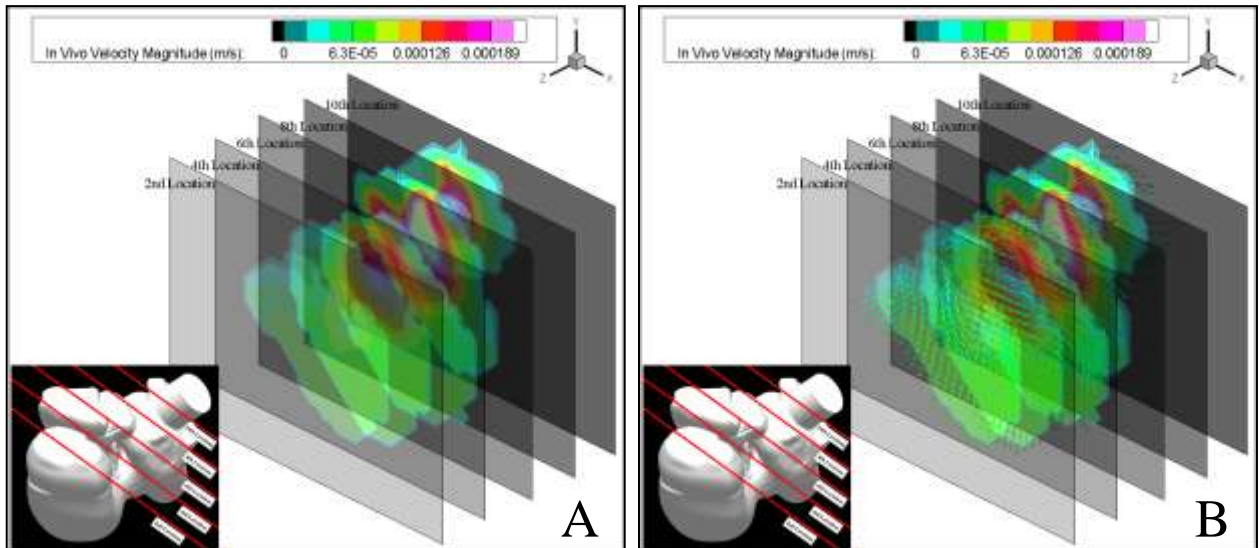


Figure 6.26 - In vivo results for all five planar locations analyzed showing (A) contours and (B) vectors contoured by the global velocity magnitude for $Re = 0.035$. (The maximum velocity that occurred in the planes analyzed was 0.21 mm/sec)

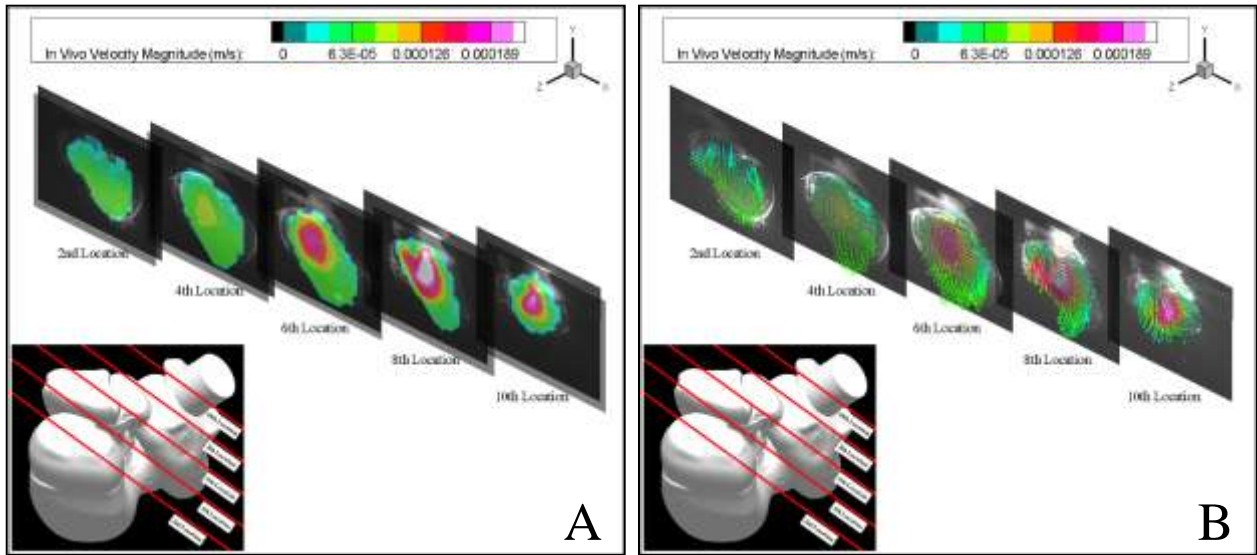


Figure 6.27 - Exploded view of all five planar locations analyzed showing (A) contours and (B) vectors contoured by the *in vivo* global velocity magnitude for a $Re = 0.035$. (The maximum velocity that occurred in the planes analyzed was 0.21 mm/sec)

Finally, Figure 6.28 illustrates the top view of the emphy model which represents the *in vivo* magnitude and direction of the a-component of velocity for an *in vivo* Re of 0.035.

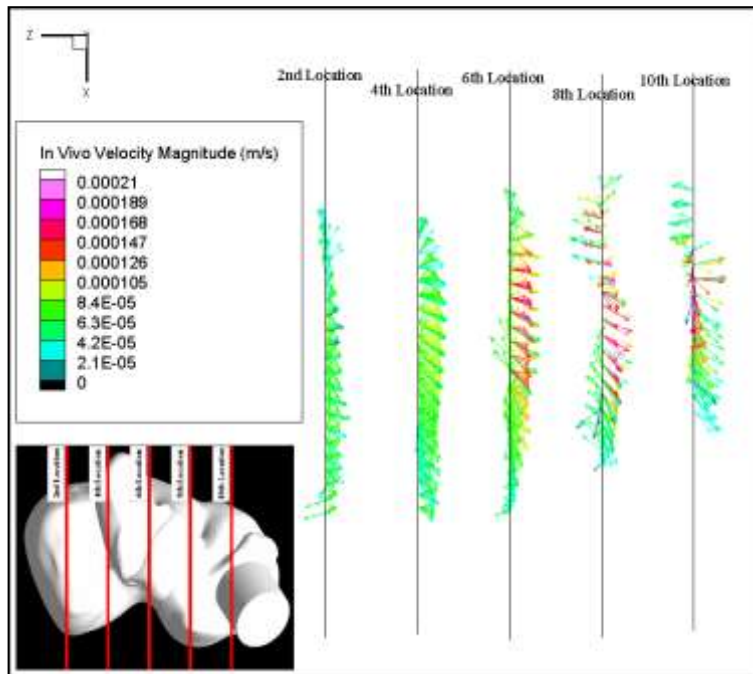


Figure 6.28 - Top view of the emphysemic human model representing the *in vivo* magnitude and direction of the z-component of velocity (for $Re = 0.035$).

6.5 – Comparison between Healthy and Emphysemic Models

The flow fields for each model (healthy model normal and heavy breathing, and emphysema model normal breathing) were obtained experimentally under dynamically similar flow conditions. Comparisons made under these conditions can only be qualitative. For example, whether or not recirculation is present can be examined on the large scale. However, the experimental results can be used to compare flow field magnitudes *in vivo* by scaling the experimental results back to *in vivo* size and breathing conditions. The following sections analyze characteristics that affect the differences that exist between the two models.

6.5.1 – Geometric Differences

Table 6.5 represents the geometrical differences that exist between the healthy and emphysemic models (for both *in vivo* and experimental cases), while Figure 6.29 illustrates the physical differences existing between the prototypes used for experimentation. A major difference existing between the two models is the presence of potential recirculation regions in the healthy model; occurring when the ductal flow is large compared to the alveolar flow (section 6.1.1). From observation, the healthy model had two such locations, but the emphysemic model did not contain geometry that would induce recirculation.

Table 6.5 - Characteristics of *in vivo* and experimental healthy and emphysemic models.

		Duct Diameter (mm)	Model Volume (mm ³)	Overall Length (mm)	Overall Width (mm)	Scaling Factor
<i>In Vivo</i> Model	Healthy	0.41	1.3	1.7	2.1	N/A
	Emphy	0.9	14.4	3.5	3.9	N/A
Experimental Model	Healthy	8.0	9013.5	33	41	19.4
	Emphy	8.0	10488.6	31	35	8.9

The majority of the emphysemic model was merged into two large sections (Figure 6.29A); none of which contained regions where the alveolar mouth diameter was small compared to the alveolar depth. The healthy model, however, contained multiple, well defined bulb structures with several distinct alveoli (Figure 6.29B).



Figure 6.29 - (A) Healthy and (B) emphysemic experimental prototypes. The circled portion represents the locations in the healthy model most

6.5.2 – Comparison of Flow Conditions

Table 6.6 represents the comparisons between the *in vivo* and emphysemic breathing conditions and corresponding flow rates and velocities. The effects of these differences are described in the following sections.

Table 6.6 - Comparison between the healthy and emphysemic breathing conditions calculated for *in vivo* and experimental cases.

		Breathing Condition	Time Averaged Re at Model Inlet	Expansion (%)	BF (breaths/min)	Time Averaged Flow Rate at Model Inlet (mL/sec)	U, Time and Spatially Averaged Velocity at Model Inlet (mm/sec)
Healthy	<i>In Vivo</i>	Normal	0.009	16	15.7	1.30E-04	0.97
		Heavy	0.035	60	15.7	4.91E-04	3.66
	Experiment	Used in This Work	0.138	35	15.0	1.94	38.60
Emphysema	<i>In Vivo</i>	Normal	0.035	11	16.0	1.03E-03	1.61
	Experiment	Used in This Work	0.138	30	15.0	1.94	38.60

6.5.3 – Normal Healthy Breathing vs. Normal Emphysemic Breathing

The flow fields shown in section 6.1.1 conclude that reversible flow is present in the regions of potential recirculation (6th and 8th locations) and throughout the entire healthy human model. Reversible flow was also concluded for all regions in the emphysemic model. Therefore, regardless of the magnitudes existing in the flow fields, both models exhibit characteristics of reversible flow. This indicates that the fluid motion replicates the motion of the outer boundary; following the contours of the model as it changes shape. In order to better understand the differences occurring between the two models, the *in vivo* normal healthy breathing (Re = 0.009) and normal emphysemic breathing (Re = 0.035) cases were compared. It is seen in Table 6.6 that the normal emphysemic *in vivo* flow rate at the model inlet is 8x larger than the flow rate seen in the normal healthy model (1.03E-3 mL/sec for normal emphysemic and 1.30E-4 mL/sec for normal healthy). The average velocity occurring in the normal healthy model, however, is approximately 1.6x larger than the emphysemic model. These differences stem from the flow conditions used for each *in vivo* model.

The average flow rate is calculated based on the derivative of the volume change curve. The change in volume for a given model is calculated based on the initial volume of the model and the desired percent expansion to occur over a known breathing period. The average velocity is then calculated by dividing the average flow rate by the cross-sectional area of the inlet duct (a function of the duct diameter squared). *In vivo* duct dimensions were used to calculate *in vivo* predictions (0.41 mm and 0.90 mm for healthy and emphysemic, respectively), while 8 mm was used for both experimental models. Therefore, the larger initial volume of the emphysemic model (11x larger than healthy) coupled with the slightly smaller percent expansion (11% for emphysemic opposed to 16% for healthy; approximately 1.5x less) results in an average flow rate that is approximately 8x that seen in the heavy healthy model (11x larger volume / 1.5x less percent expansion). The differences in average velocities are calculated based on the differences between *in vivo* duct diameters (0.90 mm for emphysemic and 0.41 mm for healthy).

Figure 6.30 represents the predicted *in vivo* flow fields occurring close to the inlet of each model, when scaling to an *in vivo* Re = 0.009 for normal healthy breathing and Re = 0.035 for normal emphysemic breathing. The difference between the maximum velocity magnitudes was

calculated to be 8% ($2.34E-4$ m/sec for normal healthy and $2.15E-4$ m/sec for normal emphysema). Even though the velocity magnitudes are similar, the distributions occurring throughout the each model vary significantly. Figure 6.30A illustrates the flow entering the healthy model at a high velocity then uniformly slowing as the fluid moves towards the outer walls. The emphysemic model (Figure 6.30B), however, yields a large region of fast flow near the inlet that begins to slow at non-uniform intervals.

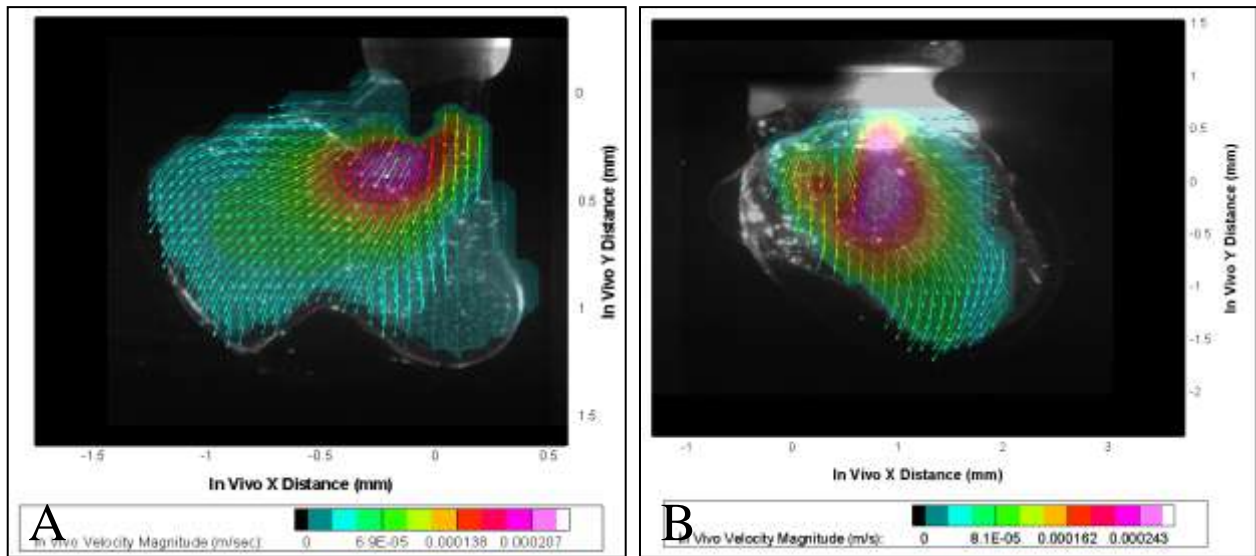


Figure 6.30 - (A) 10th location in the normal healthy human model ($Re = 0.009$) and the (B) 8th location of the normal emphysemic model ($Re = 0.035$).

To further compare the differences existing in the normal healthy breathing and emphysemic conditions, the locations furthest from the inlet were analyzed representing the 2nd location for both models (Figure 6.31). The difference between the maximum velocity magnitudes at the 2nd location is approximately 66% ($4.34E-5$ m/sec for normal healthy and $8.57E-5$ m/sec for normal emphysema). The distribution occurring throughout the contours of the model vary between the different geometries at this location. It is seen that the healthy model exhibits a very uniform flow field distribution with the magnitudes decreasing from the center of the model out towards the wall. The emphysemic geometry, however, illustrates a non-uniform spread with the largest magnitude occurring close to the outer wall near the bottom of the model (furthest distance from the inlet of the model).

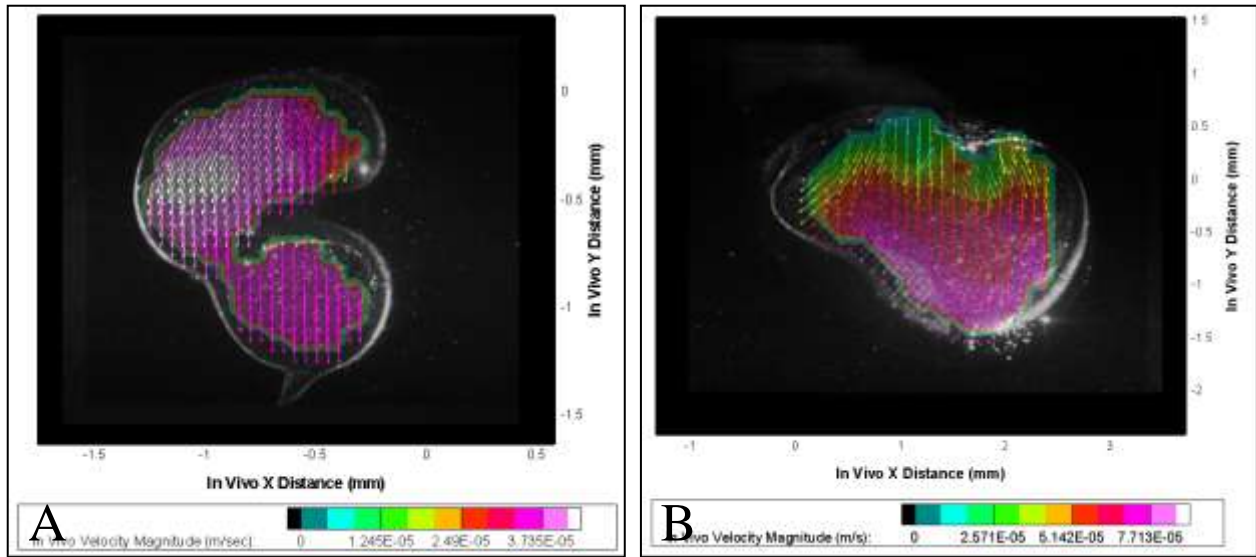


Figure 6.31 - 2nd location in the (A) normal healthy human model ($Re = 0.009$) and the (B) normal emphysemic model ($Re = 0.035$).

Based on the *in vivo* breathing conditions and initial model volumes, the normal emphysemic breathing model inhales 1.6 mm^3 versus 0.2 mm^3 for the normal healthy breathing model (a total of 8x more fluid). This is an indication that particles traveling in the emphysemic model would travel deeper into the model than those in the healthy model by convection. This result is interesting since the diffusion capacity of the lung decreases in emphysema (Park et al. 1970), so higher ventilation rates could be a way for the emphysemic lung to compensate. However, particles are not able to deposit on the alveolar walls by this method of transport alone. The overall size of the emphysemic model is significantly larger (11x) than the healthy model. Therefore, even though the initial traveling distance of a particle occurring in the emphysemic model may be longer due to convection, the outer bounds of the emphysemic model are much further away with respect to the finishing location of a particle. Based on this final distance needed to travel by diffusion prior to depositing (distance from the end of a pathline to the nearest wall), it is concluded that particles would have a higher tendency to deposit in the healthy model rather than the emphysemic model because the walls are much closer to the ends of particle pathlines. Residence time (the amount of time that a particle has to diffuse) plays little to no role in the overall diffusion occurring in each of these models because the *in vivo* breathing frequencies are similar (15.7 breaths/min for healthy and 16.0 breaths/min for emphysema). If a significant difference were present (a frequency of 30 breaths/min for the healthy model, for

example), particles might not have time to diffuse to the adjacent walls. Similarly, if a longer breathing period were present for the emphysemic conditions, particles might have enough time to diffuse to the alveolar walls. These conclusions agree with previous work completed by Jessica Oakes (2008) and Sturm and Hofmann (2004). Both studies report decreased deposition occurring in emphysemic models with higher particle diffusion in the healthy models.

6.5.4 – Normal Healthy Breathing vs. Heavy Healthy Breathing

Figure 6.32 and Figure 6.33 illustrate the comparisons between the normal healthy and heavy healthy breathing *in vivo* predictions occurring at the 10th location (closest to the model inlet) and 2nd location (furthest from the inlet), respectively. It is seen that the heavy normal breathing models maximum velocity is 116% larger than the normal healthy magnitudes for both locations. This is due to 116% difference between the *in vivo* model expansions (16% for normal healthy and 60% for heavy healthy breathing), during the same time period.

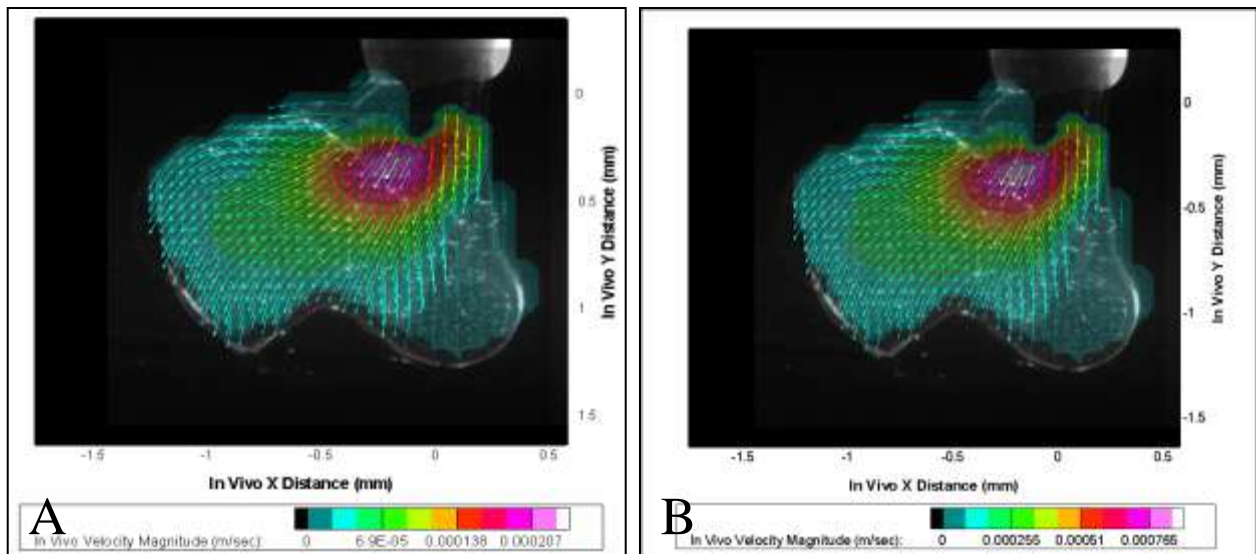


Figure 6.32 – 10th location for the (A) normal healthy human model (Re = 0.009) and the (B) heavy healthy model (Re = 0.035).

Because the heavy healthy model has an *in vivo* percent expansion of 60%, a total of 0.8 mm³ is inhaled each breath as compared to 0.2 mm³ for the normal healthy breathing condition (percent expansion of 16%). This suggests that particles travel deeper into the heavy healthy breathing model by convection alone for a single breath. Because each model has the same initial *in vivo*

volume and breathing period, diffusion would also dominate in the heavy healthy model because the deeper particles would have less of a distance to travel to deposit on the alveolar walls. Similar to the normal healthy versus the normal emphysema case, residence time is irrelevant in this situation because the *in vivo* breathing frequencies are identical.

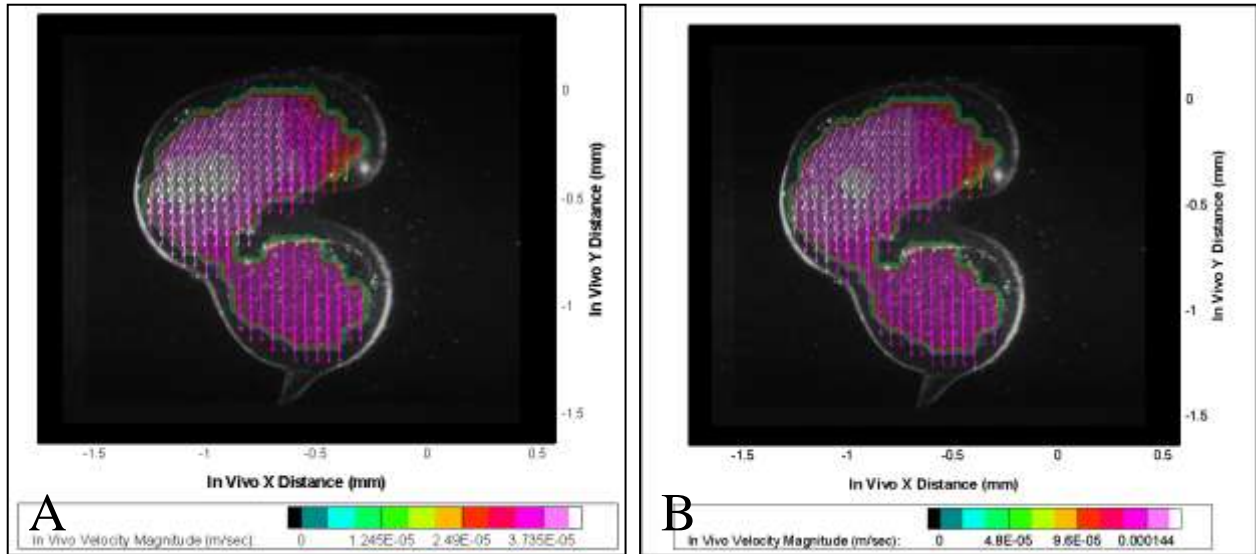


Figure 6.33 - 2nd location for the (A) normal healthy human model ($Re = 0.009$) and the (B) heavy healthy model ($Re = 0.035$).

6.5.5 – Heavy Healthy Breathing vs. Normal Emphysemic Breathing

Although the breathing conditions for a healthy heavy breather are very different from an emphysematic breathing normally (shown in Table 6.6), the breathing conditions result in similar Re ($Re = 0.035$). Even though the calculated *in vivo* Re are equal for heavy healthy and normal emphysemic breathing, the time averaged *in vivo* flow rates at the model inlets for the normal emphysemic breathing condition is 2x larger than the *in vivo* heavy healthy breathing ($1.03E-3$ mL/sec for normal emphy and $4.91E-4$ mL/sec for heavy healthy). This is, again, due to the larger initial volume of the emphysemic model (11x larger than the healthy model), and the substantially larger percent expansion of the heavy healthy model (5.5x larger than the emphysemic expansion). The difference between the two flow rates is found by the ratio of the volume differences to the expansion differences (11x larger emphysemic volume / 5.5x larger healthy expansion). Similarly, the *in vivo* velocity at the model inlet for the heavy healthy case, however, is 2x larger than the normal emphysemic condition (3.7 mm/sec for heavy healthy and

1.6 mm/sec for normal emphysema). These differences stem from the differences between the *in vivo* duct diameters (emphysemic *in vivo* diameter is 2x the healthy).

The differences that exist between the *in vivo* flow fields were analyzed to compare the effects of the healthy and emphysemic geometries for similar non-dimensional flow fields ($Re = 0.035$). For example, Figure 6.34 represents the predicted *in vivo* flow fields that exist closest to the model inlet for both the heavy healthy (10^{th} location) and normal emphysemic (8^{th} location) models for an *in vivo* Re of 0.035 (refer to Figure 6.1 and Figure 6.20 for the laser plane locations for the healthy and emphysemic models, respectively). The maximum *in vivo* heavy healthy breathing velocity magnitude is $8.86E-4$ m/s, occurring near the inlet of the model, while the maximum normal emphysemic breathing *in vivo* magnitude is $2.69E-4$ m/s; more than 3x less than the maximum heavy healthy magnitude with a difference of 107%.

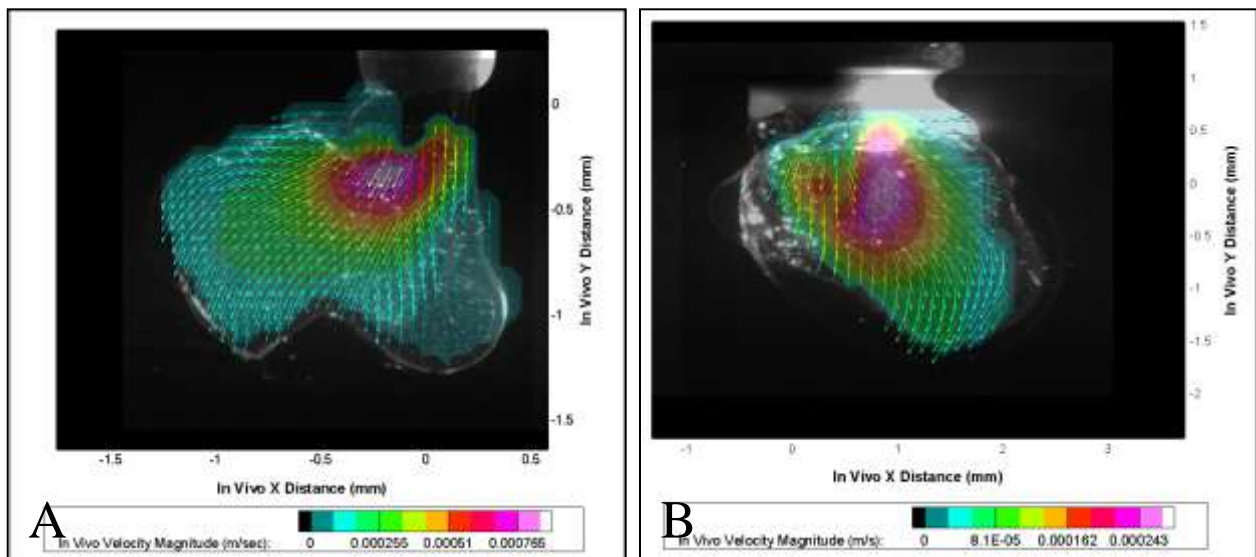


Figure 6.34 - (A) 10th location in the healthy heavy human model and the (B) 8th location of the normal emphysemic model (*in vivo* $Re = 0.035$).

For further comparison, the 2^{nd} locations were compared to illustrate the differences existing at the furthest distances from the inlet of the model, again for an *in vivo* Re of 0.035 (Figure 6.35). The maximum velocity occurring at this location in the normal breathing emphysemic model is $8.57E-5$ m/s, representing a 63% difference from the heavy healthy model ($1.64E-4$ m/s).

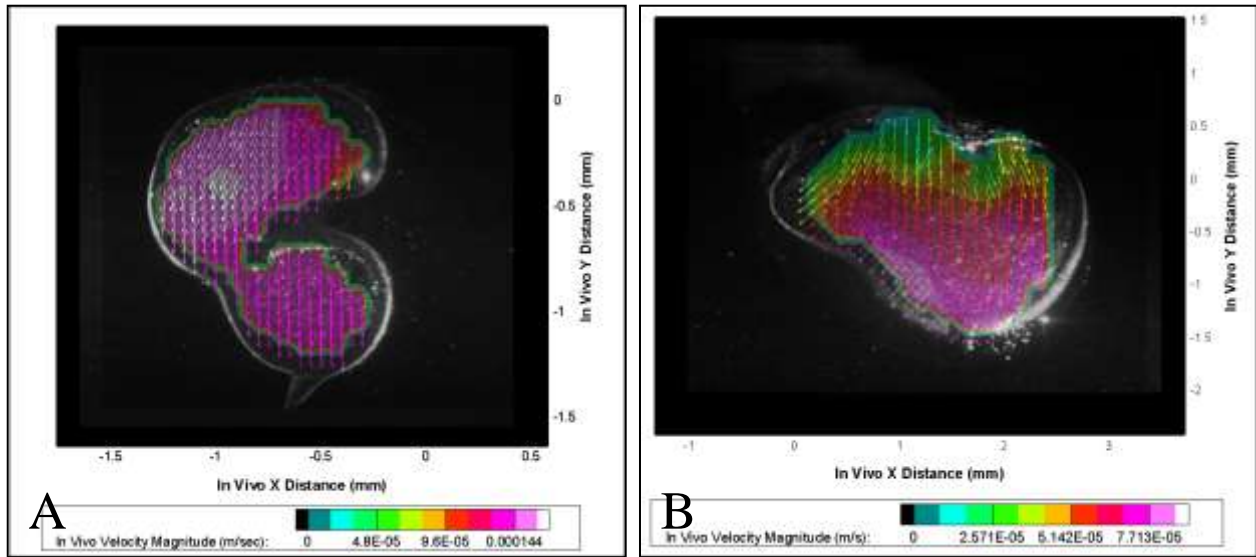


Figure 6.35 – 2nd location in the (A) heavy healthy human model and the (B) normal emphysemic model (in vivo $Re = 0.035$).

Based on the *in vivo* breathing conditions and initial model volumes, the normal breathing emphysemic model inhales two times as much fluid as the heavy breathing healthy model (1.6 mm^3 versus 0.8 mm^3 , respectively). Similar to the conclusions made in section 6.5.3, the difference in volume change indicates that particles would travel deeper into the emphysemic model by means of convection. The larger volume change of the heavy breathing healthy model (as compared to the normal breathing healthy), however, indicates that particles would travel deeper into the heavy healthy breathing as compared to the normal breathing healthy. Therefore, the travel distance required for deposition in the heavy healthy model is significantly less than previously seen in the normal healthy model. This suggests that particles in the heavy healthy model would diffuse at a much faster rate than in the emphysemic model even if the emphysemic volume is 11x larger than the healthy model. Residence time continues to have little effect in this case because the *in vivo* breathing frequencies are similar.

Chapter 7: Conclusions and Discussion

7.1 – Remarks

The present research was successful in the execution of its predefined goals (Chapter 1):

1. Create compliant hollow models
 - Two experimental model prototypes were created from *in vivo* healthy and emphysemic human lung geometries. The healthy model was 19.4x *in vivo* size, while the emphysemic model represented 8.9x *in vivo* dimensions. Compliant models were then obtained for both experimental geometries using the dipping techniques developed in our lab.
2. Develop PIV setup capable of 3D flow field analysis
 - Stereoscopic particle image velocimetry (stereoPIV) techniques were successfully employed to visualize the 3D fluid flows occurring in each of the experimental models. An experimental setup was developed to accommodate the necessary components in the system while a LabVIEW program was created to expand and contract the compliant models based on the desired input parameters. A fluid scaling analysis was performed to ensure that the *in vivo* flow fields were well represented experimentally. Finally, the stereoPIV setup was validated by comparing the results of a full experimental analysis of simple 3D bulb geometry to the results of a CFD analysis.
3. Complete stereoPIV analysis on healthy and emphysematous models
 - Using the validated setup, healthy and emphysemic models were analyzed and compared. Specifically, the differences in model geometries were compared along with the variations that occur in each of the flow fields (i.e. velocity magnitudes and velocity distributions across a given plane). Finally, the characteristics that affect particle transport were discussed and compared between the healthy and emphysemic models.

7.2 – Healthy versus Emphysemic Models

It was shown that major geometric differences exist between the healthy and emphysemic geometries. The major difference separating the two models is the presence of potential recirculation regions in the healthy model. These locations were determined based on defined bulb structures that yield small ratios of alveolar depth to mouth diameter. The emphysemic model, however, contained no such geometry. In fact, the overall appearance of the emphysemic model appeared to contain two distinct sections merged into a single large alveolus. The predicted *in vivo* flow fields yield reversible flow occurring everywhere in each model. Therefore, the geometric differences had no impact on the presence of reversible or recirculating flow.

The velocities occurring closest to the model inlet in the typical emphysemic breathing model were larger than those found in the typical healthy breathing flow fields. Therefore, more ventilation occurred in the typical breathing emphysemic model (as compared to the typical breathing healthy model) because of the higher average flow rates at the model inlet. The healthy model exhibited a very uniform flow field distribution with the magnitudes decreasing from the center of the model out towards the wall. The emphysemic model, however, illustrated a non-uniform spread. It was concluded that particles are more likely to deposit in the normal healthy breathing model rather than in the normal breathing emphysemic model because of the ratio of percent expansion to initial model volume. Even though particles would potentially travel deeper into the emphysemic model, the distance required to deposit would be less for the healthy normal breathing condition. These results agree with the previous studies of Oakes (2010; 2008) and Sturm and Hofmann (2004) who studied the differences occurring between normal healthy breathing and normal emphysemic breathing.

Because of the larger model percent expansion, the velocities occurring throughout the heavy breathing healthy model were significantly larger than those seen in the normal breathing healthy case (for all locations analyzed). In addition, because particles travel further into the heavy breathing model, they have a higher tendency to deposit on the alveolar walls.

The same flow field distributions occurred between the heavy breathing healthy and normal breathing emphysemic comparison as was shown between the normal breathing healthy and normal emphysemic breathing case. Because of the larger inlet flow rates, however, more ventilation was seen in the normal breathing emphysemic case. Finally, it was concluded that particles would be more likely to deposit in the heavy breathing healthy model as opposed to the normal emphysemic model because of the larger percent expansion, and, therefore, expected deeper penetration of the healthy breathing heavy model.

7.2.1 – Discussion of *In Vivo* Predictions

As shown in Chapter 2, the size and location of the inlet ducts for each model were arbitrarily chosen to fit with the contours of the model. The below discussion aims to address how the dimensions and locations of the inlet ducts and the final chosen models affects the *in vivo* predictions as defined in section 6.5.

7.2.1.1 – Residence Time

Residence time is defined as the amount of time a particle has to deposit in the lung during a single breath. It is determined based on *in vivo* conditions from literature; specifically breathing frequency. The predicted residence times in this work are relevant to *in vivo* conditions because the *in vivo* flow parameters were matched between the *in vivo* and experimental models; assuming that the breathing frequency used for the entire lung is the same that occurs in individual alveoli. Because residence time is related to the breathing frequency, the sizes of the final model section and the duct diameter have no effect on particle residence time. The residence time for emphysemic conditions is slightly lower than those seen in typical healthy humans because the *in vivo* breathing period is smaller (3.7 seconds for typical emphysemic conditions and 3.8 seconds for typical healthy conditions). Therefore, particles will have a longer time to deposit in the healthy model as opposed to the emphysemic model. In this work, the difference between typical healthy breathing and heavy healthy breathing is percent expansion. Therefore, the residence times in these models are equal.

7.2.1.2 – Particle Penetration Depth

Penetration depth is the distance a particle (either air or aerosol) is expected to travel into the lung for a given breathing period, as measured by the distance from the position at the start of inhalation. In our model, we predicted measurements from the duct entrance, which would represent a particle that was already in the lung at the alveoli at the start of inhalation.

Penetration depth cannot be determined directly from the presented results since three-dimensional pathlines are required. However, the 3D flow fields can be used in the future to derive this information. For this work, we estimated relative penetration depth to inhalation volume. The functional residual capacity (FRC) and tidal volume (inhaled volume) were taken from literature and the expansion was calculated by the tidal volume / FRC. It should be noted that penetration depth must be related to the location of the final position of a particle relative to the model wall, since the wall is where gas exchange and particle deposition occurs. If we assume that the lung expands uniformly in every lobe and alveoli, the percent expansion of the model is directly related to *in vivo* expansions. Although absolute volume inhaled is directly related to the size of the initial model selected, the desired percent expansion is not affected by model or duct size. Therefore, relative penetration depth is not affected by the size of the model or the duct diameter; it is related to the applied model expansion. In this work, we made observations about the penetration depth relative to the inhaled volume (the percent of inhaled volume relative to the total volume of the model). This comparison was completed for each of the three cases (typical healthy versus typical emphysemic breathing, typical healthy versus heavy healthy breathing, and heavy healthy versus typical emphysemic breathing) and is presented in the above section (section 7.2). In conclusion, even though the penetration depth is higher in the emphysemic model as compared to the typical healthy model, the relative penetration depth is smaller because the volume required to penetrate is much larger in the emphysemic as compared to the healthy model; for the models chosen in this work.

If a different model were created with a larger duct diameter, for example, the model volume would be less due to a smaller required scaling factor to obtain *in vivo* dimensions. If the same input parameters were applied to this new model, specifically percent expansion, the relative penetration depths would be identical. Therefore, the penetration depth predictions presented above are very relevant to *in vivo*.

7.2.1.3 – Particle Deposition

Deposition by diffusion and sedimentation depends on both penetration depth and residence time. Penetration depth defines how far a particle is carried in from the convective motion of the wall expansion and how much distance is remaining to get to the wall after inhalation.

Residence time is how long particles are in the lung or the time allowed for particles to deposit. Because the breathing periods are similar for healthy and emphysemic conditions, the residence times are analogous. As described above, the penetration depths in typical emphysemic models are larger than those seen in typical healthy models because of the model percent expansion. The volume to penetrate in the typical emphysemic model, however, is much larger than the typical healthy model, which yields lower deposition by diffusion in the typical emphysemic model as compared to the typical healthy model. Because the heavy healthy model has a larger percent expansion, however, deposition is even more prevalent in the heavy healthy model as compared to the typical emphysemic model. Similarly, deposition is greater in the heavy healthy model as compared to the typical healthy model because of the large difference in percent expansion. Note that we are assuming a lumped capacitance approach to these predictions. This assumes that diffusion from the streamline occurs only after a particle is completely inhaled. In reality, however, drifting from the streamline occurs during inhalation.

7.2.1.4 – Flow Rate

The input flow rates applied to each model were determined based on the initial model volume, breathing period, and desired percent expansion. If different model dimensions were used, however, the flow rates would be affected by the initial model volume of the model. From Chapter 2, the model size is determined based on the scaling factor applied in order to achieve the appropriate duct diameter. Therefore, if the duct diameter's arbitrary dimension were increased, for example, the scaling factor would be decreased, therefore decreasing the initial volume of the model (assuming the same model location was selected from the original cast). Assuming the same input breathing period and percent expansion, a lower input flow rate would result in a model with a larger *in vivo* duct diameter as opposed to the models used in this work.

7.2.1.5 – Velocity Fields

The experimental velocity fields determined from stereoPIV were scaled back to represent *in vivo* flow fields using *in vivo* flow conditions (see Chapter 3). These *in vivo* fields allowed us to demonstrate the importance of diffusive relative to convective motion, which is needed to model air and particle flow. Similar to the flow rates, the velocity field magnitudes would change if different models were created other than the ones used in this work. Again, for example, if a larger arbitrary duct diameter was chosen, the resulting model volume would be smaller than that seen in this work. This would yield smaller experimental velocity magnitudes. The resulting *in vivo* flow fields would also have smaller magnitudes because the ratio of the experimental diameter to the *in vivo* diameter would be less than that used in this work.

7.3 – Limitations of Work

One limitation in the current research is the settings of the cameras used to acquire raw PIV images. The most accurate setting would be 90° between the cameras, but because of restricted optical access, smaller angles were required, reducing the accuracy of the results, particularly in the z-direction as shown in the bulb model. Therefore, to optimize the vector field results, Scheimpflug mounts are traditionally used. In this work, however, Scheimpflug mounts were not used. If future work is performed, the use of these mounts is highly recommended to optimize the accuracy of the experiments (especially the z-component of velocity).

Another limitation of the experimental setup involved the location of the syringe pump used to expand and contract the experimental models. Because the pump was located to one side of the model, the rig had a tendency to non-uniformly expand the compliant models during experimentation, and was illustrated in the boiling flask validation. This non-uniform expansion resulted in the velocities on the left side of the model being less than the predicted values with the right side velocities being higher than the predictions.

A final limitation existing in the experimental setup dealt with the tracer particles. Over long periods of time, the particles had a tendency to disperse unevenly throughout the model. Unfortunately, the only way to re-mix the particles required the entire model to be removed from the setup. Because of this movement in particles, experiments for a given model needed to be

completed in a single setting as to not detect the rising of the particles. This limitation, however, had no affect on the results of this study.

7.4 – Future Work

The conclusions generated from the *in vivo* predictions related to particle transport occurring in healthy and emphysemic geometries. Quantitative results for particle penetration depths were unable to be calculated in this work because it was unclear how potential particles would travel in a non-symmetric model. Pathlines were also unable to be calculated because time elapsed sequences were not analyzed. It is suggested for future work, however, to extract 3D pathlines to determine the penetration depths and general paths of particles throughout healthy and emphysematous models. 3D pathlines would also allow for more accurate predictions of convective transport.

As stated above, the accuracy of the experimental results was reduced because the Scheimpflug mounts were not used in the experimental setup. If future stereoPIV work is completed, the use of these mounts is highly recommended to maximize the accuracy of the desired outputs. These mounts would also increase the quality of the raw images because the entire field of view would be in focus; optimizing the correlation peaks in the image processing.

It was demonstrated that a measured conversion factor is desired to compare to the factor calculated by Insight. Although this was done for the boiling flask model, it was not completed for the emphysemic or healthy models. Therefore, the results of the healthy and emphysemic models contain a small amount of error from the pixel to length conversions (as calculated in Insight 3G). It is suggested to measure the conversion factors for the laser plane locations used in the reported results and scale the experimental and predicted *in vivo* velocity fields by the ratio of the measured to the calculated conversion factors. Finally, compare the differences between the results from the two geometries when using the calculated factor versus the measured factor.

References

- Angus, G. E., and W. M. Thurlbec. 1972. Number of alveoli in human lung. *Journal of Applied Physiology* 32 (4):483-&.
- Berg, E. J., J. L. Weisman, M. J. Oldham, and R. J. Robinson. 2010. Flow field analysis in a compliant acinus replica model using particle image velocimetry (PIV). *J Biomech* 43 (6):1039-1047.
- Bloch, K. E., Y. M. Li, J. N. Zhang, R. Bingisser, V. Kaplan, W. Weder, and E. W. Russi. 1997. Effect of surgical lung volume reduction on breathing patterns in severe pulmonary emphysema. *American Journal of Respiratory and Critical Care Medicine* 156 (2):553-560.
- Colebatch, H. J., K. E. Finucane, and M. M. Smith. 1973. Pulmonary conductance and elastic recoil relationships in asthma and emphysema. *Journal of Applied Physiology* 34 (2):143-153.
- Darquenne, C. 2001. A realistic two-dimensional model of aerosol transport and deposition in the alveolar zone of the human lung. *Journal of Aerosol Science* 32 (10):1161-1174.
- Dynamics, D. 2010. Stereoscopic PIV. PowerPoint Presentation, 1-15.
- Haefelibleuer, B., and E. R. Weibel. 1988. Morphometry of the human pulmonary acinus. *Anatomical Record* 220 (4):401-414.
- Harding, E. M., and R. J. Robinson. 2010. Flow in a terminal alveolar sac model with expanding walls using computational fluid dynamics. *Inhalation Toxicology* 22 (8):669-678.
- Karl, A., F. S. Henry, and A. Tsuda. 2004. Low Reynolds number viscous flow in an alveolated duct. *Journal of Biomechanical Engineering-Transactions of the Asme* 126 (4):420-429.
- Klinge, T. G., and N. C. Staub. 1970. Alveolar shape changes with volume in isolated, air-filled lobes of cat lung. *Journal of Applied Physiology* 28 (4):411-&.
- Kohlhauf, M., P. Brand, T. Meyer, G. Scheuch, N. Weber, K. Haussinger, H. Schulz, and J. Heyder. 1997. Detection of impaired intrapulmonary convective mixing by aerosol bolus dispersion in patients with emphysema. *Eur J Med Res* 2 (3):121-128.

- Kohlhauf, M., P. Brand, G. Scheuch, T. Meyer, H. Schulz, K. Haussinger, and J. Heyder. 2000. Aerosol morphometry and aerosol bolus dispersion in patients with CT-determined combined pulmonary emphysema and lung fibrosis. *Journal of Aerosol Medicine-Deposition Clearance and Effects in the Lung* 13 (2):117-124.
- Kumar, H., M. H. Tawhai, E. A. Hoffman, and C.-L. Lin. 2009a. The effects of geometry on airflow in the acinar region of the human lung. *Journal of Biomechanics*.
- Kumar, H., M. H. Tawhai, E. A. Hoffman, and C. L. Lin. 2009b. The effects of geometry on airflow in the acinar region of the human lung. *Journal of Biomechanics* 42 (11):1635-1642.
- LaVision. *Particle Image Velocimetry* 2009 [cited June 8, 2010].
- Loudon, C., and A. Tordesillas. 1998. The use of the dimensionless Womersley number to characterize the unsteady nature of internal flow. *Journal of Theoretical Biology* 191 (1):63-78.
- Macklem, P. T., and N. J. Wilson. 1965. Measurement of intrabronchial pressure in man. *Journal of Applied Physiology* 20 (4):653-&.
- Mercer, R. R., J. M. Laco, and J. D. Crapo. 1987. 3-Dimensional reconstruction of alveoli in the rat for pressure-volume relationships. *Journal of Applied Physiology* 62 (4):1480-1487.
- Metro Health System, T. *Chronic Obstructive Lung Disease (COPD)*. Medseek, Inc 2008 [cited Accessed June 16, 2010].
- Netter, F. H. 1979. The Ciba Collection of Medical Illustrations, 16, 24.
- Oakes, J. 2008. Thesis: Flow field analysis in an expanding healthy and emphysematous alveolar model using particle image velocimetry, Mechanical Engineering, Rochester Institute of Technology, Rochester, NY.
- Oakes, J. M., S. Day, S. J. Weinstein, and R. J. Robinson. 2010. Flow field analysis in expanding healthy and emphysematous alveolar models using particle image velocimetry. *J Biomech Eng* 132 (2):021008-021001 - 021008-021009.
- Phalen, R. F., H. C. Yeh, O. G. Raabe, and Velasque.Dj. 1973. Casting lungs in-situ. *Anatomical Record* 177 (2):255-263.

- Robinson, R. J., R. L. Doolittle, and J. N. Diflorio. 2007. Use of asthmatic pulmonary function test data to predict lung deposition. *Journal of Aerosol Medicine-Deposition Clearance and Effects in the Lung* 20 (2):141-162.
- Sciences, N. I. o. E. H. *Environmental asthma and COPD group* 2009 [cited 9/11/2009].
- Soria, J. 2000. Particle image velocimetry: A practical guide. *Journal of Fluid Mechanics* 377:374-381.
- Sturm, R., and W. Hofmann. 2004. Stochastic simulation of alveolar particle deposition in lungs affected by different types of emphysema. *Journal of Aerosol Medicine-Deposition Clearance and Effects in the Lung* 17 (4):357-372.
- Sznitman, J., F. Heimsch, T. Heimsch, D. Rusch, and T. Rosgen. 2007a. Three-dimensional convective alveolar flow induced by rhythmic breathing motion of the pulmonary acinus. *Journal of Biomechanical Engineering-Transactions of the Asme* 129 (5):658-665.
- Sznitman, J., T. Heimsch, J. H. Wildhaber, A. Tsuda, and T. Rosgen. 2009. Respiratory flow phenomena and gravitational deposition in a three-dimensional space-filling model of the pulmonary acinar tree. *J Biomech Eng* 131 (3):031010.
- Tippe, A., and A. Tsuda. 2000. Recirculating flow in an expanding alveolar model: Experimental evidence of flow-induced mixing of aerosols in the pulmonary acinus. *Journal of Aerosol Science* 31 (8):979-986.
- TSI, I. 2009. Insight 3G - Data acquisition, analysis, and display software platform: User's Guide, 343.
- Tsuda, A., F. S. Henry, and J. P. Butler. 1995. Chaotic mixing of alveolated duct flow in rhythmically expanding pulmonary acinus. *Journal of Applied Physiology* 79 (3):1055-1063.
- van Ertbruggen, C., P. Corieri, R. Theunissen, M. L. Riethmuller, and C. Darquenne. 2008. Validation of CFD predictions of flow in a 3D alveolated bend with experimental data. *Journal of Biomechanics* 41 (2):399-405.
- Weibel, E. R. 1965. Lung structure. *Medicina Thoracalis* 22 (5):548.
- White, F. M. 2006. *Viscous Fluid Flow*. Third ed: McGraw-Hill.

Womersley, J. R. 1955. Method for the calculation of velocity, rate of flow and viscous drag in arteries when the pressure gradient is known. *Journal of Physiology-London* 127 (3):553-563.